Title
Surfzone Tracer Dispersion: Methods, Observations, and Modeling

Author
Clark, David B.

Publication Date
2010

Peer reviewed

UNIVERSITY OF CALIFORNIA, SAN DIEGO

Surfzone Tracer Dispersion: Methods, Observations, and Modeling

A dissertation submitted in partial satisfaction of the
requirements for the degree
Doctor of Philosophy

in

Oceanography

by

David Brutsche Clark

Committee in charge:

Falk Feddersen, Chair
Robert T. Guza, Co-Chair
Ken Melville
Sutanu Sarkar
Clint Winant

2010

ProQuest LLC
789 East Eisenhower Parkway
P.O. Box 1346
Ann Arbor, MI 48106-1346

The dissertation of David Brutsche Clark is approved, and it is acceptable in quality and form for publication on microfilm and electronically:

_____

_____

_____

_____
Co-Chair

_____
Chair

University of California, San Diego

2010

TABLE OF CONTENTS

LIST OF FIGURES

LIST OF TABLES

ACKNOWLEDGEMENTS

Thanks to my committee for their scientific guidance, and additional thanks to Matt Spydell, Melissa Omand and Aurélien Ponte for our many discussions of surfzone and coastal processes. Thanks to Brian Woodward, Bill Boyd, Kent Smith, Dennis Darnell, and Ian Nagy who designed, built, and operated the jet ski mounted instrument package, and installed instruments in the field. Additional field support was provided by M. Yates, M. McKenna, M. Rippy, S. Henderson, D. Michrokowski, K. Milikan, S. Scott, and the CDIP crew. ONR provided support to design and build the jet ski mounted instrument package. Further support was provided by the California Coastal Conservancy, NOAA, California Sea Grant, and NSF. DBC was supported with Doherty, NDSEG, and NSF fellowships.

Chapter 1, in full, is a reprint of the material as it appears in Air Water and Soil Pollution, 2009, Clark, David B.; Feddersen, Falk; Omand, Melissa; Guza, R.T., Springer, 2009. The dissertation author was the primary investigator and author of this paper.

Chapter 2, in full, is a reprint of the material as it appears in Journal of Geophysical Research - Oceans, 2010, Clark, David B.; Feddersen, Falk; Guza, R.T., Elsevier, 2010. The dissertation author was the primary investigator and author of this paper.

Chapter 3, in part is currently being prepared for submission for publication of the material. Clark, David B.; Feddersen, Falk; Guza, R.T. The dissertation author was the primary investigator and author of this material.

Chapter 4, in part is currently being prepared for submission for publication of the material. Clark, David B.; Feddersen, Falk; Guza, R.T. The dissertation author was the primary investigator and author of this material.

VITA AND PUBLICATIONS

2003	B. S. in Physics, University of California Santa Barbara
2010	Ph. D. in Oceanography, University of California, San Diego

PUBLICATIONS

Clark, D. B., F. Feddersen, M. M. Omand, and R. T. Guza, "Measuring Fluorescent Dye in the Bubbly and Sediment Laden Surfzone", *Air Water and Soil Pollution*, 204(1-4), p. 103-115, doi: 10.1007/s11270-009-0030-z, 2009.

Clark, D. B., F. Feddersen, and R. T. Guza, "Cross-shore Surfzone Tracer Dispersion in an Alongshore Current", *Journal of Geophysical Research - Oceans*, 115(C10035), doi: 10.1029/2009JC005683, 2010

ABSTRACT OF THE DISSERTATION

Surfzone Tracer Dispersion: Methods, Observations, and Modeling

by

David Brutsche Clark

Doctor of Philosophy in Oceanography

University of California, San Diego, 2010

Falk Feddersen, Chair
Robert T. Guza, Co-Chair

Decisions about recreational beach closures would be enhanced with better estimates of surfzone contaminant transport and dilution. New *in situ* methods, developed here, for measuring fluorescent Rhodamine WT dye tracer in the surfzone increase the temporal and spatial resolution over previous techniques. Bubbles and sand suspended by breaking waves in the surfzone interfere with *in situ* optical fluorometer dye measurements, but turbidity correction reduces root-mean-square dye concentration errors to $< 5\%$ of dye concentration magnitude.

Alongshore tracer plumes, formed by continuously releasing dye in a wave driven alongshore current are used to examine cross-shore surfzone tracer dispersion at Huntington Beach, California. Ensemble averaged cross-shore tracer concentration

profiles are generally shoreline attached (maximum at or near the shoreline), with increasing cross-shore widths and decreasing peak concentrations with downstream distance. For each release, cross-shore surfzone absolute diffusivities κ_{xx}, estimated using a simple Fickian diffusion solution with a no-flux boundary at the shoreline, range from $\kappa_{xx} = 0.5 - 2.5\ \mathrm{m^2\,s^{-1}}$. The κ_{xx} scale best with a mixing-length scaling (correlation $r^2 = 0.59$ and the expected scaling versus κ_{xx} best-fit slope < 1), indicating that horizontal rotational motions are important for cross-shore tracer dispersion in the surfzone.

The five tracer plumes used for κ_{xx} estimates are simulated with a time-dependent wave-resolving Boussinesq surfzone model (`funwaveC`) initialized with the observed bathymetry and incident wave spectra. The modeled and observed cross-shore structure of significant wave heights and mean alongshore currents have good qualitative agreement. Modeled and observed low frequency (< 0.03 Hz) horizontal rotational velocities, possibly important for cross-shore dispersion, have similar cross-shore structure, although magnitudes are slightly over predicted.

Modeled tracer is spread by model currents and eddies, a breaking wave eddy diffusivity, and a small ($0.01\ \mathrm{m^2\,s^{-1}}$) background diffusivity. Mean model tracer concentration skill (compared to a zero prediction) is highly variable (from negative to 0.73), however cross-shore integrated moments (normalized by the cross-shore tracer integral) have consistently high skills (~ 0.9). Modeled κ_{xx} estimates are similar to the observations, but the skill (0.4) is only moderate. The model breaking wave eddy diffusivity does not effect dispersion significantly.

Chapter 1

Instrument Development

1.1 Abstract

Decisions about recreational beach closures would be enhanced if better estimates of surfzone contaminant transport and dilution were available. *In situ* methods for measuring fluorescent Rhodamine WT dye tracer in the surfzone are presented, increasing the temporal and spatial resolution over previous surfzone techniques. Bubbles and sand suspended by breaking waves in the surfzone interfere with *in situ* optical fluorometer dye measurements, increasing the lower bound for dye detection ($\approx$ 1 ppb) and reducing (quenching) measured dye concentrations. Simultaneous turbidity measurements are used to estimate the level of bubble and sand interference, and correct dye estimates. After correction, root-mean-square dye concentration errors are estimated to be $< 5\%$ of dye concentration magnitude, thus demonstrating the viability of *in situ* surfzone fluorescent dye measurements. The surfzone techniques developed here may be applicable to other environments with high bubble and sand concentrations (e.g., cascading rivers and streams).

1.2 Introduction

Surfzone dispersion is important to many biological and physical processes including the dilution of contaminated runoff [e.g., *Boehm*, 2003; *Grant et al.*, 2005],

phytoplankton transport [e.g., *Campbell and Bate*, 1988], and larval recruitment [e.g., *Denny and Shibata*, 1989]. However, few surfzone tracer dispersion studies have been conducted, and measurement techniques are less advanced than those used further offshore. As a result, surfzone tracer dispersion is poorly understood. Increased knowledge of transport and dilution in the surfzone would enable beach managers to better minimize public exposure to shoreline pollution.

Fluorescent dye (e.g., Rhodamine WT, or fluorescein), optically measured with a fluorometer, is commonly used to study tracer (i.e., pollutant) dispersion in both marine [e.g., *Okubo*, 1971] and freshwater [e.g., *Csanady*, 1963] environments. Dye measurements are used to estimate eddy diffusivities and scale dependence [e.g., *Okubo*, 1971; *Murthy*, 1976; *Fong and Stacey*, 2003], tracer transport [e.g., *Houghton*, 1997; *Tilburg et al.*, 2007], and other quantities. The observations of diffusion and mixing can be used to calibrate numerical models.

Ideally, accepted *in situ* techniques using flow-through [e.g., *Pritchard and Carpenter*, 1960] or open-face [e.g., *Ledwell et al.*, 2004] fluorometers could be adapted for surfzone use. However, surfzone waves and strong currents can damage instrumentation, hamper deployment, and render many oceanographic instruments and platforms (i.e., boats) unusable. Breaking waves intermittently suspend optically interfering bubbles [e.g., *Deane*, 1997] and sediment [e.g., *Brenninkmeyer*, 1976; *Yu et al.*, 1993], creating highly variable turbidity.

Measured dye fluorescence is altered by many factors, including background fluorescence [*Pritchard*, 1979], temperature, and suspended sediment [*Smart and Laidlaw*, 1977]. Suspended sediment increases apparent background fluorescence without dye in the water, and reduces (quenches) concentration estimates when dye is present. However, the effect of suspended sediment on dye estimates varies with sediment type, color, and concentration [*Smart and Laidlaw*, 1977] and the effect of suspended sand in the surfzone is unknown. The effect of surfzone bubbles on *in situ* dye measurements are also unknown. Dye mass can also be lost to photochemical decay [e.g., *Suijlen and Buyse*, 1994], adsorption [e.g., *Talbot and Boon*, 1975], and other factors [e.g., *Smart and Laidlaw*, 1977], but these processes are not expected to be significant over the few hour duration of most surfzone dispersion studies.

Previous surfzone dye measurements have been limited to bottle samples taken either at the shoreline or near the visually estimated center of a spreading dye patch [*Harris et al.*, 1963; *Inman et al.*, 1971; *Clarke et al.*, 2007]. While simple and inexpensive, the number and distribution of samples has been severely limited, with maximum rates up to 2 bottle samples per minute [*Clarke et al.*, 2007], and a maximum of 4 simultaneous locations over several hours [*Harris et al.*, 1963]. These studies provided important initial estimates of surfzone dispersion, but could not resolve cross-shore dye structure, and used few (or single) dye patch or plume realizations. *In situ* fluorometers allow for higher frequency dye measurements, but have not been implemented in the surfzone, possibly because of concerns that suspended bubbles and sand would degrade instrument performance.

Instruments suitable for *in situ* surfzone measurement of fluorescent Rhodamine WT dye are discussed in Section 1.3, along with possible mechanisms causing high errors in some instruments. The specific instrumentation used here (Section 1.4), and testing procedures (Section 1.5) are described. The effects of surfzone bubbles and sand on *in situ* Rhodamine WT measurements are characterized, and results are given in Section 1.6. Errors in *in situ* surfzone fluorescence are estimated, recommendations are made for error reduction, and example field applications are given in Section 1.7. Details of mixing and delay time within the mobile flow-through fluorometer system, and estimates of effective spatial resolution are given in Appendix A.

1.3 Considerations for *in situ* surfzone Rhodamine WT measurement

Many commercial fluorometers are available. Two widely-used open-face type fluorometers (WET Labs ECO Triplet, and Turner SCUFA) that measure Rhodamine WT dye fluorescence D and turbidity τ were tested side-by-side in a natural surfzone without dye in the water to determine the instruments response to suspended bubbles and sand from breaking waves. Light emitted near the dye excitation peak is fluoresced at a slightly longer wavelength [e.g., *Guibault*, 1990]. The intensity of the fluoresced light is detected at an angle to the excitation beam (scattering angle), and used to determine dye

concentration (Fig. 1.1). The WET Labs ECO Triplet measures D (0.1 - 400 ppb range) with 530 nm (30 nm FWHM, full width half max) wavelength excitation, and 570 nm fluorescence detection (35 nm FWHM), and measures τ (0.03 - 100 ntu, nephelometric turbidity units, range) at 660 nm wavelength. ECO Triplet D and τ both use $117°$ scattering angles. The Turner SCUFA measures D (0.04 - 400 ppb range) with 530 nm (40 nm FWHM) wavelength excitation, and 600 nm (40 nm FWHM) fluorescence detection, and measures τ (0.1 - 400 ntu^* range) at 530 nm. SCUFA D and τ both use $90°$ scattering angles. ECO Triplet and SCUFA τ, with units ntu and ntu^* respectively, are similar but not equivalent due to instrumental differences (Section 1.4.2).

The instruments were mounted 1 m apart, so they were close enough to measure similar turbidities, but far enough apart to eliminate interference. Both the ECO Triplet (Fig. 1.2a) and the SCUFA (Fig. 1.2b) recorded spurious dye measurements (non-zero dye measurements when no dye is present) in response to τ from surfzone bubbles and sand. The ECO Triplet recorded very little spurious dye ($< 0.8\,\mathrm{ppb}$), while the SCUFA recored large spurious dye measurements (up to $17\,\mathrm{ppb}$) that were highly correlated with turbidity τ.

The SCUFA and ECO Triplet measure Rhodamine WT fluorescence with different optical elements and angles. Ideally, narrow banded non-overlapping optical filters on the source and detection elements prevent excitation light from being detected as dye. However, non-ideal optical filters allow excitation light, backscattered off bubbles and sand (Fig. 1.1), to pass through the detection filter, and to be measured as elevated dye concentrations. The SCUFA optical filters have a slightly wider pass-band than the ECO Triplet, possibly increasing SCUFA spurious dye measurements. However, the SCUFA filter centers are also 10 nm further apart than the ECO Triplet, slightly reducing this effect. The intensity of light scattered by surfzone bubbles and sand increases with a reduction in scattering angle [*Zege et al.*, 2006]. Therefore the smaller SCUFA scattering angle increases the excitation light incident on the detection filter, enhancing spurious dye measurements.

Although the SCUFA accurately measures Rhodamine WT in many environments, the combined effects of filters and scattering angle make the SCUFA dye estimate more sensitive to surfzone bubbles and sand (spurious dye values sometimes

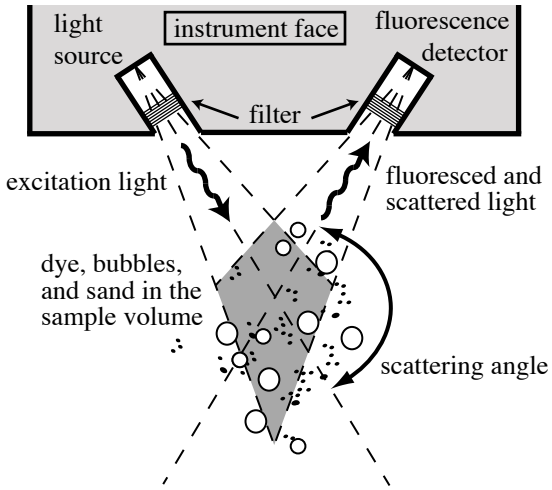

Figure 1.1: Schematic of fluorometer optics (ECO Triplet example). Light emitted near the excitation peak of Rhodamine WT is fluoresced by the dye at a longer wavelength and measured by the detector. When dye concentrations are low, bubbles and sand in the sample volume (center shaded region) scatter excitation light from the instrument towards the dye fluorescence detector. Overlap between the instrument excitation spectrum and the fluorescence detection spectrum allows backscattered excitation light to be falsely interpreted as an elevated dye concentration in the sample volume. When dye concentrations are not low, bubbles and sand reduce the amount of fluoresced light reaching the detector and measured dye concentrations are reduced. Bubbles and sand also backscatter light from the turbidity light source into the turbidity detector (not shown), increasing measured τ

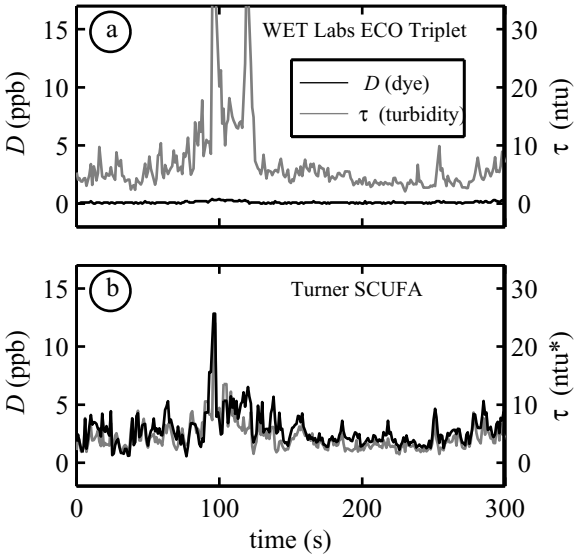

Figure 1.2: Field measurements of spurious D (black) and τ (gray) versus time with no dye in the water for (a) WET Labs ECO Triplet and (b) Turner SCUFA. The instruments were deployed mid-surfzone, 0.5 m above the seabed in 1 m depth, and separated 1 m in the alongshore at Scripps Beach, CA with small spilling waves. Seaward of the surfzone, significant wave height was 0.5 m and peak period was 15 s. Note turbidity units ($\mathrm{ntu}, \mathrm{ntu}^*$) are similar but not equivalent due to instrumental differences (Section 1.4.2)

reached 80 ppb, not shown) than the ECO Triplet. Further testing to determine the effect of surfzone bubbles and sand on ECO Triplet dye measurements is described below (Section 1.6).

1.4 Surfzone dye fluorescence instrumentation

In situ open-face type (frame mounted, fixed location) and flow-through type (mobile, jet ski mounted, Fig. 1.3) fluorometer systems were used to measure Rhodamine WT dye concentration (D) in the surfzone. Fixed location fluorometers provide much higher temporal resolution and longer sampling periods than previous hand-filled bottle methods, but extensive spatial coverage is precluded by cost and logistics. Increased spatial coverage is provided by a jet ski mounted fluorometer system. The jet ski allows fast repeated cross- and alongshore transects though the surfzone where traditional boats and submersibles cannot go. Simultaneous turbidity (τ) measurements are used to estimate relative bubble and sand interference in the instrument sample volume, and to correct estimates of D. These instruments can also be used to measure surfzone chlorophyll-a, but the methodology differs from dye [*Omand et al.*, 2009].

WET Labs ECO Triplet open-face type fluorometers (hereafter ET) were used to measure dye concentration D and backscatter turbidity τ (see Section 1.3 for specifications), and were frame-mounted at fixed locations in the field. The ETs averaged 8 Hz data to yield sampling rates of 0.89 Hz in the laboratory and 0.23 Hz in the field.

The jet ski mounted flow-through fluorometer / turbidity sensor system (hereafter WS) consisted of a WET Labs Wetstar fluorometer (470 nm excitation wavelength, 570 nm fluorescence detection, 0.11 - 400 ppb range) and a Turner SCUFA turbidity sensor (see Section 1.3 for specifications) with flow-through cap. Although the SCUFA is capable of measuring both fluorescence and turbidity (Section 1.3), the surfzone fluorescence signal was noisy (Fig. 1.2). Here, the SCUFA (robust enough for surfzone conditions) is used only for its flow-through turbidity measurement. Water, drawn through the jet ski mounted intake boom from 20 cm below the surface with an electric pump, passes through a debubbler, the SCUFA turbidity sensor, and finally the Wetstar fluorometer (Fig. 1.3). The debubbler (a small 200 ml chamber) allows air to escape from the

top and water to flow out of the bottom, reducing the number of large bubbles entering the optical instruments. The flow-through system hoses and debubbler (Fig. 1.3) smooth sharp gradients in dye occurring over times less than 2.4 s, and delay dye measurements relative to GPS positions (Appendix A). Dye fluorescence D, turbidity τ, water temperature (measured at the end of the intake boom), and GPS position are sampled at 5 Hz. Data are both logged onboard and transmitted to a shore station, allowing real-time analysis and adaptive sampling. A handlebar mounted screen displays real time data and a local map of position, allowing repeated sampling of pre-determined transects.

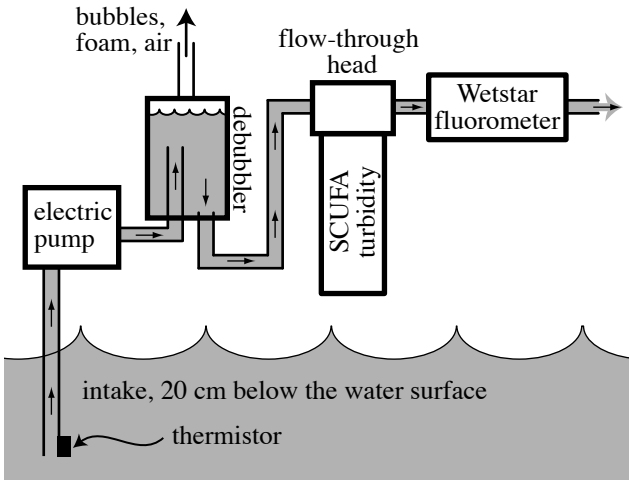

Figure 1.3: Schematic of jet ski mounted WS flow-through system (diagram is not to scale)

1.4.1 Fluorometer calibrations

Fluorometers were calibrated at four temperatures ($7 - 24\ ^{\circ}\mathrm{C}$ range) using nine known concentrations of Rhodamine WT (0 - 400 ppb range) in filtered (to remove particles) seawater. Salinity, alkalinity, and pH all weakly effect dye fluorescence [*Feuerstein and Selleck*, 1963; *Smart and Laidlaw*, 1977; *Stanbro and Pyrch*, 1979], thus calibrations were always conducted in seawater. Dye calibrations were found to be within 15% of the factory calibrations. ET calibrations were slightly nonlinear above 100 ppb, and Wetstar calibrations were linear up to 400 ppb. Calibrations before and after the field deployment were similar. Temperature dependence followed *Smart and Laidlaw* [1977],

$D_{T_0} = D_T \exp[0.027(T - T_0)]$, where D_{T_0} is the dye fluorescence normalized to a reference temperature T_0 (°C), and D_T is the dye fluorescence at the *in situ* temperature T (°C). Factory turbidity calibrations were used for both the ET and WS.

1.4.2 Turbidity measurements

Turbidity τ measured with the ET (ntu) and the SCUFA (ntu*) are not equivalent, because the backscatter wavelengths and angles are different (Section 1.3). In laboratory experiments using Scripps Beach sand suspended in seawater (Fig. 1.4) SCUFA and ET τ were similar for sand concentrations $< 8\ \mathrm{g\,L^{-1}}$ (< 30 ntu, ntu*). However, above $8\ \mathrm{g\,L^{-1}}$ the SCUFA τ was less responsive to sand than the ET. The SCUFA τ sensor saturates near 75 ntu*, at sand concentrations $> 20\ \mathrm{g\,L^{-1}}$ that are not expected above the bottom boundary layer in the surfzone. Additional tests (Fig. 1.5) show that SCUFA $\tau > 75$ ntu* can be produced by bubbles or a combination of bubbles and sand, but not by sand alone. SCUFA τ, well beyond the recommended 100 ntu* upper limit (Turner Designs SCUFA manual, revision 2.1), are used because they prove useful for error estimation and dye correction in the WS instrument package (Section 1.7). The τ response to bubble void fraction was not measured.

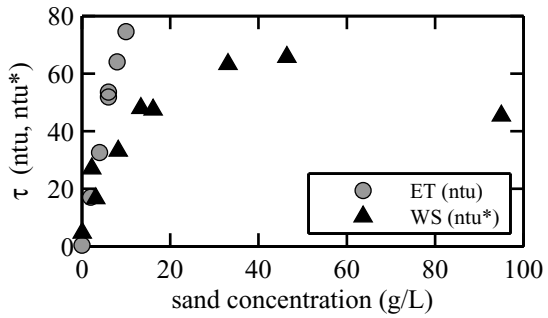

Figure 1.4: Laboratory averaged turbidity τ versus sand concentration for ET (black triangles) and WS (gray circles) using Scripps Beach (La Jolla, CA) sand. For the open-face ET, known amounts of sand were completely suspended by vigorous stirring in a laboratory tank, and turbidity was averaged over 2 minutes. For the flow-through WS, sand laden water was drawn into the system, and the average dried sand concentrations were measured from discharge water

1.5 Instrument testing methods

The effects of surfzone bubble and sand induced turbidity τ on dye measurements D were observed both with and without dye in the water. Experiments without dye were conducted in both the field (surfzone) and the laboratory. However, controlled dye concentrations could not be produced in the field, so tests with known (non-zero) dye concentrations were performed in the lab where τ levels were varied by altering the amount of suspended bubbles and sand. To apply laboratory-based results to the field, it is assumed that natural surfzone τ over a sand bottom is primarily caused by bubbles and sand (i.e.,not from mud, organic matter, etc.).

1.5.1 Field methods

ET and WS instruments were tested over several days in the surfzone at Huntington Beach, California, where significant wave height was about 1 m, peak periods ranged from 14 to 16 s, and hourly surfzone averaged alongshore currents reached 0.5 $\mathrm{m\,s^{-1}}$. Huntington Beach sand is a tan medium grained quartz typical of the Southern California coast. Four ETs were deployed in various cross-shore locations between the shoreline and 4 m mean water depth. The ETs were mounted nominally 0.5 m above the bed with the sensor facing downward at 30 degrees from vertical. Collocated temperature measurements were used for ET dye calibration (Section 1.4.1). The jet ski mounted WS was driven on $\approx 200\ \mathrm{m}$ long cross-shore transects from seaward of the surfzone towards the shore (inbound transect) until the jet ski turned around near the shoreline ($\approx\ 0.5\ \mathrm{m}$ water depth) and returned offshore (outbound transect). WS field data were corrected for delay time (relative to GPS positions) within the flow-through system (Appendix A).

1.5.2 Laboratory methods

Laboratory experiments with and without dye in the water were conducted for both the open-faced ET and the flow-through WS system. Black (to reduce reflected light) containers were filled with 15 liters of filtered seawater, and 5 dye concentrations (0 - 238 ppb). The ET was held in the container at mid-water depth ($\approx$ 15 cm), and for the WS the intake and discharge hoses were mounted near the bottom of the con-

tainer. Bubbles ($\approx$ 0.1 - 5 mm diameter) roughly representative of those injected into the surfzone by breaking waves [*Deane and Stokes*, 1999], were added using an aquarium aerator. Scripps Beach sand, a tan medium-grained quartz, was added by hand. Each system was perturbed with bubbles, then with sand, and finally with bubbles and sand combined. Bubbles and sand were suspended by vigorous stirring, allowed to settle, and then the process was repeated. It was unknown if the bubble and sediment size distribution of a stirred laboratory container closely represented that suspended in a natural surfzone. However, the amounts of bubbles and sand in the laboratory were varied so the turbidity range spanned that found in the field.

1.6 Results

1.6.1 Field and laboratory without dye

Field and laboratory data (D and τ) without dye in the water were collected with the ET (Fig. 1.5a,b) and the WS (Fig. 1.5c,d) instruments. Spurious dye concentrations D (when no dye is present) increase with turbidity τ in both field and laboratory measurements, consistent with *Smart and Laidlaw* [1977]. High τ events are infrequent in the surfzone for both instruments (Fig. 1.5b,d), resulting in low mean spurious D (0.25 ppb for ET, and 0.39 ppb for WS) in the surfzone.

The standard deviation (STD) of spurious dye measurements (indicated by vertical bars) increases with τ for the ET (Fig. 1.5a), but remains nearly constant for the WS (Fig. 1.5c). ET laboratory D results are similar to the surfzone, where combined bubble/sand results are the closest to the field (Fig. 1.5a). WS lab results are also similar to the surfzone (Fig. 1.5c), but only the bubble perturbed test produced the full range of observed surfzone turbidity (because of the strongly non-linear τ response to sand, Section 1.4.2).

Spurious dye measurements are small, however the integral over many spurious measurements in time (ET) or space (WS) can effect dye concentration statistics (e.g., total dye mass, dye patch/plume width). For example, if the WS was driven on a cross-shore transect without dye in the water, the inclusion of spurious dye measurements would suggest that dye, and the resulting plume/patch width, spanned the entire transect. To remove spurious dye measurements for both instruments in the surfzone, a lower

bound for dye detection D_{low} is estimated by a fit to $D > 99\%$ of the spurious surfzone D in each bin versus binned τ. The disadvantage to this approach is that it sets a lower limit on measurable dye concentration, and the resultant size and duration that a dye patch/plume can be observed. However, it is suggested that D below D_{low} be set equal to zero to avoid biasing dye statistics. The fit (Fig. 1.5a,c dashed black line) to surfzone field data without dye for each instrument respectively is

$$D_{\text{low}} = \alpha\tau + C \,, \tag{1.1}$$

where α and C are fit constants, and D_{low} is in ppb. For the ET $\alpha = 0.02$ ppb $\cdot$ ntu^{-1}, and $C = 0.3$ ppb, and for the WS $\alpha = 0.01$ ppb $\cdot$ ntu^{*-1}, and $C = 0.46$ ppb.

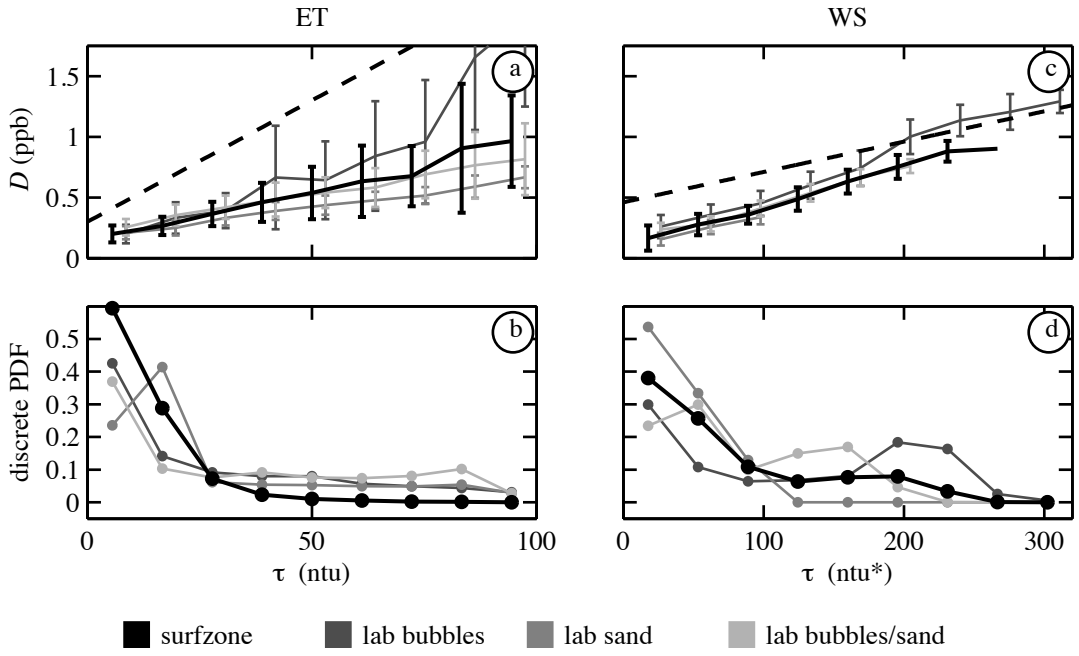

Figure 1.5: Field and laboratory results without dye in the water for (left panels) ET and (right panels) WS. (a,c) Spurious D versus τ (solid curves), and D_{low} fit (dashed curve) from (1.1). (b,d) Discrete probability density functions (PDFs) of τ corresponding to top panels. D is given as binned means, with vertical bars indicating $\pm$ one STD. ET field data (solid black curves) combine several cross-shore locations within the surfzone, and field data for the WS combine multiple cross-shore transects. Laboratory data are given for τ from bubbles, from sand, and from bubbles and sand combined (see legend). Between 1200 (lab) and 28,000 (field) samples are used to construct ET curves, and 1180 (field) to 5398 (lab) samples for each of the WS curves

1.6.2 Laboratory with dye

Four known dye concentrations (D_0) were perturbed with bubbles (Fig. 1.6a,d), sand (Fig. 1.6b,e), and a combination of bubbles and sand (Fig. 1.6c,f) for ET (Fig. 1.6a-c) and WS (Fig. 1.6d-f) respectively. Changes in measured dye concentration D are given as percent change $\%\Delta D$ from the unperturbed known D_0

$$\%\Delta D = 100\,(D - D_0)/D_0\ . \tag{1.2}$$

The mean $\%\Delta D$ is almost always negative (i.e., quenching), and is similar for all dye concentrations (curves within each panel of Fig. 1.6 overlay each other). This concentration independent $\%\Delta D$ is consistent with *Smart and Laidlaw* [1977] for τ induced quenching of Rhodamine WT, but contrasts with the concentration dependent τ induced quenching of chlorophyll-a [*Omand et al.*, 2009]. The STD (vertical bars) about the mean $\%\Delta D$ increases with τ for the ET, and to a lesser extent for the WS. The relationship between ET $\%\Delta D$ and τ is similar for bubbles, sand, and bubbles and sand combined (i.e., curves in all left panels are similar), and the maximum decrease ($\%\Delta D \approx$ -20%, binned mean minus one STD) due to τ occurs at near full scale turbidity values. However, bubbles effect the WS differently than sand (Fig. 1.6d,e), with bubbles producing τ up $300\ \mathrm{ntu}^*$ with moderate quenching effects (binned mean $\%\Delta D$ minus one STD as large as -25%), and sand producing τ up to $75\ \mathrm{ntu}^*$ with large quenching effects (binned mean $\%\Delta D$ minus one STD as large as -40%). The large WS sand quenching effect at moderate τ values is consistent with very high sand concentrations (that block fluoresced light) required to approach the $75\ \mathrm{ntu}^*$ saturation point for sand induced τ (Fig. 1.4).

1.7 Dye measurement corrections

Dye measurement errors are reduced by discarding dye data points with turbidity τ above a threshold, and correcting the remaining dye for τ induced quenching. ET data were removed when $\tau > 90\ \mathrm{ntu}$ to exclude the increased scatter in quenching (Fig. 1.6c) near and beyond the instrument τ saturation point (100 ntu). WS data were removed when $\tau > 300\ \mathrm{ntu}^*$, the highest lab observed τ (and thus the limit of lab based

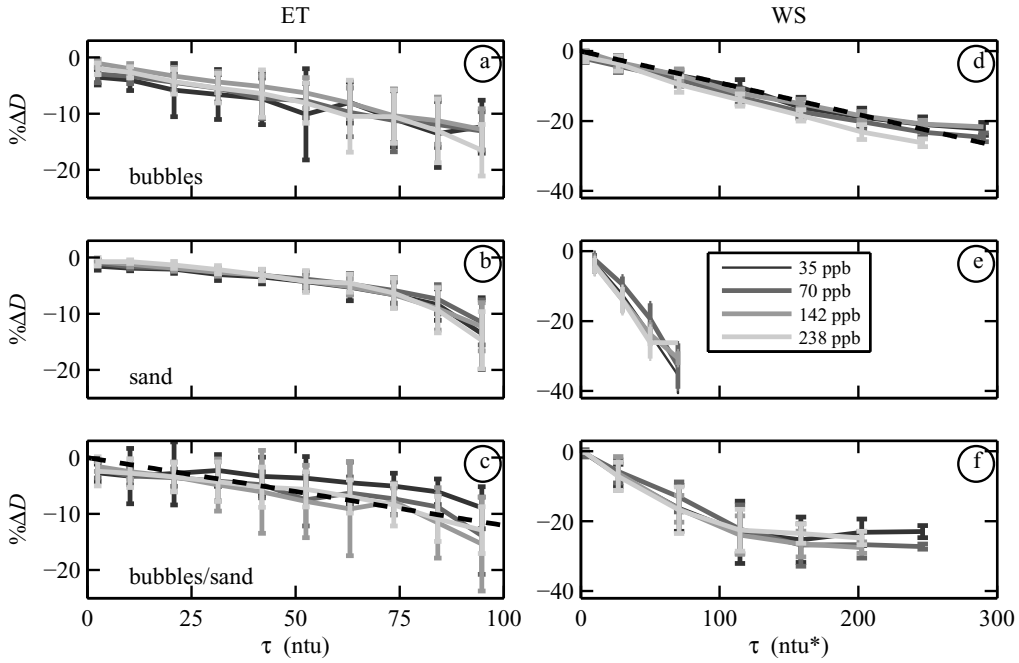

Figure 1.6: Percent change in measured dye $\%\Delta D$ (1.2) versus τ from (a,d) bubbles, (b,e) sand, and (c,f) bubbles and sand combined, for (left panels) ET and (right panels) WS with four dye concentrations in the lab (see legend). $\%\Delta D$ are given as binned means, with vertical bars indicating $\pm$ one STD. Between 550 and 860 ET, and 3600 and 5400 WS samples are used to construct each curve. Dashed black lines in (c) and (d) show fits (1.5) to binned mean data

τ correction). The combination of discarding high τ data and correcting the remaining D for τ induced quenching is hereafter called correction.

Surfzone fluorometers encounter bubbles and sand suspended by breaking waves and strong currents. The ET turbidity sensor cannot distinguish between bubbles and sand. However, the effects of bubble and sand induced τ on ET dye quenching are similar (Fig. 1.6a,b), and the curve derived from the combination of bubbles and sand (dashed line in Fig. 1.6c) is used for ET corrections. In contrast, bubbles and sand induced τ produce very different dye quenching effects in the WS (Fig. 1.6d,e), but as with the ET, the instrument cannot distinguish between τ from bubbles and τ from sand. In the present application the jet ski mounted WS system samples water 20 cm below the surface where average sand concentrations are expected to rarely exceed $1\ \mathrm{g\,L^{-1}}$ [e.g., *Beach and Sternberg*, 1992; *Yu et al.*, 1993; *Beach and Sternberg*, 1996; *Ogston and Sternberg*, 2002]. Even extreme sand concentrations ($> 20\ \mathrm{g\,L^{-1}}$) only result in τ up to $75\ \mathrm{ntu}^*$ (Fig. 1.4) with the WS τ sensor, leaving about one third of the field data with higher τ than sand alone can produce (Fig. 1.5d). Therefore, bubbles are assumed to be the τ source, and WS dye measurement corrections are made using the bubble quenching curve (Fig. 1.6d).

The relationship between binned mean $\%\Delta D$ (1.2) and τ are used to correct for τ induced dye quenching. The fits to ET bubbles and sand combined (Fig. 1.6c, dashed black line), and WS bubbles only (Fig. 1.6d, dashed black line) have the form

$$\%\Delta D = 100\,\beta\tau\ . \tag{1.3}$$

Substituting (1.2) into (1.3) yields

$$\frac{D - D_0}{D_0} = \beta\tau\ , \tag{1.4}$$

where the fit constant is $\beta = 1.2 \times 10^{-3}\ \mathrm{ntu}^{-1}$ (ET), and $\beta = 0.91 \times 10^{-3}\ \mathrm{ntu}^{*-1}$ (WS). Equating D_0 to corrected dye concentration D_c, and D to the raw dye concentration D_r, (1.4) yields the equation to correct D_r for τ induced quenching

$$D_\mathrm{c} = \frac{D_\mathrm{r}}{1 - \beta\tau}\ . \tag{1.5}$$

In laboratory tests with known $D_0 = 70\ \mathrm{ppb}$ (Fig. 1.7), the magnitude of raw $\%\Delta D_\mathrm{r}$ (1.2) is increased by τ induced quenching during periods of high turbidity.

Corrected dye concentrations $D_{\rm c}$ are usually more accurate than raw $D_{\rm c}$ ($|\%\Delta D_{\rm c}| < |\%\Delta D_{\rm r}|$). Occasionally, $D_{\rm r}$ is quenched when τ is low (e.g., at $t = 80$ s, Fig. 1.7a), and significant errors ($\sim 15\%$) remain in corrected $D_{\rm c}$. Discarding ET measurements with $\tau > 90$ ntu (light gray vertical bars) removed the large spike at $t = 60$ s (Fig. 1.7a) when the τ sensor was saturated. Results are qualitatively similar for other D_0 (not shown).

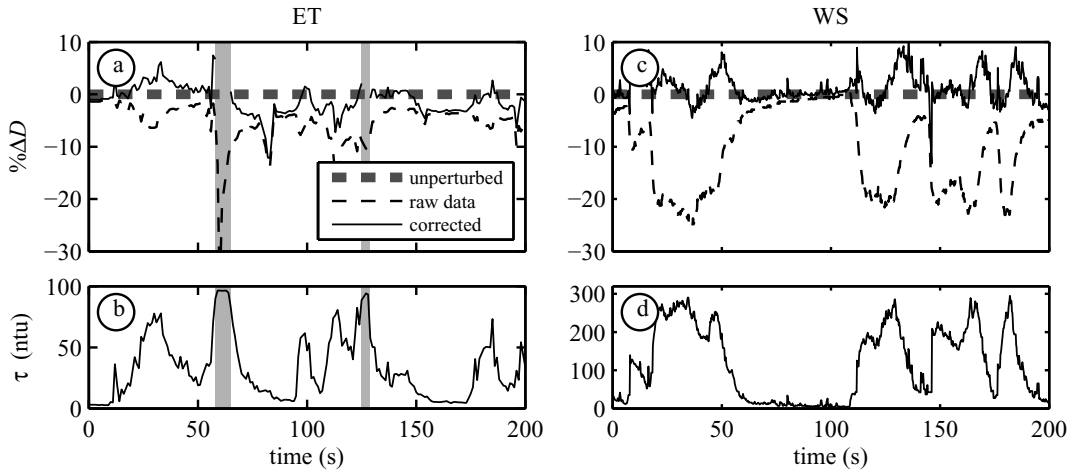

Figure 1.7: Laboratory examples of (a,c) percent change in raw $\%\Delta D_{\rm r}$ (dashed black curve) and corrected $\%\Delta D_{\rm c}$ (with (1.5), solid black curves) dye concentration and (b,d) turbidity τ versus time, for (left panels) ET and (right panels) WS. Thick dashed gray line is the unperturbed $\%\Delta D = 0$. For the ET (WS) seawater with a known $D_0 = 70$ ppb dye concentration was perturbed with bubbles and sand (bubbles only). (a) Light gray vertical bands indicate times when $\tau > 90$ ntu. At $t \approx 60$ s, the ET τ sensor is saturated at ≈ 100 ntu

Errors in raw $D_{\rm r}$ and corrected $D_{\rm c}$ (discarding high τ data and using (1.5)) are calculated from laboratory data perturbed with a combination of bubbles and sand (bubbles only) for the ET (WS) with four dye concentrations (Table 1.1). For both raw and corrected data, percent root-mean-square errors $\%\epsilon_{\rm rms} = 100 \times \langle (D_{r,c} - D_0)^2 \rangle^{1/2} / D_0$ and mean errors $\%\epsilon_{\rm m} = 100 \times \langle D_{r,c} - D_0 \rangle / D_0$ are given (Table 1.1), where $\langle\rangle$ indicates a time average. Raw percent error magnitudes are independent of concentration, and are generally $< 9\%$ ($< 13\%$) for ET (WS). For both ET and WS, correction reduces rms ($|\%\epsilon_{\rm rms}| < 5\%$) and mean ($|\%\epsilon_{\rm m}| < 2\%$) errors. Error propagation into spatial dye moments is non-trivial, and depends on the shape of the dye distribution, how realiza-

Table 1.1: Percent errors (rms $\%\epsilon_{\rm rms}$, and mean $\%\epsilon_{\rm m}$) in the laboratory with known dye concentration D_0 (left column) perturbed with bubbles and sand (ET), and bubbles (WS). $\%\epsilon_{\rm rms}$ and $\%\epsilon_{\rm m}$ are given for raw data, and data corrected by removing high turbidity (ET $\tau > 90$ ntu, WS $\tau > 300$ ntu) dye mesurements and using (1.5)

	ET				WS			
	$\%\epsilon_{\rm rms}$		$\%\epsilon_{\rm m}$		$\%\epsilon_{\rm rms}$		$\%\epsilon_{\rm m}$	
D_0 (ppb)	raw	corrected	raw	corrected	raw	corrected	raw	corrected
35	6.0	5.0	-3.9	0.7	12.1	2.7	-9.3	-0.3
70	8.3	4.9	-6.7	-1.6	12.0	1.8	-8.9	-0.1
142	8.5	5.0	-5.8	-1.1	12.4	1.4	-10.4	-0.4
238	6.6	3.3	-4.7	-1.0	11.8	2.6	-8.9	-1.8

tions are averaged, and the assumed noise decorrelation scale. However, for a simple Gaussian example with 5% rms noise and a noise decorrelation scale equal to one STD of the Gaussian itself, the rms error in measured variance is 2%.

Examples of corrections to surfzone dye measurements are shown for ET (Fig. 1.8) and WS (Fig. 1.9). ET τ induced quenching corrections $D_{\rm c} - D_{\rm r}$ are small (< 4 ppb, Fig. 1.8b) compared to dye variability (Fig. 1.8a). WS corrections are similarly small (< 1 ppb on the inbound transect), but reach 9 ppb on the outbound transect when τ is elevated by bubbly water is drawn into the flow-through system when the jet ski drives over bubble filled bores (Fig. 1.10b). On inbound transects, bubbles are reduced by driving just in front of the shoreward traveling bore (Fig. 1.10a). WS corrected $D_{\rm c}$ on sequential inbound and outbound transects have closer peak values than $D_{\rm r}$.

High turbidity events associated with increased error are less frequent in the field than the lab (Fig. 1.5b), thus ET dye measurement errors in the surfzone are expected to be smaller than in the laboratory (Table 1.1). In contrast, WS field errors may be increased relative to laboratory errors by rare high concentration sand events that are unaccounted for in lab estimates.

1.8 Summary

Open-face (ET) and flow-through (jet ski mounted WS) Rhodamine WT fluorometers for *in situ* surfzone sampling were tested. Surfzone bubbles and sand (measured as turbidity τ) interfere with fluorescent dye measurements both raising the lower bound for dye detection $D_{\rm low}$ (1.1), and reducing (quenching) measured dye fluores-

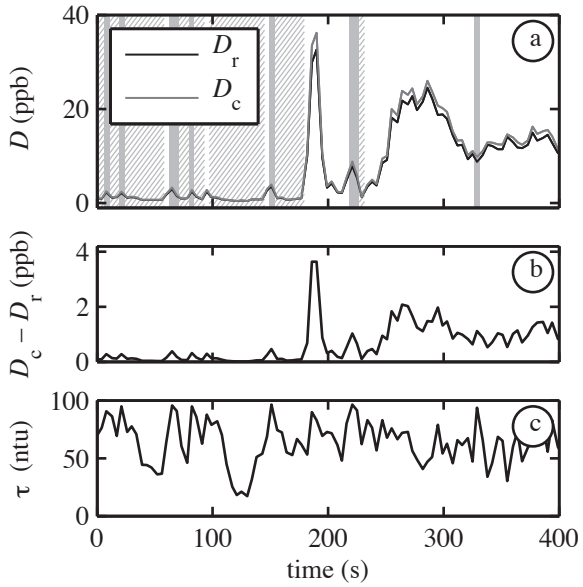

Figure 1.8: ET (a) raw and corrected dye concentration ($D_{\rm r}$, $D_{\rm c}$), (b) correction magnitude ($D_{\rm c} - D_{\rm r}$), and (c) τ versus time in the surfzone. The instrument was mounted 65 m from the shoreline, 50 cm above the bottom. A dye patch (0.25 liters of 21% by weight Rhodamine WT) was released 10 m alongshore from the ET at $t = 150$ s. (a) $D_{\rm c}$ (gray curve) is estimated from $D_{\rm r}$ (black curve) and (c) corresponding τ time series, using (1.5). Light gray vertical bands indicate times when $\tau > 90$ ntu (data are removed). Light gray hatching indicates times when $D_{\rm r} < D_{\rm low}$ (1.1), and $D_{\rm r,c}$ should be set to zero

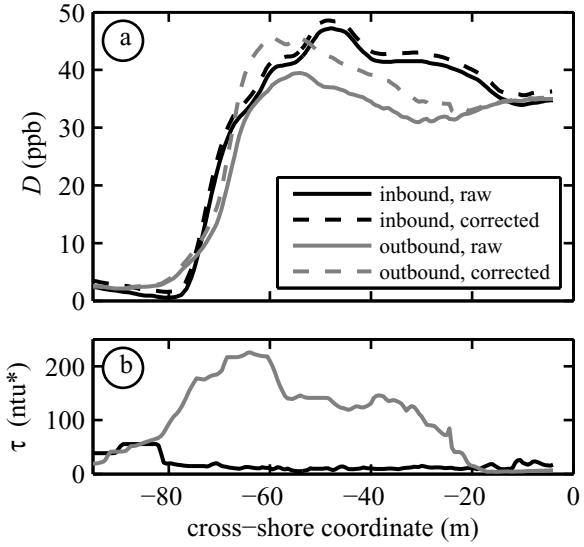

Figure 1.9: WS (a) D and (b) τ versus cross-shore coordinate (positive onshore, with shoreline at zero), for a single cross-shore transect pair, 575 m alongshore from the dye source during a continuous release in the surfzone. Inbound and outbound transect raw D and τ, and corrected D are shown (see legend). Inbound corrected dye curve is vertically offset by +1 ppb for visibility. $D > D_{\text{low}}$, and root-mean-square D_{low} was 0.56 and 0.62 ppb for inbound and outbound transects respectively. About 1 minute of data are shown

Figure 1.10: (a) Inbound and (b) outbound cross-shore transects through the surfzone with the jet ski mounted WS. (a) Inbound transect bubbles are minimized by driving just in front of a shoreward traveling bore. (b) On outbound transects, bubbly water is drawn into the flow-through WS system as the jet ski drives over a bore

cence D (Fig. 1.6). Laboratory experiments with known dye concentrations D_0 in seawater were perturbed with bubbles, sand, and bubbles and sand combined to explore the effect of τ on D. The reduction in measured D increases with τ, and the observed relationship is used to correct surfzone dye estimates. Percent root-mean-square $\%\epsilon_{\rm rms}$ and mean $\%\epsilon_{\rm m}$ errors for the ET and WS are reduced to $< 5\,\%$ by discarding high τ data and using (1.5). *In situ* Rhodamine WT measurements are feasible in the surfzone, allowing comprehensive tracer mixing and transport experiments in this heavily used but poorly understood region of the ocean.

1.9 Chapter 1 Appendix: Flow-through mixing and delay time

Continuously pumped water in the WS flow-through system (Fig. 1.3) is mixed (in hoses and the debubbler), smoothing out sharp gradients in dye concentration. In addition, water takes several seconds (delay time) to move through the hoses and debubbler before reaching the fluorometer. This delay time must be accounted for to match GPS

positions with dye measurements. Smoothing and delay time are specific to the pump, hoses (length, diameter, and roughness), and debubbler (not commercially available) used in the WS flow-through system. The specific smoothing and delay time estimates in the WS system are presented here to provide context for the result presented above, and to establish a framework for characterizing similar systems in the future.

Smoothing in the WS flow-through system was estimated with laboratory experiments using step functions of dye (created by switching the intake between water with zero and a known dye concentration with a Y-valve, Fig. 1.11). The 2.4 s 10-90% rise time gives the temporal smoothing scale. This smoothing in time gives rise to smoothing in space, which depends on jet ski speed (i.e.,2.4 s multiplied by jet ski speed). For example, at a typical jet ski speed of 4 $\mathrm{m\,s^{-1}}$(the linear wave speed in 1.6 m water depth), the distance between independent samples is about 9.6 m. The WS flow-through system, essentially a low-pass filter, results in smoothing for dye concentration frequencies greater than about $(2.4\ s)^{-1}$ entering the WS system. The severity of the smoothing increases with frequency, and is reduced by using slower jet ski speeds (thus reducing frequency). The smoothing magnitude can be estimated from the assumed true dye wavenumber spectrum, and the jet ski speed.

The WS flow-through system, essentially a low-pass filter, results in smoothing for dye concentration frequencies greater than about $(2.4\ s)^{-1}$ entering the WS system. The severity of the smoothing increases with frequency, and is reduced by using slower jet ski speeds (thus reducing frequency). The smoothing magnitude can be estimated from the assumed true dye wavenumber spectrum, and the jet ski speed.

Sequential inbound-outbound transect pairs were used to find WS system delay times by minimizing the difference between the inbound and the outbound cross-shore dye concentrations (similar to Fig. 1.12). From 64 transects pairs a delay of 8 s was the most common value (i.e.,the mode), with a mean delay of 8.1 s. The 8 s value was used to time correct the WS field data. In examples of WS D versus cross-shore distance, sequential inbound and out bound transects are closer in shape and location after time correction (Fig. 1.12). The addition of a flow rate sensor is planned to more accurately estimate the delay time. The STD of the field delay times, ± 0.84 s, results in spatial uncertainty that depends on jet ski speed. For example, the spatial uncertainty is

approximately ± 3.3 m at 4 $\mathrm{m\,s^{-1}}$speed.

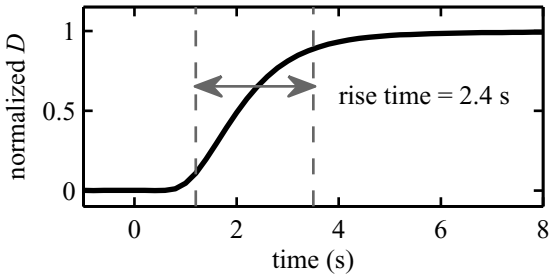

Figure 1.11: Mean (over 5 step functions) time series of normalized WS dye concentration (black curve) in response to a dye step function input. The system output shows a 10-90% rise time (between dashed gray lines) of 2.4 s, due to mixing in the flow-through system hoses and the debubbler

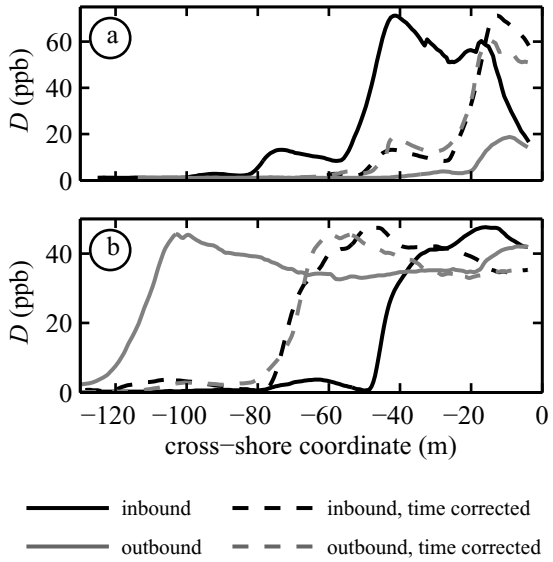

Figure 1.12: WS dye D versus cross-shore coordinate (positive onshore, with shoreline at zero), for single inbound (black) and outbound (gray) cross-shore transect pairs, (a) 50 m and (b) 575 m alongshore from the dye source during a continuous release. Time corrected inbound and outbound curves (dashed) are similar, suggesting that system delay time in raw data (solid) is accounted for

Chapter 1, in full, is a reprint of the material as it appears in Air Water and Soil Pollution, 2009, Clark, David B.; Feddersen, Falk; Omand, Melissa; Guza, R.T.,

Springer, 2009. The dissertation author was the primary investigator and author of this paper.

Chapter 2

Dye Tracer Field Experiment

2.1 Abstract

Cross-shore surfzone tracer dispersion in a wave driven alongshore current is examined over a range of wave and current conditions with 6 continuous dye releases, each roughly 1–2 hours in duration, at Huntington Beach, California. Fluorescent dye tracer released near the shoreline formed shore parallel plumes that were sampled on repeated cross-shore transects with a jet ski mounted fluorometer. Ensemble averaged cross-shore tracer concentration profiles are generally shoreline attached (maximum at or near the shoreline), with increasing cross-shore widths and decreasing peak values with downstream distance. More than a few 100 m from the source, tracer is often well mixed across the surfzone (i.e., saturated) with decreasing tracer concentrations farther seaward. For each release, cross-shore surfzone absolute diffusivities are estimated using a simple Fickian diffusion solution with a no-flux boundary at the shoreline, and range from 0.5–2.5 $\mathrm{m^2\,s^{-1}}$. Surfzone diffusivity scalings based on cross-shore bore dispersion, surfzone eddy mixing length, and undertow-driven shear dispersion are examined. The mixing-length scaling has correlation $r^2 = 0.59$ and the expected best-fit slope < 1, indicating that horizontal rotational motions are important for cross-shore tracer dispersion in the surfzone.

2.2 Introduction

Beaches and the adjacent surfzone are used for recreational and commercial activities, and provide habitat to a variety of fish and benthic species. Beach related tourism provides yearly revenue of about 1 billion dollars in Los Angeles and Orange Counties, California, U.S.A. [*Hanemann et al.*, 2001]. These economic and environmental resources are threatened by polluted terrestrial runoff that frequently drains onto the shoreline where it is entrained and spread in the surfzone [*Boehm et al.*, 2002]. Waterborne pollution threatens public health, causing both gastrointestinal and upper respiratory symptoms in exposed beachgoers [*Haile et al.*, 1999], and results in frequent beach closures [*Noble et al.*, 2000]. A model predicting the transport and dilution of surfzone pollutants would improve beach management. However, the processes that mix tracers within the surfzone are understood poorly.

Fluorescent dye tracers have been used to investigate surfzone mixing and transport [*Harris et al.*, 1963; *Inman et al.*, 1971; *Grant et al.*, 2005; *Clarke et al.*, 2007]. Visually observed tracer patches initially dispersed cross-shore until the surfzone was saturated (approximately uniform cross-shore dye concentration), followed by dominant alongshore dispersion [*Harris et al.*, 1963; *Inman et al.*, 1971; *Clarke et al.*, 2007]. After several hours, surfzone tracer patches were observed to stretch 5-8 km alongshore while remaining within a few surfzone widths of the shoreline [*Grant et al.*, 2005]. Seaward of the surfzone, visually slower dispersion suggested that mixing was weaker than within the surfzone.

A wide range of field estimated surfzone diffusivities ($\kappa \sim 10^{-3} - 10^{4}\ \mathrm{m^2\,s^{-1}}$) have been found by fitting dye tracer data to Fickian diffusion solutions assuming constant alongshore currents and depth [*Harris et al.*, 1963; *Inman et al.*, 1971; *Clarke et al.*, 2007]. *Harris et al.* [1963] estimated alongshore diffusivity κ_{yy} by measuring dye concentrations from bottle samples collected at several shoreline locations during both point and continuous tracer releases. *Inman et al.* [1971] sampled point released dye with bottles at the shoreline and at the visually estimated dye patch center. *Clarke et al.* [2007] estimated diffusivities by fitting a 2-D advection diffusion solution to point dye releases that were bottle sampled at several shoreline locations.

Cross-shore tracer structure was not observed in previous surfzone field studies

[*Harris et al.*, 1963; *Inman et al.*, 1971; *Clarke et al.*, 2007]. Diffusivity estimates were derived from single realizations in space and time, without the ensemble averaging over plume and patch fluctuations needed for stability in diffusivity estimates [e.g., *Csanady*, 1973]. In addition, local waves and currents were generally not measured, complicating the interpretation of diffusivity parameterizations.

Laboratory experiments using shore-normal monochromatic waves without [*Harris et al.*, 1963] and with [*Pearson et al.*, 2009] an imposed alongshore current have been used to study surfzone tracer dispersion. *Harris et al.* [1963] estimated a combined cross- and alongshore diffusivity κ, and used turbulent dissipation and an eddy length scale to derive a $\kappa \sim H_{\rm b}^2 T_{\rm b}^{-1}$ scaling, where $H_{\rm b}$ was the breaking wave height and $T_{\rm b}$ was the mean breaking wave period. *Pearson et al.* [2009] estimated a cross-shore diffusivity κ_{xx} from mean cross-shore dye profiles at several locations downstream from a continuous dye source, and proposed a cross-shore shear dispersion scaling using the sheared mean cross-shore current (undertow) and a vertical diffusivity.

Using a shoreward propagating region of diffusivity to represent the mixing effects of a broken wave (bore), the effects of single and multiple waves on cross-shore tracer concentrations were investigated using numerical models [*Feddersen*, 2007]. A non-dimensional cross-shore average diffusivity $\bar{\hat{\kappa}} = \sqrt{\pi}/(\hat{c}\hat{T})$ was derived where $\hat{c}$ and $\hat{T}$ are the non-dimensional cross-shore wave speed and wave period [*Feddersen*, 2007; *Henderson*, 2007].

Drifters have also been used to estimate surfzone diffusivities. On roughly alongshore uniform beaches, drifter estimated diffusivities were time-dependent with asymptotic (long-time) κ_{xx} between $0.5 - 1.5\ {\rm m^2\,s^{-1}}$ and asymptotic κ_{yy} between $2 - 18\ {\rm m^2\,s^{-1}}$ [*Spydell et al.*, 2007, 2009]. Good agreement was found between the asymptotic κ_{yy} and both mixing-length and shear dispersion scalings. At beaches with irregular bathymetry that control circulation (i.e., rip channels), estimated asymptotic diffusivities were $\kappa_{xx} = 0.9 - 2.2\ {\rm m^2\,s^{-1}}$ and $\kappa_{yy} = 2.8 - 3.9\ {\rm m^2\,s^{-1}}$ [*Brown et al.*, 2009], and estimated relative diffusivities were $\kappa_{xx} \approx -0.8 - 2\ {\rm m^2\,s^{-1}}$ and $\kappa_{yy} = 1.8 - 4.8\ {\rm m^2\,s^{-1}}$ [*Johnson and Pattiaratchi*, 2004]. Unlike tracers, drifters duck under breaking waves and are not entrained in the front face of a bore. Diffusivities for drifters and tracers may differ.

Here, field observations of continuously released surfzone dye tracer plumes in quasi-steady alongshore currents on generally alongshore uniform bathymetry are presented. Tracer experiments are conducted over a range of wave and current conditions (Section 2.3.1). Dye released into the surfzone (Section 2.3.2) is measured on repeated cross-shore transects by a dye sampling jet ski (Section 2.3.3). Using ensemble (absolute) averaged cross-shore concentration profiles, cross-shore integrated tracer statistics are estimated (Section 2.4). Variation in individual tracer profiles, the structure of mean profiles, and the downstream evolution of tracer profile statistics are described in Section 2.5. A simple Fickian diffusion model for tracer released at the shoreline with a no-flux shoreline boundary (Section 2.6.1) is used to estimate surfzone absolute κ_{xx} (Section 2.6.2) from mean dye profiles that are well contained in the surfzone. The Fickian solution is compared with observed tracer moments (Section 2.6.3). The observed surfzone κ_{xx} are compared with other surfzone κ_{xx} estimates (Section 2.7.1), and inferences are made about the relative strength of mixing seaward of the surfzone (Section 2.7.2). Three κ_{xx} scalings and related dispersion mechanisms are discussed (Section 2.7.3), and the possible causes of decreased tracer transport between the dye release pump and downstream transects are examined (Section 2.7.4). Section 2.8 is a summary.

2.3 HB06 experiment

2.3.1 Field site, waves and currents

The HB06 experiment took place from September 14th to October 17th, 2006 in Huntington Beach, California located 50 km south of Los Angles. The approximately straight, 1 km long study beach faces 214° southwest. Offshore islands strongly effect the incident waves by blocking shore-normal southwesterly swells, and obliquely incident waves from the west or south often drive strong alongshore currents.

The X and Y coordinates are the cross-shore distance from the mean sea level (MSL) shoreline, and the alongshore distance from the instrumented transect (Figure 2.1), respectively. Bathymetry (Figure 2.1a) was surveyed three times on 42 cross-shore transects using a GPS equipped jet ski, ATV, and hand pushed cart [*Seymour et al.*,

2005]. The alongshore and time-averaged bathymetry slope is 0.03 seaward of about 2 m depth, decreases to 0.006 between roughly 0.7 m and 2 m depth, and steepens to 0.075 on the beach face (Figure 2.1b). Changes in the seaward portion of the bathymetry over time were small. However, a small trough near the shoreline early in the observations subsequently accreted (shaded region between $-50 < X < -10$ m in Figure 2.1b). The tidal range is typically less than ± 1 m.

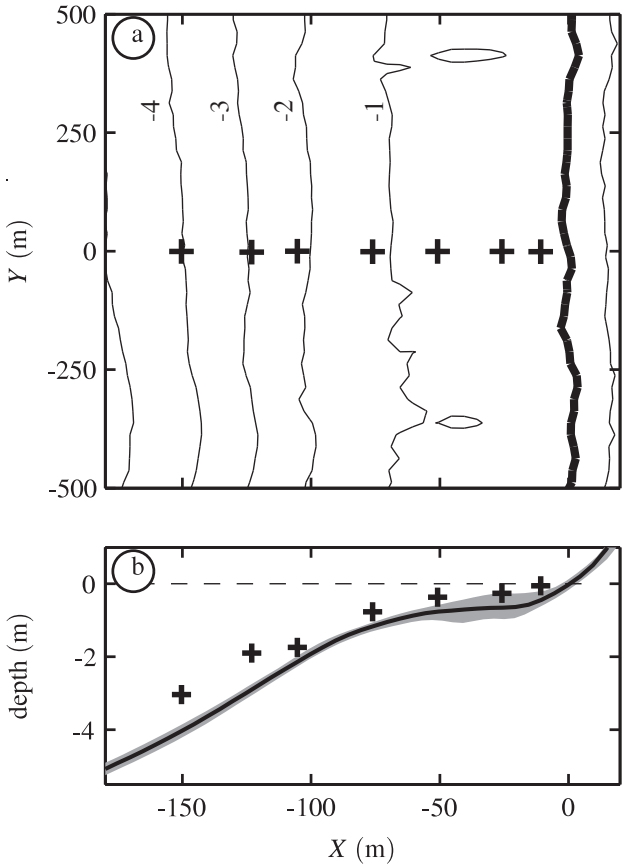

Figure 2.1: (a) Plan view of HB06 bathymetry (depth) contours versus cross-shore distance X from the MSL shoreline, and alongshore distance Y from the instrumented frames (black crosses). Thin curves are depth contours (labeled in m) and the thick black contour is at mean sea level (MSL). (b) Mean depth versus X, with depth equal to zero at the MSL shoreline (dashed black line). The gray region indicates the bathymetry standard deviation over Y and time, and black crosses indicate approximate vertical instrument locations.

Seven tripod frames with pressure sensors and acoustic Doppler velocimeters

(ADVs) were deployed in a 160 m long cross-shore array from near the shoreline to 4 m mean depth (Figure 2.1a). Frames are numbered from 1 (shallowest) to 7 (deepest). Frame 7 was always seaward of the surfzone. Frame 1 was 11 m from the MSL shoreline, and the ADV was out of the water during low tides.

During the six HB06 dye release experiments (R1 through R6) the dominant south swell drove surfzone alongshore currents and dye in the $+Y$ (upcoast) direction. For each dye release, x is the cross-shore distance from the mean shoreline (tide dependent), and y is the alongshore distance from the continuous dye source. Significant wave heights $H_{\rm s}(x)$, alongshore currents $V(x)$, and horizontal (low-frequency) rotational velocities $\mathcal{V}_{\rm rot}(x)$ [*Lippmann et al.*, 1999] were measured at each frame (Figure 2.1) and averaged over the duration of each release (Figure 2.2 and Table 2.1). The $H_{\rm s}(x)$ are estimated from pressure spectra (depth corrected to the surface) over the sea-swell band. Following *Lippmann et al.* [1999], low frequency vortical motions $\mathcal{V}_{\rm rot}(x)$ are estimated by removing irrotational infragravity wave energy from the observed velocity via

$$\mathcal{V}_{\rm rot}(x) = \sqrt{\int_{\rm IG} (S_{uu} + S_{vv} - \frac{g}{h} S_{pp}) df}, \tag{2.1}$$

where S_{uu}, S_{vv}, and S_{pp} are the cross-shore, alongshore, and pressure spectra respectively, f is frequency, and the integral is over the infragravity band ($0.004 < f < 0.03$ Hz). This $\mathcal{V}_{\rm rot}(x)$ estimate approximates shear wave velocity variance [*Noyes et al.*, 2002].

For releases R1 through R5, $H_{\rm s}(x)$ shoaled to a maximum near $x = -110$ m then decreased towards the shoreline as broken waves dissipated (Figure 2.2a). For R1-R5, $V(x)$ and $\mathcal{V}_{\rm rot}(x)$ had similar cross-shore structure with mid-surfzone maxima (Figure 2.2b,c). Wave heights during R6 were smaller than the other releases, reaching a maximum closer to the shoreline ($x = -88$ m), with a weak $H_{\rm s}(x)$ decay towards the shoreline (Figure 2.2a). Unlike R1 through R5, R6 also had $V(x)$ and $\mathcal{V}_{\rm rot}(x)$ (Figure 2.2b,c) maxima close to the shoreline.

Averaged over each release, the incident (Frame 7) $H_{\rm s}$ range from 0.41 to 1.02 m, mean wave periods $T_{\rm m}$ from 9.0 to 9.9 s (from energy weighted pressure spectra over the sea-swell band), incident wave angle (θ) from 0.9 to 9.8 degrees downcoast (after significant shoaling and refraction), and directional spread from 14.6 to 23.1 degrees

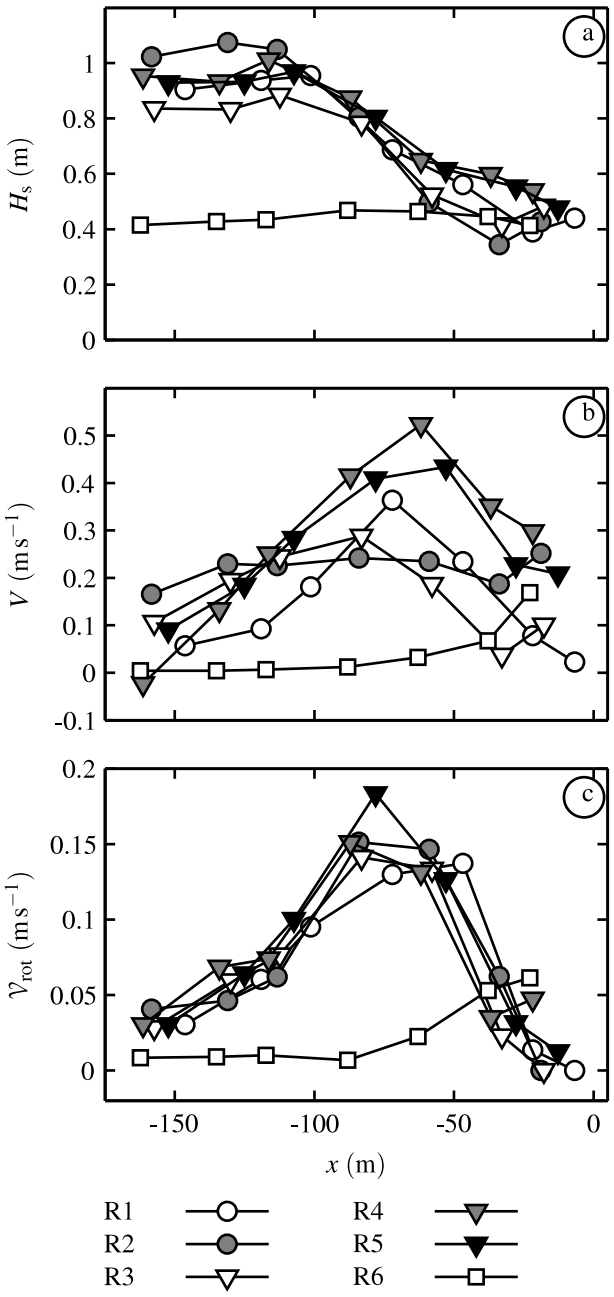

Figure 2.2: (a) Significant wave height H_s, (b) mean alongshore current V, and (c) horizontal rotational velocities $\mathcal{V}_{rot}$ versus cross-shore distance from the shoreline x for each dye release (see legend).

Table 2.1: Wave and current statistics for each dye release: release number, release date, incident (frame 7) mean significant wave height $H_{\rm s}$, mean period $T_{\rm m}$, wave angle θ and directional spread σ_θ, and surfzone averaged mean alongshore current $\overline{V}$, surfzone averaged horizontal rotational velocity $\overline{\mathcal{V}}_{\rm rot}$, and surfzone width L_x.

Release	date	$H_{\rm s}$ (m)	$T_{\rm m}$ (s)	θ (deg)	σ_θ (deg)	$\overline{V}$ ($\rm m\,s^{-1}$)	$\overline{\mathcal{V}}_{\rm rot}$ ($\rm m\,s^{-1}$)	L_x (m)
R1	Sept-18	0.90	9.5	9.8	14.6	0.18	0.075	101
R2	Sept-22	1.02	9.1	0.9	23.1	0.23	0.082	122
R3	Sept-28	0.84	9.9	7.8	17.8	0.21	0.073	112
R4	Sept-29 am	0.95	9.1	6.5	18.3	0.37	0.088	116
R5	Sept-29 pm	0.93	9.0	6.3	17.8	0.31	0.090	116
R6	Oct-11	0.41	9.2	7.0	15.3	0.07	0.036	88

(Table 2.1). The surfzone width L_x is between 88 m and 122 m, with the seaward edge of the surfzone $x = -L_x$ defined as the cross-shore location of the $H_{\rm s}$ maximum (Table 2.1). Cross-shore averaging over the frames within the surfzone results in surfzone averaged mean alongshore currents ($\overline{V}$) between 0.07 and 0.37 $\rm m\,s^{-1}$, and surfzone averaged $\overline{\mathcal{V}}_{\rm rot}$ between 0.036 and 0.090 $\rm m\,s^{-1}$(Table 2.1).

2.3.2 Dye release methods

Concentrated Rhodamine-WT dye (21% by weight) was released continuously at $1.3 - 7.1$ $\rm mL\,s^{-1}$ into the surfzone during mid- to high tide. The cross-shore dye release location x_0 (in about 1 m depth) varied between 4 and 22 m, with one release (R1) much farther offshore at $x_0 = 54$ m (Table 2.2). A battery powered peristaltic pump mounted on a 2 m tall heavy metal cart forced dye through a small tube to 0.5 meters above the bed, terminating into a small 10 cm long diffuser hose. Rapid vertical mixing was visually observed, and measured surface dye concentrations were reduced to 400 parts per billion (ppb) within a few meters of the source indicating that concentrated dye (1.2 specific gravity) was quickly diluted to a specific gravity near 1. Although dye was not measured near the bed, dye is expected to be vertically well-mixed due to vigorous surfzone mixing. The possibility of vertically varying dye is discussed in Section 2.7.4.

Table 2.2: Dye sampling parameters for each release: release number, sampling duration, cross-shore dye release location x_0, inner transect integration limit $x_{\rm in}$, number of downstream transect locations, average number of realizations on each transect $\langle N_j \rangle^{(j)}$ (where $\langle \cdot \rangle^{(j)}$ is the average over all transect locations j), average degrees of freedom on each transect $\langle \mathcal{N}_j \rangle^{(j)}$, and the estimated Eulerian decorrelation time $\tau_{\rm decorr}$. For R3 and R6, data to estimate $\tau_{\rm decorr}$ were not available so the largest estimate ($\tau_{\rm decorr} = 135$ s) is used, and marked with an asterisk.

Release	duration (minutes)	x_0 (m)	$x_{\rm in}$ (m)	transects	$\langle N_j \rangle^{(j)}$	$\langle \mathcal{N}_j \rangle^{(j)}$	$\tau_{\rm decorr}$ (s)
R1	66	-54	-13	3	15.3	15.3	41
R2	40	-13	-11	5	9.8	7.5	64
R3	117	-10	-13	6	11.3	5.9	135*
R4	64	-22	-17	8	4.5	4.4	79
R5	66	-4	-14	5	5.8	4.9	135
R6	121	-12	-10	9	9.2	8.9	135*

2.3.3 Dye sampling methods

Dye concentration D was measured with a flow-through fluorometer mounted on a GPS tracked jet ski [*Clark et al.*, 2009], allowing measurements on cross-shore transects through the surfzone where small boats cannot operate. An onboard position display facilitated repetition of predetermined transects. Water was pumped from an intake 20 cm below the surface into a debubbler, thus reducing the number of large bubbles entering the optical instruments. The water subsequently passed through a turbidity sensor to estimate the remaining bubble interference, and finally through a Rhodamine WT fluorometer. Dye fluorescence measurements are corrected for bubble effects [*Clark et al.*, 2009], with resulting root mean square (rms) errors estimated to be less than 2.7% of D. Mixing within the flow-through system smoothes sharp gradients in dye concentration over time scales less than 2.4 s. The time for water to move through the flow-through system and reach the fluorometer varied by ± 0.84 s, resulting in spatial errors (matching dye measurements to GPS positions) of a few meters, dependent upon jet ski speed [*Clark et al.*, 2009].

Dye tracer plumes were sampled for 40 to 121 minute durations (Table 2.2) downstream from the dye source on cross-shore transects (e.g., R3 and R6 examples in

Figure 2.3). The dye plume was allowed to advect past the farthest downstream transect for roughly 20 minutes prior to sampling, insuring that initial transients had moved beyond the sampling region. Inbound transects were driven from seaward of the dye plume towards the shoreline until the jet ski turned around in roughly 0.5 m water depth (< 10 m from the shoreline). Inbound transects were shore normal, uninterrupted, and driven just in front of a broken bore to reduce the number of bubbles entering the flow-through dye sampling system. Outbound transects were not analyzed because large amounts of air was entrained when the jet ski jumped over bores, and transects were often interrupted while avoiding waves. Inbound sampling over the same part of the wave orbital cycle (e.g., just in front of a bore) may bias the cross-shore dye locations by roughly $\pm 1 - 2$ m (using linear theory for typical HB06 surfzone conditions). The alongshore distances between transects varied between roughly 20 and 250 m, and the largest downstream distance was 686 m.

Each transect location was repeated 1–4 times before moving to the next location, and the entire pattern was repeated several times. Each transect through the dye plume yields a realization (or snapshot, denoted with an i) of cross-shore dye concentration $D_i(x, y_j)$ at alongshore transect location y_j. The number of transect locations for each release ranged from three (R1) to nine (R6). The number of realizations on a transect is N_j, and the release averaged realizations per transect $\langle N_j \rangle^{(j)}$ (where $\langle \cdot \rangle^{(j)}$ is the average over all transect locations j in a release) varies between 4.5 and 15.3 (Table 2.2).

Individual $D_i(x, y_j)$ realizations include instrument dye measurement errors (with uncertainty $\pm 0.027\, D$) and errors from the ± 0.84 s uncertainty in flow-through system delay time τ [*Clark et al.*, 2009]. The delay time error is assumed to have a Gaussian probability density function (PDF) $P(\tau)$ with 0.84 s standard deviation. Total rms dye measurement errors $\epsilon_i(x, y_j)$ are estimated from squared dye variations and squared dye measurement errors integrated over $P(\tau)$

$$\epsilon_i(x, y_j) = \left[\int_{-\infty}^{\infty} [D_i(x - c\tau, y_j) - D_i(x, y_j)]^2 P(\tau) d\tau + \int_{-\infty}^{\infty} [0.027 D_i(x - c\tau, y_j)]^2 P(\tau) d\tau \right]^{1/2}, \tag{2.2}$$

where c is the roughly 1-5 $\mathrm{m\,s^{-1}}$jet ski speed. In general, ϵ_i is $< 20\%$ of D_i.

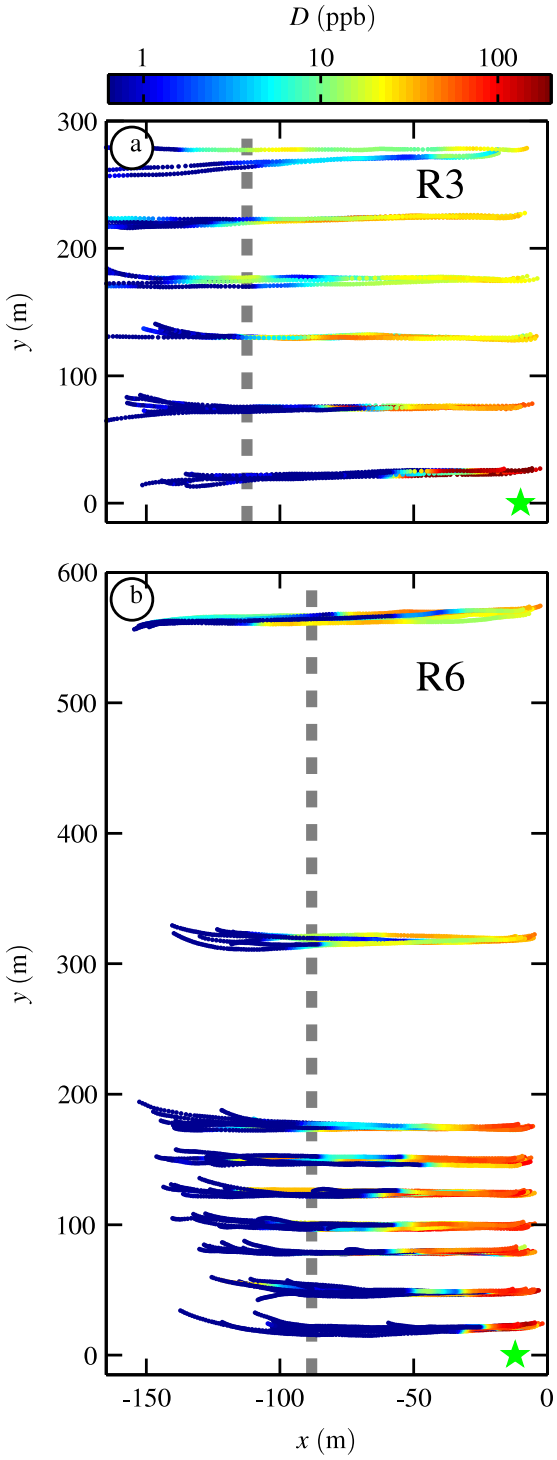

Figure 2.3: Jet ski dye measurements D (concentration in color) during releases (a) R3 and (b) R6 versus cross-shore distance from the shoreline x, and alongshore distance y from the dye source (green star). Only inbound (traveling towards the beach) transects are shown. Dashed gray line indicates the seaward edge of the surfzone.

2.4 Tracer means and moments

2.4.1 Absolute averages

Turbulent tracer dispersion has time varying structure, and ensemble averages (over realizations in time) are used to describe mean (or bulk) tracer statistics [e.g., *Taylor*, 1921; *Batchelor*, 1949; *Csanady*, 1973]. Absolute averages are taken in a fixed coordinate frame, and include the effects of both meandering (varying advection of the realization center of mass) and relative diffusion about the realization center of mass. Relative averages remove meandering by averaging in a center of mass coordinate system (relative to each realization), and isolate the effects of relative diffusion by smaller spatial and temporal scale processes. *Batchelor* [1952], *Csanady* [1973], *Fong and Stacey* [2003] and many others discuss absolute and relative averaging.

For each release, cross-shore profiles of mean (absolute averaged) concentration $\overline{D}(x, y_j)$ at each y_j transect location are constructed by averaging N_j transect realizations $D_i(x, y_j)$ in shoreline coordinates x, i.e.,

$$\overline{D}(x, y_j) = \langle D_i(x, y_j) \rangle^{(i)}, \tag{2.3}$$

where $\langle \cdot \rangle^{(i)}$ is the average over all realizations i. Absolute averaging is used for simplicity because the interaction of a tracer plume with a boundary (i.e., the beach) complicates the interpretation of relative averages. For example, $D_i(x, y_j)$ realizations with shoreline maxima (shoreline attached), equal dye mass, and different cross-shore widths give varying individual centers of mass at a transect location y_j (Figure 2.4). The center of mass variation may imply that the plume is meandering, but could also be explained (e.g., this example) by turbulent fluctuations widening some shoreline attached realizations more than others.

Rms errors $\epsilon_{\overline{D}}(x, y_j)$ in the mean $\overline{D}(x, y_j)$ are estimated by

$$\epsilon_{\overline{D}}(x, y_j) = \frac{1}{\sqrt{\mathcal{N}_j}} \sqrt{\langle \epsilon_i^2(x, y_j) \rangle^{(i)} + \langle [D_i(x, y_j) - \overline{D}(x, y_j)]^2 \rangle^{(i)}}, \tag{2.4}$$

where $\langle \epsilon_i^2(x, y_j) \rangle^{(i)}$ is the mean squared dye measurement error, $\langle [D_i(x, y_j) - \overline{D}(x, y_j)]^2 \rangle^{(i)}$ is the dye variance at each x, and $\mathcal{N}_j$ is the degrees of freedom at a transect

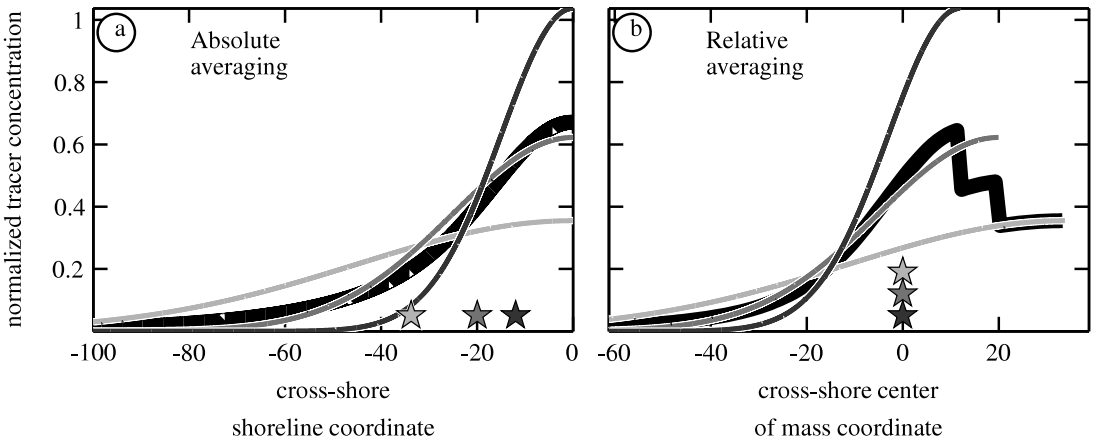

Figure 2.4: Schematic cross-shore tracer concentration in (a) shoreline and (b) center of mass coordinates, illustrating the difficulty in estimating relative diffusivity near the shoreline (shoreline coordinate zero). Tracer averages (thick black curves) are from three realizations (gray curves) with varying cross-shore widths. The center of mass for each realization is indicated with a star in the corresponding shade of gray.

location j (Appendix 2.9). The dye variance is usually much larger than the instrumental error. Using $\mathcal{N}_j$ in (2.4) accounts for consecutive $D_i(x, y_j)$ that are not independent. The $\mathcal{N}_j$ are estimated from the Eulerian tracer decorrelation time (Appendix 2.9), where $\mathcal{N}_j = 1$ and $\mathcal{N}_j = N_j$ correspond to completely dependent and completely independent sampling, respectively (release averaged $\langle \mathcal{N}_j \rangle^{(j)}$ are given in Table 2.2).

2.4.2 Mean profile $\overline{D}(x, y_j)$ cross-shore integrated statistics

Two cross-shore integrated tracer statistics are estimated from mean $\overline{D}(x, y_j)$ profiles; the alongshore tracer transport $M(y_j)$, and the surface-center of mass (first moment) $\mu(y_j)$. These statistics are both functions of y_j, the alongshore distance from the dye source. The jet ski cross-shore transects are driven as shallow as possible without running aground, and the location of the $\overline{D}(x, y_j)$ inner ends vary. To avoid propagating transect end variations into $\overline{D}(x, y_j)$ statistics, the shoreward integral limit is at $x_{\rm in}$ (Table 2.2), the inner $\overline{D}(x, y_j)$ end that is farthest from the shoreline (for each release). Taking the integral limit at $x_{\rm in}$ biases mean transect statistics equally, rather than randomly as with variable inner ends. The $x_{\rm in}$ are generally shoreward of the cross-shore

dye release location x_0, and little data is discarded. The effect of the unsampled region near the shoreline on $M(y_j)$ is discussed in Section 2.7.4.

An idealized tracer plume conserves alongshore tracer transport (i.e., flux through the xz plane). Assuming vertically well-mixed tracer, alongshore uniform depth $h(x)$ and alongshore current $V(x)$, negligible tracer-alongshore current covariance, and negligible dye offshore of frame 7 (x_{F7}), the mean alongshore tracer transport $M(y_j)$ is defined as

$$M(y_j) = \int_{x_{\mathrm{F7}}}^{x_{\mathrm{in}}} h(x)V(x)\,\overline{D}(x, y_j)\,dx. \tag{2.5}$$

The transport M at $y = 0$ is given by the estimated pump flow rate ($\mathrm{m^3\,s^{-1}}$) times the initial dye concentration (2.1×10^8 ppb).

The tracer plume surface-center of mass $\mu(y_j)$ is given by the $\overline{D}(x, y_j)$ first moment

$$\mu(y_j) = \frac{\int_{x_{\mathrm{out}}}^{x_{\mathrm{in}}} x\,\overline{D}(x, y_j)\,dx}{\int_{x_{\mathrm{out}}}^{x_{\mathrm{in}}} \overline{D}(x, y_j)\,dx}, \tag{2.6}$$

where the offshore limit of $\overline{D}(x, y_j)$, x_{out}, is always seaward of the tracer plume. For non-shoreline attached tracer plumes (i.e., no plume-shoreline interaction) and no cross-shore advection, $\mu(y_j)$ is expected to remain constant [e.g., *Csanady*, 1973]. In contrast, shoreline attached plumes spread (i.e., disperse) away from the shoreline, and $\mu(y_j)$ magnitudes are expected to increase downstream. Similar to $\mu(y_j)$, the shoreline also complicates estimates of the plume second moment, as discussed in Section 2.6.

Errors $\epsilon_M(y_j)$ and $\epsilon_\mu(y_j)$ in cross-shore tracer statistics $M(y_j)$ and $\mu(y_j)$ are estimated using Monte Carlo simulations. For each transect, 10^4 simulated $\overline{D}(x, y_j)$ are generated from the observed $\overline{D}(x, y_j)$ plus Gaussian noise, where the noise variance is equal to $\epsilon^2_{\overline{D}}(x, y_j)$ (2.4). The tracer statistic errors $\epsilon_M(y_j)$ and $\epsilon_\mu(y_j)$ are estimated as the standard deviation of simulated $M(y_j)$ and $\mu(y_j)$ calculated from the simulated $\overline{D}(x, y_j)$. The errors are dependent on the $\epsilon^2_{\overline{D}}$ decorrelation length-scale, thus the Monte Carlo process is repeated with cross-shore decorrelation length-scales between zero and twice the surfzone width L_x. The maximum $\epsilon_M(y_j)$ and $\epsilon_\mu(y_j)$ over the range of decorrelation length-scales, are used.

2.5 Observations of surfzone tracer plumes

2.5.1 Tracer cross-shore structure

Continuous surfzone dye releases in an alongshore current form tracer plumes (e.g., Figure 2.3) similar to a smokestack plume in the wind, with plume axis parallel to the shoreline. The positive alongshore current (Figure 2.2b) advects dye downstream ($+y$) from the dye source (green star, Figure 2.3). The initially concentrated dye dilutes and spreads cross-shore as it is advected downstream. The plumes were visually patchy with adjacent high and low concentration areas at all alongshore distances from the dye source, and the patch length-scale increased with distance. Bores did not "surf" dye to the shoreline, although the plume cross-shore width visually widened with each passing bore [e.g., *Feddersen*, 2007]. Bore-mixing was most apparent when plume widths were < 10 m, and difficult to observe when plume widths were visually > 40 m.

At all cross-shore locations, individual $D_i(x, y_j)$ vary about the mean (e.g., Figure 2.5). At transect locations close to the source (e.g., Figure 2.5a,d), dye maxima are sometimes seaward of the shoreline, and have "meandering like" variations (roughly ± 10 m). Farther downstream from the dye source (Figure 2.5, all panels except a and d) the $D_i(x, y_j)$ realizations are more shoreline attached, and may significantly interact with the shoreline boundary.

The mean tracer profile errors $\epsilon_{\overline{D}}(x, y_j)$ (2.4), indicated by the light-colored regions about the mean in Figure 2.6, combine variability between realizations (e.g., Figure 2.5) and dye measurement errors (2.2). For all realizations, dye inter-realization variance (last term of (2.4)) dominates $\epsilon_{\overline{D}}(x, y_j)$ and is on average 45 times greater than mean squared dye measurement errors. The $\epsilon_{\overline{D}}(x, y_j)$ increase with increasing $\overline{D}(x, y_j)$ (e.g., Figure 2.6). The R3 $\epsilon_{\overline{D}}(x, y_j)$ are larger than R6 because (in addition to larger $\overline{D}(x, y_j)$) R3 has shorter times between transects, resulting in lower degrees-of-freedom $\mathcal{N}_j$ (Table 2.2).

The mean tracer profiles $\overline{D}(x, y_j)$ (Figure 2.7) average over stirring and meandering, and are smoother than individual profiles $D_i(x, y_j)$ (e.g., Figure 2.5). Most mean profiles $\overline{D}(x, y_j)$ are shoreline attached with maxima at or near the shoreline (Figure 2.7). The exception, R1, has maxima in the mid- to outer-surfzone, likely because

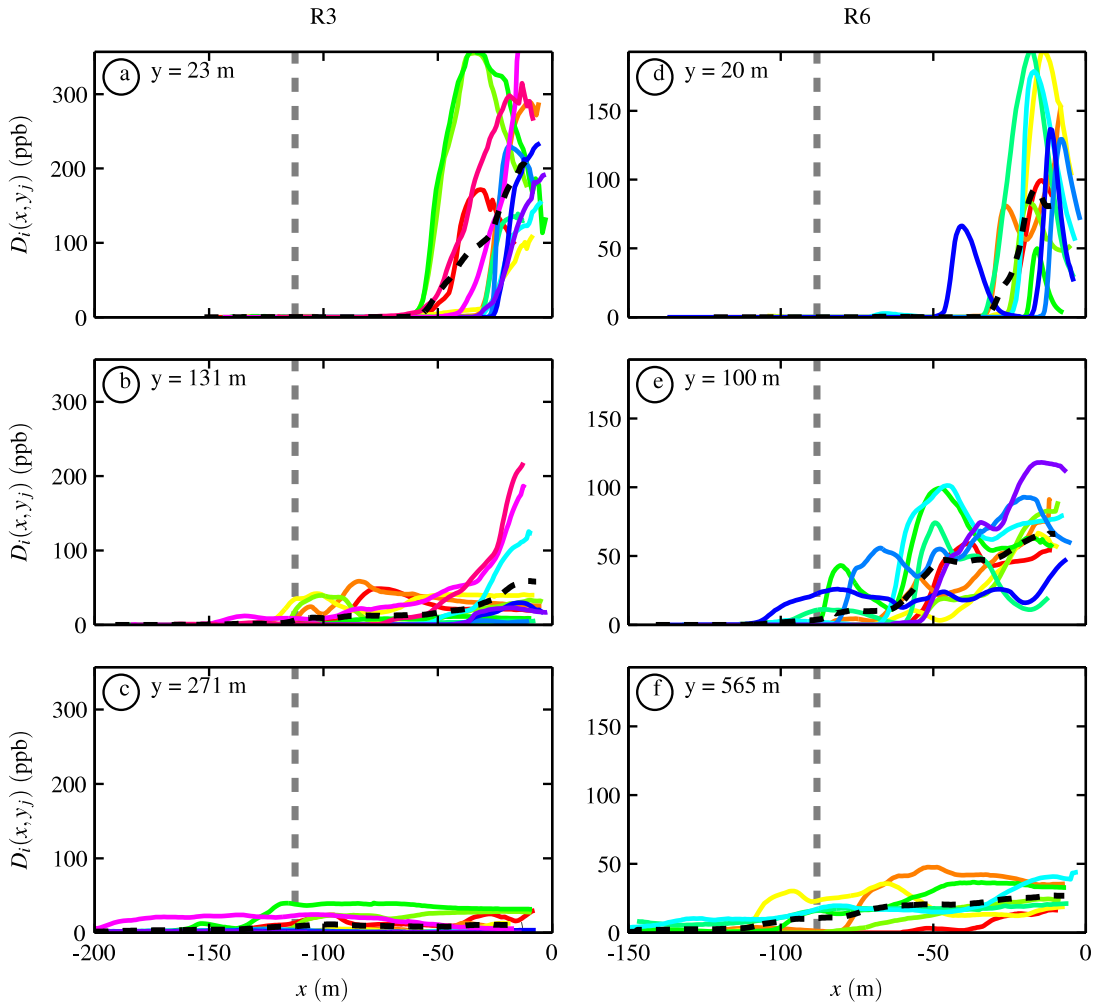

Figure 2.5: Cross-shore dye concentration transects $D_i(x, y_j)$ versus x for (a-c) R3 and (d-f) R6 at three downstream locations y from the dye source (see each panel). In each panel, individual realizations $D_i(x, y_j)$ are in color and the mean $\overline{D}$ is a dashed black curve. (a-c) R3 and (d-f) R6 have different vertical scales.

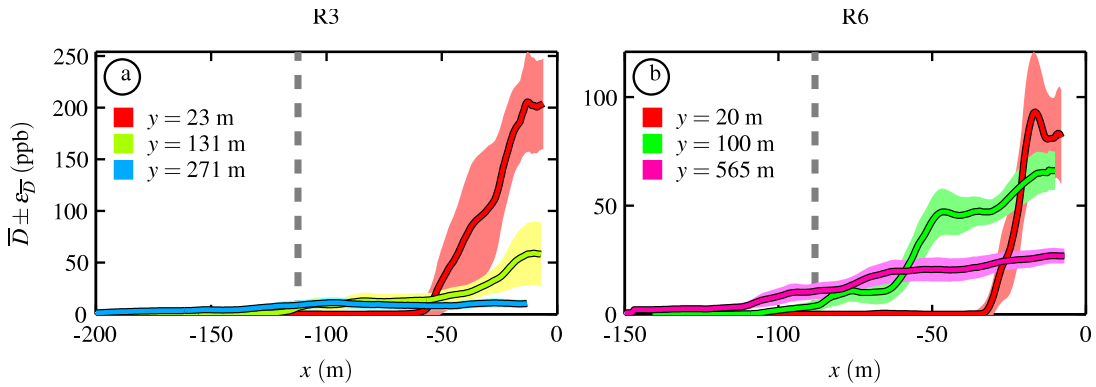

Figure 2.6: Mean dye profile curves $\overline{D}(x, y_j)$ with lighter regions indicating $\overline{D}(x, y_j) \pm \epsilon^2_{\overline{D}}(x, y_j)$, for dye releases (a) R3 and (b) R6 at three alongshore distances y from the dye source (see legend). The dashed gray line indicates the seaward edge of the surfzone. Vertical scales differ.

dye was released in the mid- to outer-surfzone ($x_0 = -55$ m), and y_j sampling distances are short (Figure 2.7a). On all releases except R5, the initially narrow $\overline{D}(x, y_j)$ profiles disperse across the surfzone and peak concentrations decrease with downstream distance from the source (Figure 2.7). Release R5 was sampled far downstream of the the dye source ($y_j > 240$ m) where tracer had already spread (i.e., saturated) across the surfzone (Figure 2.7e), with smaller concentrations seaward of the surfzone. The two farthest downstream $\overline{D}(x, y_j)$ profiles of R3 (Figure 2.7c, with expanded scale in Figure 2.8) and R6 (Figure 2.7f) are also surfzone saturated. The strong gradients in $\overline{D}$ profiles seaward of the saturated surfzone are consistent with decreased diffusivity.

2.5.2 Alongshore evolution of $\overline{D}(x, y_j)$ statistics

The downstream y evolutions of tracer transport $M(y_j)$ (2.5) and surface-center of mass $\mu(y_j)$ (2.6), estimated using $\overline{D}(x, y_j)$ mean profiles, are examined. Tracer seaward of frame 7 ($x < -150$ m from the MSL shoreline) is neglected (2.5) and reduces some $M(y_j)$ at large y. Alongshore variation in $V(x)$ is also neglected, and complete vertical mixing is assumed. Nevertheless, for all releases, the downstream (i.e., not including $y = 0$ m) tracer transports $M(y > 0\ \mathrm{m})$ generally vary by less than a factor of 2 (Figure 2.9), and (except for R4) are either roughly constant downstream (e.g., R1

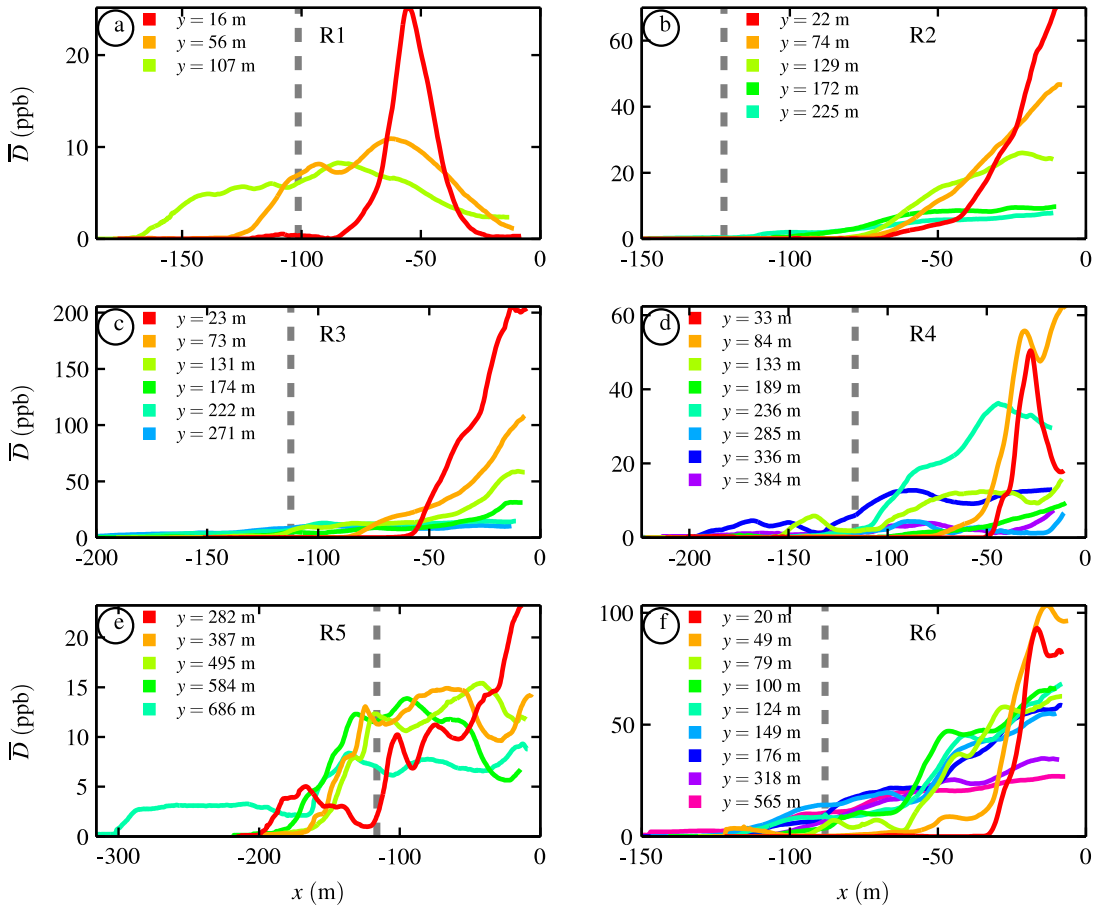

Figure 2.7: Mean tracer concentration $\overline{D}(x, y_j)$ versus x for releases (a) R1, (b) R2, (c) R3, (d) R4, (e) R5, and (f) R6. Colors indicate different downstream alongshore distances y (see legends in each panel). The surfzone is between $x = 0$ m and the vertical dashed gray line. Mean (over all releases) fractional errors $\epsilon_{\overline{D}}(x, y_j)/\overline{D}(x, y_j)$ are 0.38 ± 0.16 (for $D > 5$ ppb), and 0.78 ± 0.29 (for $D < 5$ ppb). Vertical and horizontal scales vary.

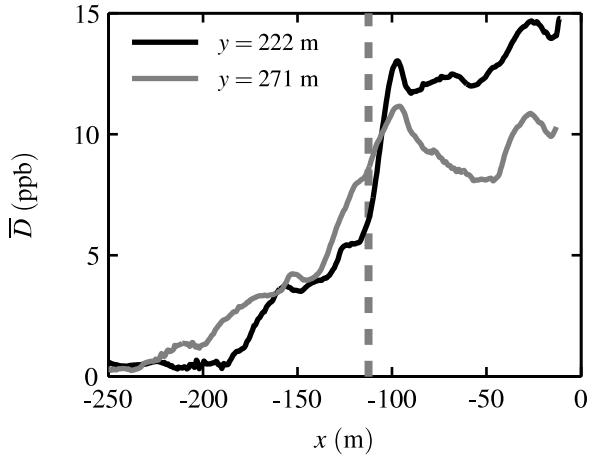

Figure 2.8: $\overline{D}(x, y_j)$ versus x for the two R3 transects farthest downstream from the dye source (expanded view of Figure 2.7c). The surfzone is between $x = 0$ m and the vertical dashed gray line.

and R3) or monotonically decrease (e.g., R2). Thus, a significant amount of the dye measured on the first transect ($y_j > 0$ m) is accounted for farther downstream.

The reason that the pump-rate calculated $M(y = 0\ \mathrm{m})$ are larger than downstream estimated $M(y > 0\ \mathrm{m})$ is not known. Consistent fluorometer calibrations over multiple batches of calibration standards indicate that fluorometer instrumentation error is not the cause. Other possible reasons are discussed in Section 2.7.4. All other tracer moments considered here (e.g., μ (2.6)) are normalized by the cross-shore surface tracer integral on each transect, thus reducing the effect of tracer transport variations.

The $\overline{D}(x, y_j)$ (Figure 2.7) tracer surface-centers of mass $\mu(y_j)$ (2.6) are initially grouped (Figure 2.10) near the cross-shore dye release locations x_0 (Table 2.2). Farther downstream, the shoreline attached R2–R6 $\mu(y_j)$ generally move seaward, consistent with shoreline attached dye profiles (Figure 2.7b-f) broadened by cross-shore dispersion (Figure 2.10, and Section 2.6.3), and does not likely represent cross-shore advection of the mean plume. In contrast, R1 tracer was released mid-surfzone (Table 2.2) and the $\mu(y_j)$ appear (Figure 2.7a) to move seaward by advection of the mean plume, and not plume widening near a boundary. For shoreline attached profiles, surfzone saturation and a lower diffusivity seaward of the surfzone would result in decreased seaward $\mu(y_j)$

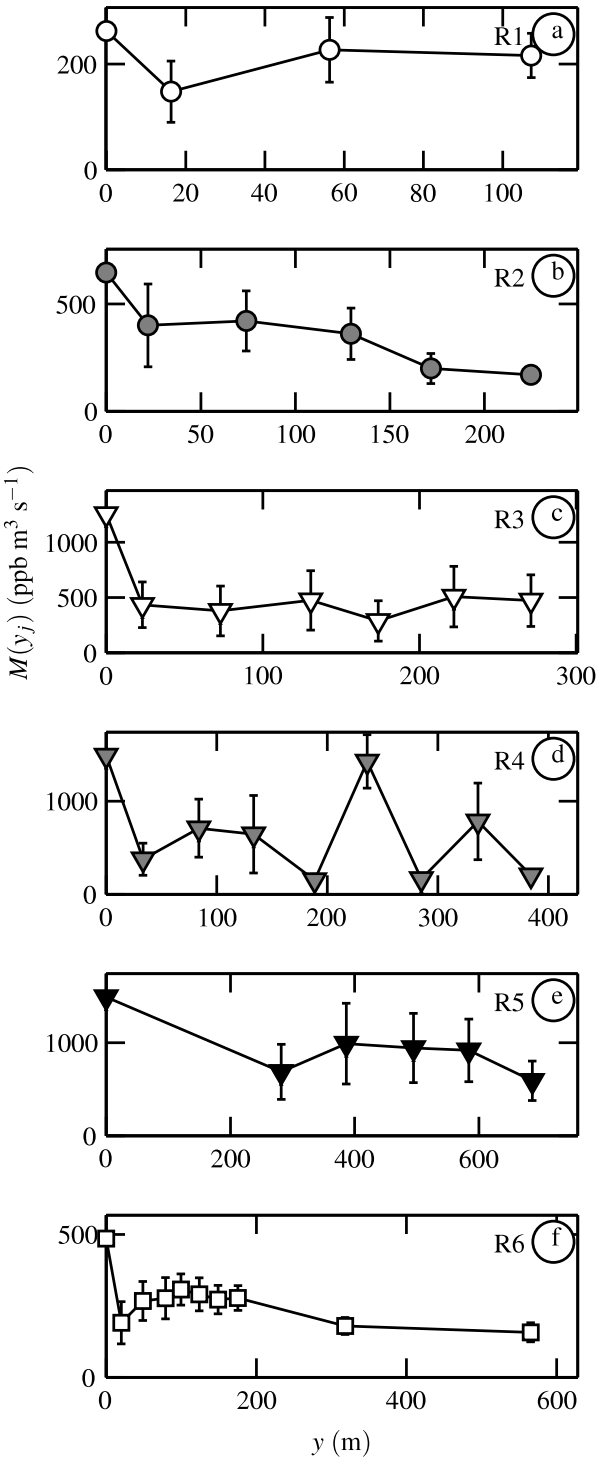

Figure 2.9: Tracer alongshore transport $M(y_j)$ (2.5) versus y, with error bars $\pm\epsilon_M$ for releases (a) R1, (b) R2, (c) R3, (d) R4, (e) R5, and (f) R6. The initial condition at $y = 0$ m is the injected dye transport (concentration times flow-rate).

movement at large y, and is apparent in release R6.

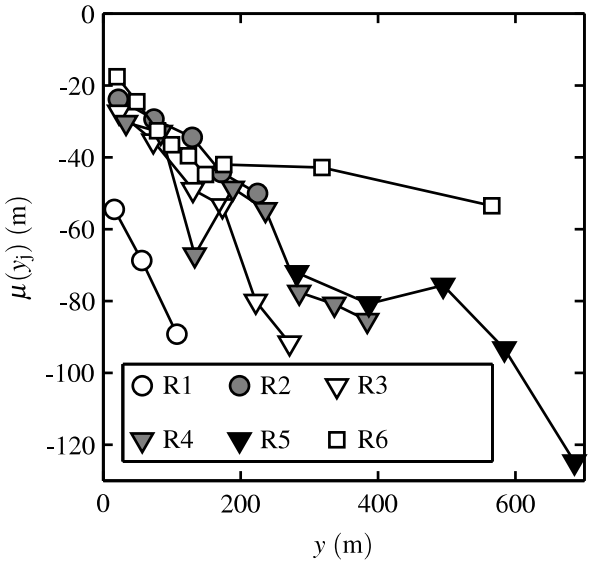

Figure 2.10: Tracer surface-center of mass $\mu(y_j)$ (2.6) versus y. The mean $\mu(y_j)$ error over all transects and releases is $\epsilon_\mu(y_j) \approx 14$ m.

2.6 Dispersive plume widening and surfzone cross-shore diffusivity κ_{xx}

2.6.1 Simple diffusion models

Surfzone cross-shore turbulent mixing results from many mechanisms with different time- and length-scales. The appropriate model diffusivity depends on the model dynamics and the scales resolved. For example, a two-dimensional (2D) horizontal eddy-resolving Boussinesq model [e.g., *Johnson and Pattiaratchi*, 2006; *Spydell and Feddersen*, 2009] would require a much smaller diffusivity than a simple bulk model averaged over longer time scales that combine eddy stirring into a bulk (Fickian) diffusivity. Here, a simple Fickian diffusion model is presented that provides an analytic method for estimating the bulk diffusivity from observations of $\overline{D}(x, y_j)$, and also has solutions relating diffusivity, tracer surface-center of mass, and dilution of maximum tracer concentration.

The time invariant 2-D Fickian advection-diffusion model for vertically-mixed mean tracer concentrations $\overline{D}(x,y)$ with a tracer source Q_0 ($\mathrm{m^3\,ppb\,s^{-1}}$) at $x = x_0$ and $y = 0$, and assuming a constant cross-shore diffusivity κ_{xx} (Brownian diffusion regime), a long narrow plume ($\partial^2/\partial y^2 << \partial^2/\partial x^2$), and cross-shore variable depth $h(x)$ is

$$h(x)V(x)\frac{\partial \overline{D}(x,y)}{\partial y} = \kappa_{xx}\frac{\partial}{\partial x}\left(h(x)\frac{\partial \overline{D}(x,y)}{\partial x}\right) + Q_0\delta(x-x_0,y). \qquad (2.7)$$

Assuming constant surfzone averaged depth $\overline{h}$ (neglecting dh/dx) and that tracer is advected downstream by the surfzone averaged mean alongshore current $\overline{V}$, (2.7) becomes

$$\overline{V}\frac{\partial \overline{D}(x,y)}{\partial y} = \kappa_{xx}\frac{\partial^2 \overline{D}(x,y)}{\partial x^2} + \frac{Q_0}{\overline{h}}\delta(x-x_0,y), \qquad (2.8)$$

and allows for analytic solutions. For HB06 cross-shore variable bathymetry $h(x)$ (Figure 2.1b), observed $V(x)$ (Figure 2.2b), and dye release locations (Table 2.2), numerical solutions to the constant (2.8) and cross-shore varying depth and alongshore current (2.7) equations are similar (particularly for $y > 50$ m), as is the evolution of cross-shore integrated moments. One reason for the similar solutions may be the relatively flat terraced surfzone bathymetry (see $-75 < X < -10$ m in Figure 2.1b). Defining a plume alongshore advection time t_p

$$t_\mathrm{p} = \overline{V}^{-1}y,$$

where t_p is the time for a section of the plume moving with $\overline{V}$ to reach a downstream location y, (2.8) reduces to the familiar 1-D diffusion equation

$$\frac{\partial \overline{D}(x,t_\mathrm{p})}{\partial t_\mathrm{p}} = \kappa_{xx}\frac{\partial^2 \overline{D}(x,t_\mathrm{p})}{\partial x^2} + \hat{Q}_0\delta(x-x_0,t_\mathrm{p}), \qquad (2.9)$$

where $\hat{Q}_0 = Q_0/(\overline{h}\,\overline{V})$. On an unbounded domain (2.9) has a Gaussian solution,

$$\overline{D}(x,t_\mathrm{p}) = \frac{\hat{Q}_0}{\sqrt{4\pi\kappa_{xx}t_\mathrm{p}}}\exp\left[\frac{-(x-x_0)^2}{4\kappa_{xx}t_\mathrm{p}}\right], \qquad (2.10)$$

where κ_{xx} is related to the tracer second moment σ^2 [e.g., *Csanady*, 1973]

$$\kappa_{xx} = \frac{1}{2}\frac{\mathrm{d}\sigma^2}{\mathrm{d}t_\mathrm{p}}, \tag{2.11}$$

and σ^2 is defined as

$$\sigma^2 = \frac{\int_{-\infty}^{\infty}[x-\mu]^2\overline{D}(x,y_j)\,dx}{\int_{-\infty}^{\infty}\overline{D}(x,y_j)\,dx}, \tag{2.12}$$

where μ (2.6) is calculated over the $\pm\infty$ domain. On a semi-infinite domain ($-\infty < x < 0$) with a no-flux boundary condition at the $x = 0$ shoreline

$$\left.\frac{\partial\overline{D}}{\partial x}\right|_{x=0} = 0,$$

(2.9) has the method of images solution

$$\overline{D}(x,t_\mathrm{p}) = \frac{\hat{Q}_0}{\sqrt{4\pi\kappa_{xx}t_\mathrm{p}}}\left[\exp\left(\frac{-(x-x_0)^2}{4\kappa_{xx}t_\mathrm{p}}\right) + \exp\left(\frac{-(x+x_0)^2}{4\kappa_{xx}t_\mathrm{p}}\right)\right]. \tag{2.13}$$

For the case of dye released at the shoreline ($x_0 = 0$), the solution (2.13) is a shoreline attached half-Gaussian. The cross-shore diffusivity for (2.13) is

$$\kappa_{xx} = \frac{1}{2}\frac{\mathrm{d}\sigma_\mathrm{sl}^2}{\mathrm{d}t_\mathrm{p}}, \tag{2.14}$$

where σ_sl^2 is the shoreline based second moment

$$\sigma_\mathrm{sl}^2 = \frac{\int_{-\infty}^{0} x^2\,\overline{D}\,dx}{\int_{-\infty}^{0}\overline{D}\,dx}. \tag{2.15}$$

Thus, for shoreline attached plumes (R2, R3, R4, and R6) κ_{xx} is estimated from (2.14) and (2.15), with modification (Section 2.6.2). For plumes that are well separated from the shoreline (i.e., R1), κ_{xx} is estimated from (2.11) and (2.12). Applying (2.14) and (2.15) to numerical solutions of the full advection diffusion equation (2.7) with observed release parameters (Table 2.2), and cross-shore varying $h(x)$ (Figure 2.1) and $V(x)$ (Figure 2.2b), yields κ_{xx} estimates within 10% of the modeled value. Therefore, the cross-shore uniform h and $\overline{V}$ approximations are not expected to bias κ_{xx} significantly.

2.6.2 Estimating surfzone κ_{xx}

Surfzone absolute κ_{xx} are estimated by applying (2.14) and (2.15) to shoreline attached mean tracer profiles $\overline{D}(x, y_j)$, with some adjustments to capture surfzone specific κ_{xx}. Because $\sigma^2_{\rm sl}$ is sensitive to tracer seaward of the surfzone, a surfzone-specific 2nd moment $\sigma^2_{\rm surf}$ is defined, similar to $\sigma^2_{\rm sl}$, but integrated only over the surfzone, i.e.,

$$\sigma^2_{\rm surf}(y_j) = \frac{\int_{-L_x}^{x_{\rm in}} \overline{D}(x, y_j)\, x^2\, dx}{\int_{-L_x}^{x_{\rm in}} \overline{D}(x, y_j)\, dx}, \tag{2.16}$$

thus excluding dye seaward of the surfzone. With a delta function source at $x = x_0$ (Table 2.2) and $y = 0$ (i.e., $t_{\rm p} = 0$), $\sigma^2_{\rm surf}(0) = x_0^2$.

With a reduced κ_{xx} seaward of the surfzone [e.g., *Harris et al.*, 1963], initially rapid surfzone cross-shore dispersion would slow as a tracer spreads offshore. A surfzone saturation ratio $\mathcal{R}$ is used to select transects with dye well contained in the surfzone, and exclude surfzone saturated transects effected by reduced seaward κ_{xx}. For each transect, $\mathcal{R}$ is the ratio of the measured $\sigma^2_{\rm surf}(y_j)$ to that of a saturated surfzone (i.e., constant surfzone concentration)

$$\mathcal{R} = \sigma^2_{\rm surf}(y_j) \Big/ \left[\frac{\int_{-L_x}^{x_{\rm in}} x^2\, dx}{\int_{-L_x}^{x_{\rm in}} dx}\right]. \tag{2.17}$$

Unsaturated transects, between the source and the farthest downstream transect satisfying a surfzone saturation ratio criterion $\mathcal{R} < \mathcal{R}_0$, are included in κ_{xx} estimates. The cutoff threshold $\mathcal{R}_0 = 0.55$ is chosen to include many $\sigma^2_{\rm surf}(y_j)$ in κ_{xx} fits while not biasing κ_{xx} estimates by more than 10% (Appendix 2.10).

For shoreline attached releases (R2, R3, R4, R6), surfzone κ_{xx} is estimated from least squares $\sigma^2_{\rm surf}$ versus $t_{\rm p}$ fits, i.e.,

$$\sigma^2_{\rm surf} = 2\kappa_{xx} t_{\rm p} + \beta, \tag{2.18}$$

where κ_{xx} and β are fit constants, and from (2.15) β is expected to be close to the initial condition x_0^2. The κ_{xx} error ϵ_κ is estimated from the fit slope error assuming the variance of the residuals is equal to $\epsilon^2_{\sigma^2_{\rm surf}}$ [e.g., *Wunsch*, 1996], where $\epsilon_{\sigma^2_{\rm surf}}$ is estimated with the same Monte Carlo methods as ϵ_M and ϵ_μ (Section 2.4.2). All transects between the release location and the farthest downstream transect with $\mathcal{R} \leq \mathcal{R}_0 = 0.55$ are

Table 2.3: Estimated κ_{xx} from a non-shoreline attached σ^2 versus t_p fit (R1), and shoreline attached σ^2_surf versus t_p fits (R2, R3, R4, R6). Squared correlations r^2 are given for all releases, with an exception for R1 where a two point fit gives the trivial result $r^2 = 1$.

	$2[\kappa_{xx} \pm \epsilon_\kappa]t_\mathrm{p} + \beta$	r^2
R1	$2[0.8 \pm 0.31]t_\mathrm{p} + 0$	—
R2	$2[1.3 \pm 0.26]t_\mathrm{p} + 251$	0.94
R3	$2[1.6 \pm 0.68]t_\mathrm{p} + 233$	0.95
R4	$2[2.5 \pm 0.62]t_\mathrm{p} + 545$	0.56
R6	$2[0.5 \pm 0.08]t_\mathrm{p} + 51$	0.97

included in the fit (solid black symbols, Figure 2.11b,c,d,f). For shoreline attached releases, estimated $\kappa_{xx} \pm \epsilon_\kappa$ range from 0.5 ± 0.08 to $2.5 \pm 0.62\ \mathrm{m^2\,s^{-1}}$ with generally high squared correlation coefficients r^2 (Table 2.3). The R5 κ_{xx} is not estimated because all downstream transects are surfzone saturated, with $\mathcal{R} > 0.55$ (Figure 2.11e).

For release R1 with mid-surfzone release location, mean tracer profiles $\overline{D}(x, y_j)$ (Figure 2.7a) are not shoreline attached, thus (2.14) through (2.17) do not apply. The non-shoreline attached R1 surfzone κ_{xx} is estimated using the common definition (2.11) for absolute dispersion without a boundary [e.g., *Fong and Stacey*, 2003; *Jones et al.*, 2008], where the cross-shore moments μ and σ^2 are integrated from x_in to the seaward transect limit x_out. Using the initial condition $\sigma^2 = 0$ (at $t_\mathrm{p} = 0$) and the first downstream σ^2 (surfzone contained by inspection, Figure 2.7), the resulting best-fit is $\kappa_{xx} = 0.8 \pm 0.31\ \mathrm{m^2\,s^{-1}}$, and r^2 cannot be estimated from the two point fit.

2.6.3 Half-Gaussian shoreline-attached model data comparison

For shoreline attached R2, R3, R4, and R6 releases, the observed downstream evolution of $\overline{D}$ is similar to the half-Gaussian solution (2.13) with $x_0 = 0$ m. For example, within the surfzone the observed σ^2_surf increase linearly with t_p (black symbols in Figure 2.11b,c,d,f) with generally high r^2 (Table 2.3) as is expected for (2.13) and (2.14), and is consistent with the assumption (Section 2.6.1) of constant (in time and space) surfzone κ_{xx}. This model also predicts the downstream evolution of the maximum tracer $\overline{D}^{(\mathrm{p})}_\mathrm{max}$

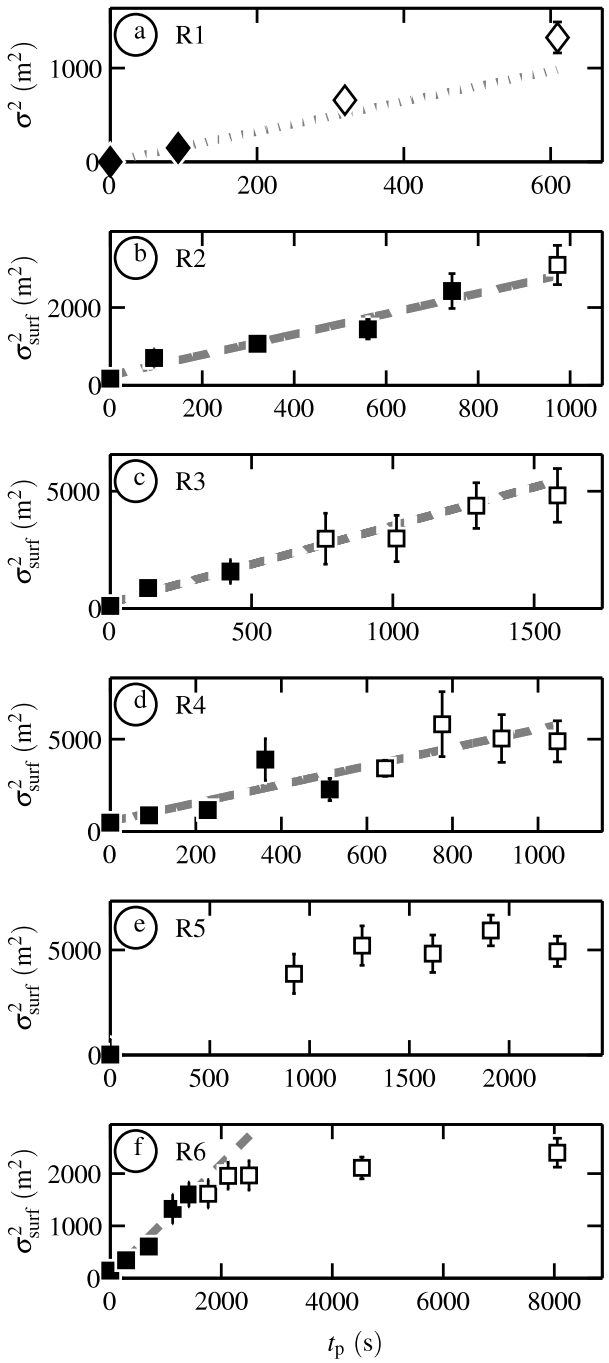

Figure 2.11: (a) $\sigma^2 \pm \epsilon_{\sigma^2}$ and (b-f) $\sigma^2_{\text{surf}} \pm \epsilon_{\sigma^2_{\text{surf}}}$ versus t_{p} for releases (a) R1, (b) R2, (c) R3, (d) R4, (e) R5 and (f) R6. Black symbols indicate points used in the κ_{xx} fits (dashed gray curves) between $t_{\text{p}} = 0$ and the farthest downstream transect with dye largely confined within the surfzone ($\mathcal{R} \leq \mathcal{R}_0$). Errors ϵ_{σ^2} and $\epsilon_{\sigma^2_{\text{surf}}}$ are estimated in the same manner as ϵ_M and ϵ_μ (Section 2.4.2).

$$\overline{D}^{(\mathrm{p})}_{\max} = \frac{2\hat{Q}_0}{(4\pi\kappa_{xx}t_\mathrm{p})^{1/2}}, \tag{2.19}$$

and surface-center of mass $\mu^{(\mathrm{p})}$

$$\mu^{(\mathrm{p})} = \frac{\int_{-\infty}^{0} xG(x_0=0)dx}{\int_{-\infty}^{0} G(x_0=0)dx} = -2(\kappa_{xx}t_\mathrm{p}/\pi)^{1/2} \tag{2.20}$$

where $G(x_0 = 0)$ is the shoreline-attached half-Gaussian solution (2.13) with dye released at $x_0 = 0$. Note that $\mu^{(\mathrm{p})}$ moves offshore owing to the presence of the shoreline, not from advection. Both predictions are now compared with observations using the estimated surfzone κ_{xx}.

For the R2, R3, R4, and R6 transects used in κ_{xx} estimation (solid symbols in Figure 2.11b,c,d,f), and representative of surfzone mixing, the observed $\overline{D}_{\max}$ and predicted $\overline{D}^{(\mathrm{p})}_{\max}$ (2.19) are consistent (Figure 2.12a). The predictions are slightly larger than the observations, and may result from using pump rate estimated $Q_0 = M(y = 0\ \mathrm{m})$ (larger than transect estimates, Figure 2.9) in $\hat{Q}_0$ (2.19) or higher tracer concentrations near the shoreline ($x > x_\mathrm{in}$, Table 2.2) where the jet ski does not sample. Although the R3 and R6 $\overline{D}^{(\mathrm{p})}_{\max}$ have large errors at the first downstream transect, the skill (defined as $1 - \langle(\overline{D}^{(\mathrm{p})}_{\max} - \overline{D}_{\max})^2\rangle / \langle\overline{D}^2_{\max}\rangle$ over all releases) of 0.76 is high. The observed μ and predicted $\mu^{(\mathrm{p})}$ are also consistent (Figure 2.12b) with skill (defined similarly to $\overline{D}_{\max}$ skill) of 0.90. The shoreward bias of $\mu^{(\mathrm{p})}$ relative to μ (Figure 2.12b), may result from assuming a shoreline release ($x_0 = 0$ in (2.20)) in $\mu^{(\mathrm{p})}$. In addition μ estimates may be biased seaward by neglecting the near-shoreline region between x_in (Table 2.2) and the $x = 0$ m shoreline, where the jet ski does not sample. The seaward $\mu(y_j)$ movement for R2–R6 can be explained as dispersive widening of the shoreline attached plume near a boundary (e.g., Figure 2.7b-f). The linear σ^2_surf growth with t_p, the predicted decrease in normalized maxima, and the correspondence of μ and $\mu^{(\mathrm{p})}$, all indicate (2.13) well describes the downstream evolution of surfzone contained tracer released near the shoreline.

The shoreline attached moment $\sigma^2_\mathrm{surf}(y_j)$ (2.16) and the half-Gaussian solution (2.13) assume that the $\overline{D}_{\max}$ cross-shore locations remain at the shoreline, however the observed locations vary slightly (Figure 2.7). Consistent with the assumed shoreline

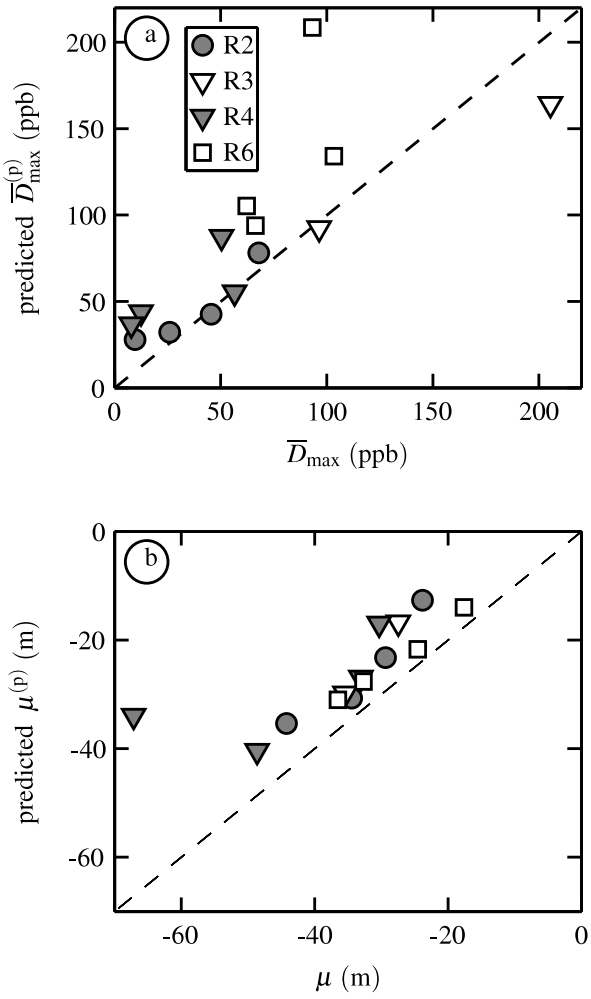

Figure 2.12: (a) Predicted tracer maxima $\overline{D}^{(\mathrm{p})}_{\max}$ versus observed $\overline{D}_{\max}$, and (b) predicted $\mu^{(\mathrm{p})}$ versus observed μ, for surfzone-contained shoreline attached profiles used in κ_{xx} fits (releases R2, R3, R4, and R6). The predicted $\overline{D}^{(\mathrm{p})}_{\max} = 2\hat{Q}_0/(4\pi\kappa_{xx}t_{\mathrm{p}})^{1/2}$ (2.19) and $\mu^{(\mathrm{p})} = -2\sqrt{\kappa_{xx}t_{\mathrm{p}}/\pi}$ (2.20) use the observed best-fit κ_{xx} (Figure 2.11b,c,d,f). The dashed line indicates perfect agreement. The skill in (a) is 0.76 and the skill in (b) is 0.90.

maxima, the "Péclet numbers" ($L\,U/\kappa_{xx}$) for shoreline attached releases are small ($<$ 0.12), where U is the mean cross-shore velocity of the tracer maxima (for profiles used in κ_{xx} fits), $L = U\,t_{\max}$, and $t_{\max}$ is the maximum $t_{\rm p}$ included in κ_{xx} fits. The small "Péclet numbers" and the agreement between μ and $\mu^{(\rm p)}$ are consistent with neglecting cross-shore advection for shoreline attached profiles. In contrast, the "Péclet number" for the non-shoreline attached R1 is 3.9 and the cross-shore advection is accounted for in (2.11) and (2.12).

2.7 Discussion

2.7.1 Surfzone κ_{xx} comparisons

Previous surfzone field experiments have used the alongshore distribution of point-released dye at the shoreline to estimate κ_{yy}, but lack the cross-shore tracer measurements required to estimate κ_{xx} quantitatively. Detailed surfzone tracer κ_{xx} comparisons are therefore not possible, but the κ_{xx} estimated here (Table 2.3) are within the range of previous κ values [*Inman et al.*, 1971; *Clarke et al.*, 2007]. GPS-tracked drifters, designed to duck under breaking waves and avoid surfing onshore, have been used to estimate surfzone cross-shore diffusivities $\kappa_{xx}^{(\rm d)}$ with alongshore uniform [*Spydell et al.*, 2007, 2009] and rip channel [e.g., *Johnson and Pattiaratchi*, 2004; *Brown et al.*, 2009] bathymetries. During the HB06 experiment, drifter-based surfzone $\kappa_{xx}^{(\rm d)}$ were estimated [*Spydell et al.*, 2009], but on different days than dye. Observed dye and asymptotic (long-time) drifter κ_{xx} have similar magnitudes (around $1\ {\rm m}^2\,{\rm s}^{-1}$).

The HB06 drifter-derived $\kappa_{xx}^{(\rm d)}$ were time-dependent. At times less than the drifter Lagrangian time-scale T_{xx} of $O(100\ {\rm s})$, the drifter $\kappa_{xx}^{(\rm d)}$ increase quasi-ballistically ($\sigma^2 \sim t^2$ or $\kappa_{xx} \sim t$) towards a peak value [*Spydell et al.*, 2009]. In contrast, tracer-derived surfzone κ_{xx} are roughly constant in time and $\sigma^2_{\rm surf} \sim t$ (Figure 2.11), indicating Brownian diffusion. However the first dye transects occur near $t_{\rm p} = 100$ s where the drifter ballistic regime generally ends [*Spydell et al.*, 2009], and unobserved ballistic tracer dispersion may have occurred between the first transects and the dye source (where $t_{\rm p} \lesssim T_{xx}$).

For $t > T_{xx}$, drifter $\kappa_{xx}^{(\rm d)}$ gradually decreased [*Spydell et al.*, 2009], possibly

because drifters sampled the lower diffusivity seaward of the surfzone. Recent dye dispersion studies seaward of the surfzone in ~ 10 m water depth [*Fong and Stacey*, 2003; *Jones et al.*, 2008], with similar plume widths to those observed here, found absolute diffusivities roughly 10 times smaller than the surfzone κ_{xx} here. Note that $\sigma^2_{\rm surf}$ is surfzone integrated, and therefore not an appropriate variable to examine seaward κ_{xx}.

2.7.2 Surfzone saturation and diffusion seaward of the surfzone

The $\overline{D}(x, y_j)$ profiles far-downstream (largest y) have roughly constant magnitude (i.e., are saturated) across the surfzone for releases R3, R5, and R6 (Figure 2.7c,e,f), and the far-downstream R3 and R5 transects have sharp $\overline{D}(x, y_j)$ gradients at the seaward edge of the surfzone (e.g., Figure 2.7e and Figure 2.8). These $\overline{D}(x, y_j)$ profiles are consistent with a larger surfzone κ_{xx} smoothing dye gradients inside the surfzone and a smaller κ_{xx} slowly mixing dye farther seaward. In contrast, the two farthest downstream R1 transects have significant amounts of dye outside the surfzone (Figure 2.7a), but the dye plume continues to spread. The continued dispersion seaward of the surfzone may result from absolute averages over meandering of the non-shoreline attached plume, but could also result from rip currents that transport dye well beyond the seaward edge of the surfzone.

Although $\sigma^2_{\rm surf}$ excludes data (and dispersion) seaward of the surfzone, constant $\sigma^2_{\rm surf}$ versus $t_{\rm p}$ does indicate surfzone saturation. The $\sigma^2_{\rm surf}(y_j)$ for R6 initially grow inside the surfzone, but become constant for $t_{\rm p} > 2000$ s in agreement with saturated profiles (Figure 2.7f). In addition, the nearly constant $\sigma^2_{\rm surf}$ in the farthest downstream transects of R4 (Figure 2.11d) suggest surfzone saturation that is not visually apparent in the $\overline{D}(x, y_j)$ profiles (Figure 2.7d).

2.7.3 Parameterizing κ_{xx}

Previous dye dispersion studies [e.g., *Harris et al.*, 1963; *Inman et al.*, 1971] parameterized diffusivity with

$$\kappa_{xx} \sim \frac{H_{\rm b}^2}{T}, \tag{2.21}$$

or

$$\kappa_{xx} \sim \frac{H_{\rm b} L_x}{T}, \tag{2.22}$$

where $H_{\rm b}$ is the wave height at the breakpoint, and T is a wave period. With planar bathymetry and constant $\gamma = H/h$, these two parameterizations (2.21, 2.22) are essentially equivalent. Although previous work found agreement between surfzone diffusivity variability and the parameterizations above [e.g., *Bowen and Inman*, 1974], the physical mechanism driving cross-shore diffusion was unclear.

Mechanisms for cross-shore surfzone diffusion investigated here include bore-mixing, shear dispersion, and horizontal vortical-flow. Multiple cross-shore propagating bores with turbulent front faces (a high diffusivity region) can result in net cross-shore diffusion [*Feddersen*, 2007]. The non-dimensional bore-induced average diffusivity $\bar{\hat{\kappa}}$ [*Feddersen*, 2007; *Henderson*, 2007] is

$$\bar{\hat{\kappa}} = \frac{\sqrt{\pi}}{\hat{c}\hat{T}} \tag{2.23}$$

where $\hat{c}$ and $\hat{T}$ are the non-dimensional phase speed and wave period, respectively. A dimensional mid-surfzone $\bar{\kappa}_{xx}$ can be derived from the scalings in *Feddersen* [2007]

$$\bar{\kappa}_{xx} = O(1)\frac{\sqrt{\pi} h^2}{T}. \tag{2.24}$$

Assuming a self-similar surfzone ($H/h = \gamma$) and a mid-surfzone water depth ($h = h_{\rm b}/2$) then

$$\bar{\kappa}_{xx} = O(1)\frac{\sqrt{\pi}}{4\gamma^2} H_{\rm b}^2 T^{-1}. \tag{2.25}$$

With $\gamma = 0.6$, the slope between κ_{xx} and $H_{\rm b}^2 T^{-1}$ would be near 2.

Here the incident (measured at frame 7, Figure 2.1) $H_{\rm s}$ and mean period $T_{\rm m}$ (Table 2.1) are used in the bore induced κ_{xx} scaling (2.25). Although observed κ_{xx} generally increase with $H_{\rm s}^2\, T_{\rm m}^{-1}$ (Figure 2.13a), the correlation is low ($r^2 = 0.32$), and the best-fit slope of 11.7 is a factor 6 larger than expected for bore-induced dispersion (2.25). The observed cross-shore dye dispersion is probably not dominated by bore-mixing. However, the range of $H_{\rm s}$ and $T_{\rm m}$ are small (Table 2.1) and the κ_{xx} error bars (Figure 2.13a) often overlap, indicating the need for more observations.

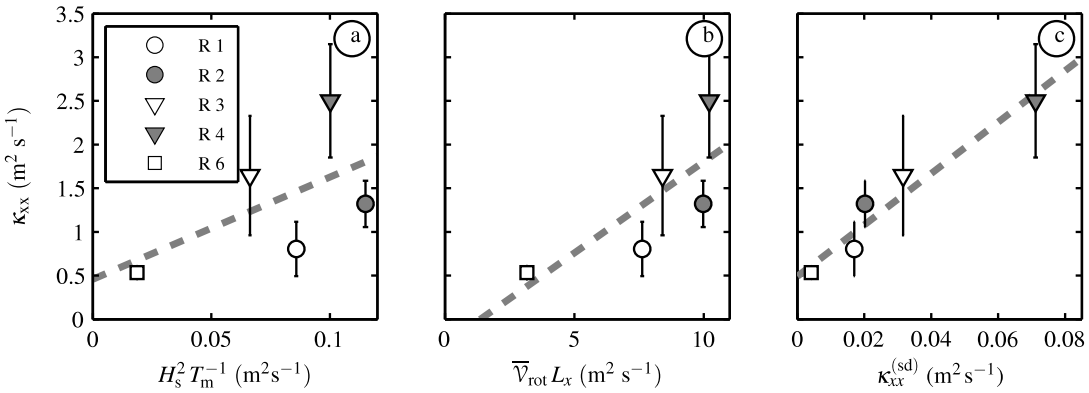

Figure 2.13: Estimated surfzone cross-shore diffusivity $\kappa_{xx} \pm \epsilon_\kappa$ versus (a) $H_s^2\,T_m^{-1}$, (b) $\overline{\mathcal{V}}_{rot}\,L_x$, and (c) $\kappa_{xx}^{(sd)}$. The fit slopes are 11.7 and 0.2, and r^2 correlations are 0.32 and 0.59 for (a) $H_s^2\,T_m^{-1}$ and (b) $\overline{\mathcal{V}}_{rot}\,L_x$, respectively. In (c), the $r^2 = 0.94$ correlation is high, but $\kappa_{xx}^{(sd)}$ magnitudes are much smaller than the observed κ_{xx}.

In model simulations [*Spydell and Feddersen*, 2009], horizontal rotational velocities (i.e., vortical flow) generated by finite crest length breaking [*Peregrine*, 1998] or shear instabilities of the alongshore current [e.g., *Oltman-Shay et al.*, 1989] were found to be a primary mixing mechanism. Here, a mixing-length scaling, i.e., a velocity scale times a length scale [e.g., *Tennekes and Lumley*, 1972], is examined using a surfzone width L_x length-scale and a surfzone-averaged low-frequency horizontal rotational velocity scale $\overline{\mathcal{V}}_{rot}$ (i.e., cross-shore averaged $\mathcal{V}_{rot}(x)$ (2.1) between the shoreline and $x = -L_x$, Table 2.1),

$$\kappa_{xx} = \alpha \overline{\mathcal{V}}_{rot} L_x \tag{2.26}$$

where α is a non-dimensional constant. In analogy with Von Kármán's constant of 0.4 in wall-bounded shear flow, or the factor of 0.57 [e.g., *Rodi*, 1987] in 2-equation (i.e., k-ϵ) models relating diffusivity to a length- and velocity scale product, α is expected to be < 1 but still $O(1)$. Surfzone $\mathcal{V}_{rot}(x)$ includes horizontal rotational flow driven by instabilities in the alongshore current [e.g., *Oltman-Shay et al.*, 1989], wave groups [e.g., *Reniers et al.*, 2004], and finite crest-length wave-breaking [*Peregrine*, 1998; *Spydell and Feddersen*, 2009]. Finite crest length breaking creates vertical vor-

ticity by adjacent regions of breaking and non-breaking wave crest, and differs from mixing by the turbulent front face of a broken bore (e.g., (2.25)). The surfzone averaged $\overline{\mathcal{V}}_{\rm rot}$ ranges between 0.036-0.09 $\mathrm{m\,s^{-1}}$(Table 2.1).

The surfzone tracer κ_{xx} increase with $\overline{\mathcal{V}}_{\rm rot}\,L_x$ (Figure 2.13b) and the linear best-fit gives $r^2 = 0.59$, slope of 0.2, and near-zero y-intercept. The high r^2 and an expected slope < 1 (for a mixing-length scaling) indicate that rotational velocities (surf-zone eddies) play an important role in cross-shore surfzone tracer mixing. However, similar to $H_{\rm s}$ and $T_{\rm m}$, the range of $\overline{\mathcal{V}}_{\rm rot}$ and L_x are relatively small (Table 2.1), and additional observations of surfzone tracer κ_{xx} are required to fully test this parameterization (2.26). A related mixing-length scaling, using $\overline{V}$ instead of $\overline{\mathcal{V}}_{\rm rot}$ as the velocity scale, was correlated with alongshore drifter diffusivity [*Spydell et al.*, 2009], and is consistent with the present result because $\mathcal{V}_{\rm rot}(x)$ and V are correlated [*Noyes et al.*, 2004].

As suggested by *Pearson et al.* [2009], another possible mechanism for cross-shore surfzone tracer mixing is shear dispersion [e.g., *Taylor*, 1954] driven by vertical variation of the cross-shore mean velocity (i.e., undertow). The idealized expression, assuming a step function velocity profile, for the shear dispersion driven $\kappa_{xx}^{\rm (sd)}$ [*Fischer*, 1978] used by *Pearson et al.* [2009]

$$\kappa_{xx}^{\rm (sd)} = \frac{(U_+ - U_-)^2 h^2}{48\kappa_{zz}}, \tag{2.27}$$

where h is the water depth, κ_{zz} is the surfzone vertical diffusivity, U_+ and U_- are the cross-shore velocities in the surface (onshore) and return (offshore) layers with the transition at $h/2$. Other plausible velocity profiles (e.g., linear) have different functional forms for $\kappa_{xx}^{\rm (sd)}$ [*Fischer*, 1978], but give similar results when the on-offshore transports are matched between profiles. Using (2.27) and empirical relationships for κ_{zz} and U_+, and assuming $U_- = -U_+$, *Pearson et al.* [2009] found good agreement between a laboratory estimated κ_{xx} and the corresponding scaled $\kappa_{xx}^{\rm (sd)}$ for shore-normal monochromatic waves.

The cross-shore shear dispersion scaling (2.27) is examined with field data derived from the instrumented frames. During each release, U_- is given by mid-surfzone cross-shore velocities, measured at the instrumented frames (Figure 2.1) roughly 0.4 m above the bed in 1-2 m water depth. The maximum U_- is $-0.07\ \mathrm{m\,s^{-1}}$, and analogous to

Pearson et al. [2009], $U_+ = -U_-$ is assumed. The vertical cross-shore velocity profile is unknown, however the step function profile assumed in (2.27) is used for comparison to previous work [*Pearson et al.*, 2009]. At the same locations the estimated surfzone turbulent dissipation rate $\epsilon \approx 4 \times 10^{-4}\ \mathrm{m^2\,s^{-3}}$ [*Feddersen*, 2010a]. Assuming a turbulent length-scale of half the water depth, the resulting κ_{zz} derived from a k-ϵ closure scheme [e.g., *Rodi*, 1987] are typically $\kappa_{zz} \approx 4 \times 10^{-2}\ \mathrm{m^2\,s^{-1}}$. A linear best-fit of κ_{xx} to $\kappa_{xx}^{(\mathrm{sd})}$ (Figure 2.13c) results in high correlation ($r^2 = 0.94$), but a large slope of 30. The $\kappa_{xx}^{(\mathrm{sd})}$ are expected to be $O(1)$ estimates of cross-shore shear dispersion, but ranged from 35–125 times smaller than the observed κ_{xx} (Figure 2.13c). If vertical tracer gradients exist (Section 2.7.4), the $\kappa_{xx}^{(\mathrm{sd})}$ may be underestimated, however this is unlikely to account for the large differences in magnitude. Although correlations are high, undertow-driven cross-shore shear dispersion is apparently not a dominant tracer dispersal mechanism in the observed natural surfzone. In the laboratory, with monochromatic, shore-normal waves [*Pearson et al.*, 2009], horizontal rotational velocities are reduced or absent and the undertow driven shear dispersion mechanism may be dominant.

2.7.4 Potential causes for reduced downstream $M(y_j)$ relative to dye pump estimates.

Tracer transports at the source $M(y = 0\ \mathrm{m})$, estimated using the dye pump rate, are larger than at downstream transects $M(y > 0\ \mathrm{m})$, estimated with the observed $\overline{D}(y_j)$, $V(x)$, and $h(x)$ (Figure 2.9). The reasons for the initial $M(y_j)$ decrease are unknown, but possible causes, and the implications of those causes on tracer analysis, are explored. One possibility is that pump rates were overestimated by using water (lower viscosity than dye) from a bucket (not the dye tank). However testing on a similar pump system (the original was no longer available) did not support this hypothesis. Pump rate errors would not effect cross-shore moments or κ_{xx}, but would affect the predicted tracer maxima $\overline{D}^{(\mathrm{p})}_{\mathrm{max}}$ (2.19) used for model data comparison (Figure 2.12a).

Increased near-bed dye concentration (where the jet ski does not sample) relative to the surface may be a cause of the reduced downstream $M(y_j)$ relative to the pumped $M(y = 0\ \mathrm{m})$. The injected dye, with concentration 2.1×10^8 ppb, has a specific gravity of 1.2. In a coastal or open-ocean environment, weak vertical mixing requires density

adjustment of the dye to prevent it from sinking towards the bottom [e.g., *Ledwell et al.*, 2004]. In contrast, the surfzone is a region of vigorous vertical mixing, where sand (2.65 specific gravity) is frequently lifted off of the bed and suspended at sediment-water densities $> 1.001\,\rho$ (where ρ is the density of seawater) [e.g., *Beach and Sternberg*, 1996] despite grain settling velocities of roughly 0.03 $\mathrm{m\,s^{-1}}$[e.g., *Hallermeier*, 1981]. Maximum tracer concentrations 1 m from the source are estimated at 10^4 ppb with a density of $1.0001\,\rho$, based upon the conservative assumptions of a constant 0.1 m vertical dye layer (no vertical mixing), advected by $\overline{V} = 0.1\ \mathrm{m\,s^{-1}}$ (Table 2.1) and a small-scale cross-shore diffusivity of 0.01 $\mathrm{m^2\,s^{-1}}$ (from turbulent dissipation, Section 2.7.3). Thus potential tracer induced stratification is considered negligible. With the conservative vertical diffusivity estimate $\kappa_{zz} = 10^{-2}\ \mathrm{m^2\,s^{-1}}$, mid-water column released dye in $h = 2$ m depth has a surface value $> 90\%$ of the mid-depth maximum, for $t_p > 40$ s, and is consistent with the visual observations of rapid vertical mixing. Thus, dye tracer is expected to be vertically well mixed at downstream transect locations.

The region between x_{in} (Table 2.2) and the $x = 0$ shoreline (≈ 10 m wide) was not sampled by the jet ski or included in $M(y_j)$, and the excluded near-shoreline tracer transport is a potential cause of the low biased $M(y > 0\ \mathrm{m})$ relative to the pump estimated $M(y = 0\ \mathrm{m})$. The non-shoreline attached R1, with low shoreline dye concentrations, is not expected to have significant near-shoreline transport, and indeed the $M(y_j)$ are roughly conserved from the release point to farther downstream (Figure 2.9a). Near-shoreline tracer transports are unknown, but qualitative estimates (not shown) are made assuming constant $\overline{D}$ and V between x_{in} and the shoreline. For the two R2 transects closest to the release location, the qualitative near-shoreline estimates are consistent with the correction required to match transect $M(y > 0\ \mathrm{m})$ with pump rate $M(y = 0\ \mathrm{m})$. For R3, R4 and R6 transects with $y < 200$ m, the near-shoreline estimates are between 20-33% of the correction required to match $M(y > 0\ \mathrm{m})$ and $M(y = 0\ \mathrm{m})$, and farther downstream the estimates are negligible. Thus, dye flux inshore of x_{in} may be significant at times, but does not fully explain the generally high bias of pump $M(y = 0\ \mathrm{m})$. Using the shoreline bounded analytic solution (2.13), and neglecting the near-shoreline region (i.e., integrating from x_{in} instead of $x = 0$ m), increases κ_{xx} roughly $14 - 20\%$. Thus, the κ_{xx} bias for excluding near shoreline tracer is generally low compared with

other uncertainties (error bars in Figure 2.13).

Other factors also induce $M(y_j)$ errors not accounted for in the estimated $M(y_j)$ uncertainties (error bars in Figure 2.9). The bathymetry and alongshore currents $V(x)$ are assumed perfectly alongshore uniform, and alongshore variations would increase $M(y_j)$ uncertainties. However, it is not clear that these assumptions can induce a bias.

2.8 Summary

The cross-shore surfzone dispersion of a continuously released dye tracer in an alongshore current was observed during six dye releases. Tracer concentrations were measured on repeated cross-shore transects, at various alongshore distances from the dye source, with a unique GPS-tracked jet ski dye sampling platform. Tracer is advected with the mean alongshore current (i.e., downstream) forming plumes that become wider and more diluted with distance downstream. Mean cross-shore profiles $\overline{D}(x, y_j)$ often have concentration maxima at or near the shoreline (shoreline attached) with decreasing concentration offshore, qualitatively consistent with a half-Gaussian shape. At large downstream distances from the source, $\overline{D}(x, y_j)$ is approximately constant across the surfzone with decreasing concentrations farther seaward, consistent with much lower diffusivity seaward of, than within, the surfzone.

Tracer alongshore transport $M(y_j)$ and surface-center of mass $\mu(y_j)$) are estimated from the $\overline{D}(x, y_j)$. The mean alongshore $M(y_j)$ is roughly conserved downstream of the dye source, and is typically a factor of 2 smaller than the injected dye flux. For shoreline attached profiles the $\mu(y_j)$ move offshore with downstream distance. For shoreline attached profiles (R2-R6) the offshore μ movement with increasing y is associated with plume widening and not seaward advection of the mean plume.

Surfzone cross-shore absolute diffusivities ($\kappa_{xx} = 0.5 - 2.5\ \mathrm{m^2\,s^{-1}}$), based upon a simple Fickian diffusion model near a boundary, are estimated from mean $\overline{D}(x, y_j)$ profiles. To estimate surfzone diffusivity, only mean tracer transects where tracer is surfzone-contained are included in κ_{xx} fits. For shoreline attached profiles, the estimated diffusivities, the observed tracer surface-center of mass, and the observed tracer maxima are all consistent with the Fickian modeled half-Gaussian solution.

Three potential mechanisms for cross-shore tracer dispersion in the surfzone are examined by testing cross-shore diffusivity parameterizations. A breaking-wave induced (by the turbulent front face of a bore) κ_{xx} parameterization has low correlation with observed κ_{xx} ($r^2 = 0.32$), and the best-fit slope is larger than expected. Undertow driven shear dispersion estimates have high correlation ($r^2 = 0.94$), but significantly under-predict the observed κ_{xx}, indicating that this mechanism is not a dominant term in cross-shore surfzone tracer dispersion. A mixing-length parameterization based on 2D horizontal rotational velocities (surfzone eddies) with length-scales of the surfzone width or less has good correlation ($r^2 = 0.59$) and a best-fit slope < 1 (as expected). This suggests that the observed tracer dispersion is primarily due to surfzone eddies forced either by shear instabilities (shear waves) or by finite-crest-length wave breaking (vertical vorticity generated by adjacent regions of breaking and non-breaking wave crest).

The reasons for the decreased alongshore tracer transport $M(y_j)$, relative to pump rate estimates, are unknown and possible causes are examined. Tracer induced stratification is estimated to be negligible, and unlikely to explain the $M(y_j)$ decrease. Tracer transport in the the neglected near-shoreline region (where the jet ski does not sample) is generally not large enough to account for the $M(y_j)$ decrease. Neglecting tracer near the shoreline may bias κ_{xx} estimates up to 20%.

2.9 Chapter 2, Appendix A: Degrees of freedom in estimating $\overline{D}(x, y_j)$

For each release, the degrees of freedom $\mathcal{N}_j$ at each y_j are estimated from the Eulerian decorrelation time τ_{decorr} and the times between transect realizations. Surfzone dye concentration time series (not shown), measured by fluorometers [*Clark et al.*, 2009] mounted on the instrumented frames (Figure 2.1), are used to estimate $\tau_{\text{decorr}} = A(0)^{-1} \int_0^{\tau_{\max}} A(\tau) d\tau$ [e.g., *Emery and Thomson*, 2001], where $A(\tau)$ is the lagged (τ) dye concentration autocorrelation function and $\tau_{\max}$ is the maximum lag (roughly the duration of each dye release). Sequential D_i realizations separated by times greater than τ_{decorr} are assumed independent and add one to $\mathcal{N}_j$. A group of

realizations separated by times less than τ_{decorr} are assumed fractionally independent and add $1 + (\overline{t}_b - \overline{t}_a)\tau_{\text{decorr}}^{-1}$ to $\mathcal{N}_j$, where $\overline{t_a}$ and $\overline{t_b}$ are the mean times of the first and last realizations in the group. The resulting $\mathcal{N}_j$ is between 1 and number of realizations N_j (Table 2.2).

2.10 Chapter 2, Appendix B: Surfzone saturation ratio for estimating κ_{xx}

Estimates of $\sigma^2_{\text{surf}}(y_j)$ are only included in cross-shore surfzone diffusivity κ_{xx} fits (2.14) if the mean tracer is surfzone contained, so that the fit κ_{xx} represents surfzone diffusivity rather than a combination of the surfzone and the region seaward. To quantify which transects are well contained in the surfzone, a surfzone saturation ratio $\mathcal{R}$ (2.17) is defined as the ratio of $\sigma^2_{\text{surf}}(y_j)$, to the σ^2_{surf} value for uniform tracer across the surfzone (i.e., saturated). The threshold $\mathcal{R}_0$ for determining which y_j locations to include in κ_{xx} fits is developed for shoreline attached profiles (the majority of observations) by modeled tracer diffusion.

The surfzone is likely a region of high diffusivity with lower diffusivity seaward. The transition between these two regions is not understood. Thus, two possible extremes for tracer diffusion are considered to determine the $\mathcal{R}$ threshold. The first is constant diffusivity on a semi-infinite domain with a shoreline no-flux boundary. The second is constant diffusivity within the surfzone (width L_x) with zero diffusivity seaward. This is modeled as a closed domain with no-flux boundaries at the shoreline and the seaward surfzone edge. Diffusivity along the seaward edge of the surfzone is somewhere in between these two extremes.

Non-dimensional variables are introduced

$$\tilde{x} = \frac{x}{L_x},$$

$$\tilde{t} = \frac{t\kappa_{xx}}{L_x^2},$$

$$\tilde{\overline{D}} = \frac{\overline{D}}{\int_0^1 \overline{D}\mathrm{d}\tilde{x}},$$

$$\tilde{\sigma}_{\text{surf}} = \frac{\sigma^2_{\text{surf}}}{L_x},$$

$$\tilde{\kappa}_{xx} = \frac{1}{2}\frac{\mathrm{d}\tilde{\sigma}^2_{\text{surf}}}{\mathrm{d}\tilde{t}},$$

and result in the non-dimensional diffusion equation with a delta function source at the shoreline,

$$\frac{\partial\tilde{\overline{D}}}{\partial\tilde{t}} = \tilde{\kappa}_{xx}\frac{\partial^2\tilde{\overline{D}}}{\partial\tilde{x}^2} + \delta(\tilde{x}=0,\tilde{t}=0),$$

solved on the semi-infinite and closed domains described above. $\tilde{\overline{D}}$ profiles (Figure 2.14a) are initially Gaussian until $\tilde{\overline{D}}$ reaches $\tilde{x}=1$ and either moves beyond the surfzone (semi-infinite domain) or interacts with the surfzone boundary (closed domain). The closed domain increases dye concentrations in the outer surfzone (Figure 2.14a), resulting in larger closed domain $\tilde{\sigma}^2_{\text{surf}}$ relative to the semi-infinite domain (Figure 2.14b). The $\tilde{\sigma}^2_{\text{surf}}$ are linear with respect to $\tilde{t}$ for $\tilde{t} < 0.05$, but asymptotically approach the surfzone saturation limit $[\tilde{\sigma}_{\text{surf}}]^2 = 1/3$ for large $\tilde{t}$ (Figure 2.14b). Fitting $\tilde{\kappa}_{xx}$ to $\tilde{\sigma}^2_{\text{surf}}$ for $\tilde{t} < 0.05$, where $\tilde{\sigma}^2_{\text{surf}}$ growth is linear (Figure 2.14b), produces the correct $\tilde{\kappa}_{xx} = 1$ (Figure 2.14c). Including data with $\tilde{t} > 0.05$, where the $\tilde{\sigma}^2_{\text{surf}}$ growth rate decreases, reduces the fit $\tilde{\kappa}_{xx}$ from the true value (Figure 2.14c).

The greatest possible number of field σ^2_{surf} should be used to estimate κ_{xx} without significantly biasing κ_{xx} from the surfzone value. Requiring that the fit $\tilde{\kappa}_{xx} \geq 0.9$ gives the threshold $\mathcal{R}_0 = 0.48$ and $\mathcal{R}_0 = 0.62$ for the semi-infinite and closed domains, respectively (Figure 2.14c), with average $\mathcal{R}_0 = 0.55$. Only transects between the dye source ($y = 0$ m) and the farthest downstream transect where $\mathcal{R} < \mathcal{R}_0$ are included in κ_{xx} fits (black symbols, Figure 2.11b-f).

Chapter 2, in full, is a reprint of the material as it appears in Journal of Geophysical Research - Oceans, 2010, Clark, David B.; Feddersen, Falk; Guza, R.T., Elsevier, 2010. The dissertation author was the primary investigator and author of this paper.

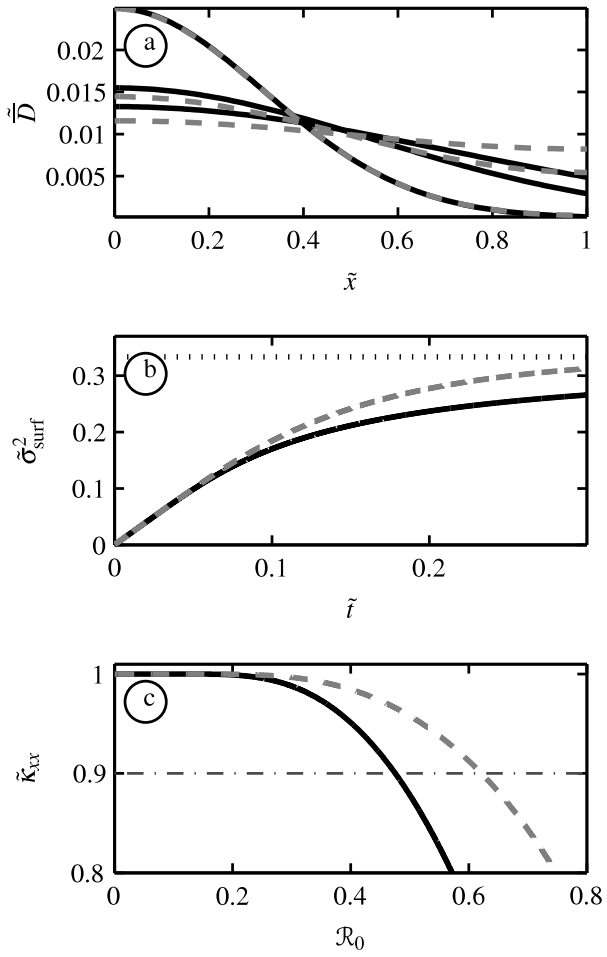

Figure 2.14: (a) Modeled non-dimensional dye concentration $\tilde{\overline{D}}$ versus non-dimensional $\tilde{x}$ at three times ($\tilde{t} = 0.05, 0.15, 0.25$), for (black curves) diffusion on a semi-infinite domain (no-flux boundary at $\tilde{x} = 0$) where the $\tilde{\overline{D}}$ are truncated at $\tilde{x} = 1$, and (dashed grey curves) diffusion on a closed $0 < \tilde{x} < 1$ domain with no-flux boundaries. (b) non-dimensionalized $\tilde{\sigma}^2_{\rm surf}$ versus non-dimensionalized $\tilde{t}$, with saturated $\tilde{\sigma}^2_{\rm surf} = 1/3$ (dotted curve) for reference. (c) non-dimensional fit $\tilde{\kappa}_{xx}$ (using $\tilde{\sigma}^2_{\rm surf}$ with $0 < \mathcal{R} < \mathcal{R}_0$) versus $\mathcal{R}_0$ and, (dot-dashed curve) the $\tilde{\kappa}_{xx} = 0.9$ threshold used to determine the $\mathcal{R}_0$ cutoff.

Chapter 3

Boussinesq Modeling of Surfzone Tracer Plumes: Part 1, Wave and Current Modeling

3.1 Introduction

Estimating the transport and dispersion of tracers (e.g., pollution, fecal indicator bacteria, sediment, or biota) in the surfzone and nearshore region requires a model that accurately simulates the waves and circulation over a broad range of time-scales. For example, on sea-swell time-scales, the strong turbulence due to propagating breaking-waves (bores) has been implicated in the cross-shore dispersion (mixing) of surfzone tracers [e.g., *Inman et al.*, 1971; *Feddersen*, 2007]. Surfzone cross-shore drifter dispersion is governed by lower frequency ($f < 0.02$ Hz) two-dimensional (2D) horizontal vortical motions [*Spydell and Feddersen*, 2009], driven by finite-crest-length wave-breaking [e.g., *Peregrine*, 1998].

Dye tracer, released within the surfzone close to the shoreline, was transported alongshore by the alongshore current V and dispersed cross-shore in a manner resembling a wall-bounded turbulent plume (analogous to a smokestack plume) with axis parallel to the shoreline [*Clark et al.*, 2010]. The cross-shore tracer dispersion was Brownian and the inferred cross-shore diffusivities κ_{xx} were consistent with a mixing-length

parameterization with length-scale given by the surfzone width L_x and velocity scale given by the low-frequency horizontal rotational velocities (vortical motions) [*Clark et al.*, 2010]. Modeling the transport and dispersion of surfzone tracers requires a model that accurately simulates waves and time-dependent circulation (eddies and the mean flow).

Wave-resolving time-dependent Boussinesq models, used to study surfzone waves and circulation, resolve all time-scales from the sea-swell band to mean circulation. Time-dependent Boussinesq models are basically nonlinear shallow water equation models that include extensions for higher-order (weak) dispersion and nonlinearity [e.g., *Peregrine*, 1967; *Nwogu*, 1993; *Wei et al.*, 1995, and many others] so that individual waves can be resolved. Wave-breaking is typically parameterized with a momentum-conserving eddy viscosity approach [*Kennedy et al.*, 2000]. Time-dependent Boussinesq models have been used to study alongshore currents [*Chen et al.*, 2003], time-dependent rip currents [*Johnson and Pattiaratchi*, 2006], and Lagrangian drifter dispersion [*Spydell and Feddersen*, 2009] in natural surfzones.

In Boussinesq surfzone models, the breaking-wave induced vorticity is generated at all length-scales from the large group length-scales to the much smaller length-scales of a breaking-wave crest. The drawback to Boussinesq models is the lack of vertical structure in the currents. Although, unlikely to be important in the surfzone due to intense vertical mixing [e.g., *Feddersen and Trowbridge*, 2005; *Feddersen*, 2010b], vertical-structure may be important just seaward of the surfzone.

Although time-dependent Boussinesq models have been tested with waves in laboratory flumes [e.g., *Kennedy et al.*, 2000], comparisons with field observations have been limited to a few cases. A time-dependent Boussinesq model accurately simulated the cross-shore distribution of significant wave height $H_{\rm s}$ and mean alongshore currents V for a single DELILAH field experiment case example [*Chen et al.*, 2003]. A time-dependent Boussinesq model (`funwaveC`) reproduced the observed cross-shore variation of significant wave height $H_{\rm s}$ and the near-zero currents for a case with small normally-incident waves [*Spydell and Feddersen*, 2009]. The Boussinesq model also reproduced the observed absolute and relative surfzone drifter dispersion statistics [*Spydell and Feddersen*, 2009] which were caused by low frequency ($f < 0.02$ Hz) rotational

(vortical) motions generated by alongshore variations in wave-breaking [e.g., *Peregrine*, 1998].

Here, the time-dependent Boussinesq model `funwaveC` is compared to field observations from a cross-shore array of pressure sensors and current meters spanning the surfzone during the HB06 experiment (Section 3.2). The five cases selected for model-data comparison correspond to dye-tracer release experiments previously analyzed for cross-shore tracer dispersion [*Clark et al.*, 2010]. The time-dependent Boussinesq model (described in Section 3.3) is compared to Eulerian observations of significant wave height, alongshore current, and low-frequency rotational velocities, which are likely important to surfzone tracer transport and dispersion. In particular, bulk (frequency-integrated) quantities (i.e., H_s or V) are well modeled (Section 3.4). Low frequency eddies are also reasonably well reproduced in the model (Section 3.5). The good model-data agreement suggests that simulations of surfzone tracer evolution with this model are appropriate. The results are summarized in Section 3.6. In Chapter 4, a tracer model coupled with the Boussinesq model is compared to observations of dye dispersion.

3.2 HB06 Wave and Circulation Observations

The observations were acquired between September 14th and October 17th, 2006 near Huntington Beach, California as part of the HB06 experiment [*Spydell et al.*, 2009; *Clark et al.*, 2010]. The fixed cross-shore coordinate X represents the (negative) distance from the mean sea level (MSL) shoreline, and increases negatively farther offshore (Figure 3.1). The time- and alongshore-averaged surveyed bathymetry (Figure 3.1) had a steep foreshore, a terraced mid-section ($-50 < X < 20$ m), and a sloping offshore region $X < -80$ m. Offshore of $X = -80$ m, the bathymetry was alongshore uniform and evolved little in time, while the near-shoreline ($X > -25$ m) bathymetry was more variable. The tidal range is typically less than ± 1 m.

Seven tripod frames (denoted F1–F7 from closest to farthest from the shoreline) with pressure sensors and acoustic Doppler velocimeters (ADVs) were deployed in a 160 m long cross-shore array from near the shoreline to 4 m mean depth (Figure 3.1).

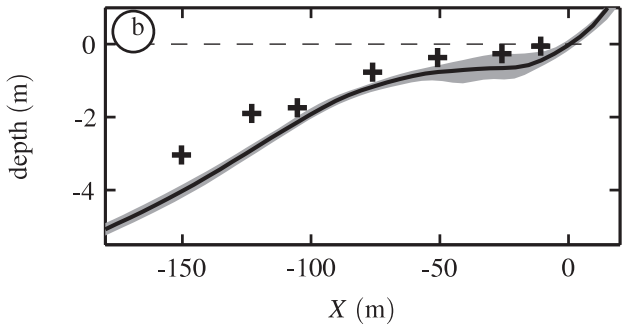

Figure 3.1: Mean (time- and alongshore-averaged) depth derived from HB06 bathymetery surveys versus X, with zero depth at the MSL shoreline (dashed black line). The gray region indicates the bathymetry standard deviation over Y and time. Black crosses indicate approximate instrument frame locations with F1 closest to the shoreline and F7 farthest offshore.

ADV orientation errors were $\pm 3^{\circ}$. Frames are numbered from 1 (shallowest) to 7 (deepest). Frame 7 was always seaward of the surfzone. Frame 1 was 11 m from the MSL shoreline, and the ADV was out of the water during low tides. The instruments at F2 were often non-operational and F2 is not included in the subsequent analysis. Each instrument measured pressure p and cross-shore u and alongshore v velocities.

Five HB06 dye release experiments (denoted R1, R2, R3, R4, and R6) each lasting approximately 2 hours were analyzed by *Clark et al.* [2010]. Dye release details are summarized in Chapter 4. For each dye release experiment, the cross-shore distance from the shoreline x is defined as $x = X - X_{\rm sl}$, where $X_{\rm sl}$ is the shoreline location in fixed coordinates where the depth $h = 0$ m, based on closest in time survey bathymetry and tide level.

For each of the 5 releases, bulk (sea-swell averaged) significant wave heights $H_{\rm s}(x)$ and alongshore currents $V(x)$, and horizontal (low-frequency) rotational velocities $\mathcal{V}_{\rm rot}(x)$ [*Lippmann et al.*, 1999] were estimated at each instrumented frame [see *Clark et al.*, 2010].

3.3 Model Description, Setup, and Simulations

3.3.1 Boussinesq Model Equations

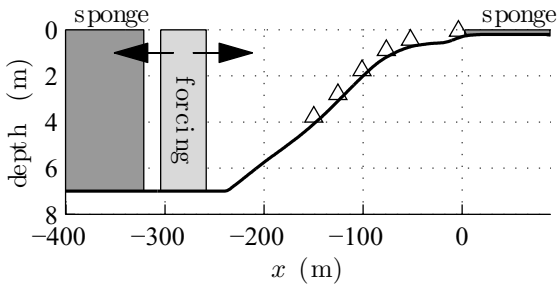

Figure 3.2: Release R1 schematic model bathymetry, sponge layers, and wavemaker regions versus cross-shore coordinate x where $x = 0$ is the nominal R1 shoreline location. Sponge layers (dark shaded regions) are located at the ends of the model domain. The wavemaker region (light shading denoted forcing) radiates waves onshore and offshore (into the sponge layer) as indicated by the arrows. Triangles represent instrument frame locations.

The wave-resolving time-dependent Boussinesq wave model `funwaveC` is used to numerically simulate surfzone waves, currents, and tracer (see Chapter 4) during the five HB06 dye tracer releases. This model has been used to study breaking-wave induced cross-shore tracer dispersion [*Feddersen*, 2007] and surfzone drifter dispersion [*Spydell and Feddersen*, 2009]. The Boussinesq model equations are similar to the nonlinear shallow water equations but include higher order dispersive terms (and in some derivations higher order nonlinear terms). The `funwaveC` model implements the equations of *Nwogu* [1993], and is described in detail in *Spydell and Feddersen* [2009]. The equation for mass (or volume) conservation is

$$\frac{\partial \eta}{\partial t} + \boldsymbol{\nabla} \cdot [(h+\eta)\boldsymbol{u}] + \boldsymbol{\nabla} \cdot \boldsymbol{M}_d = 0, \tag{3.1}$$

where η is the instantaneous free surface elevation, t is time, h is the still water depth, $\boldsymbol{u}$ is the instantaneous horizontal velocity at the reference depth $z_r = -0.531h$, where $z = 0$ is at the still water surface. The two-dimensional horizontal gradient operator $\boldsymbol{\nabla}$ operates on the cross-shore x and alongshore y directions. The dispersive term $\boldsymbol{M}_d$ in

(3.1) is

$$\boldsymbol{M}_d = \left(\frac{z_r^2}{2} - \frac{h^2}{6}\right) h\boldsymbol{\nabla}(\boldsymbol{\nabla}\cdot\boldsymbol{u}) + (z_r + h/2)h\boldsymbol{\nabla}[\boldsymbol{\nabla}\cdot(h\boldsymbol{u})]. \tag{3.2}$$

The momentum equation is (in vector form)

$$\frac{\partial \boldsymbol{u}}{\partial t} + \boldsymbol{u}\cdot\boldsymbol{\nabla}\boldsymbol{u} = -g\boldsymbol{\nabla}\eta + \mathbf{F}_d + \mathbf{F}_{\rm br} - \frac{\boldsymbol{\tau}_b}{(\eta+h)} + \frac{\boldsymbol{\tau}_s}{(\eta+h)} - \nu_{\rm bi}\nabla^4\boldsymbol{u}, \tag{3.3}$$

where g is gravity, $\mathbf{F}_d$ are the higher order dispersive terms, $\mathbf{F}_{\rm br}$ are the breaking terms, $\boldsymbol{\tau}_b$ is the instantaneous bottom stress, $\boldsymbol{\tau}_s$ is the surface stress, and $\nu_{\rm bi}$ is the hyperviscosity for the biharmonic friction ($\nabla^4\boldsymbol{u}$) term. The dispersive terms are [*Nwogu*, 1993]

$$\mathbf{F}_d = -\left[\frac{z_r^2}{2}\boldsymbol{\nabla}(\boldsymbol{\nabla}\cdot\frac{\partial\boldsymbol{u}}{\partial t}) + z_r\boldsymbol{\nabla}(\boldsymbol{\nabla}\cdot(h\frac{\partial\boldsymbol{u}}{\partial t}))\right],$$

and the bottom stress is given by a quadratic drag law

$$\boldsymbol{\tau}_b = c_d|\boldsymbol{u}|\boldsymbol{u},$$

with the non-dimensional drag coefficient $c_d = 2.3\times10^{-3}$ chosen to close a surfzone alongshore momentum balances over a 5 week period at the site [*Feddersen*, 2010b]. This c_d is also consistent and with previous surfzone circulation studies using Boussinesq models [*Chen et al.*, 2003; *Spydell and Feddersen*, 2009]. The surface stress $\boldsymbol{\tau}_s$ allows for forcing from the alongshore wind stress. Only R3 had a significant alongshore windstress of $|\boldsymbol{\tau}_s| = 2\times10^{-5}\ \mathrm{m^2\,s^{-1}}$. Biharmonic friction is required to damp nonlinear aliasing instabilities, and the hyperviscosity is set to $\nu_{\rm bi} = 0.3\,\mathrm{m^4\,s^{-1}}$.

The effect of wave breaking on the momentum equations is parameterized as a Newtonian damping [*Kennedy et al.*, 2000] where

$$\mathbf{F}_{\rm br} = (h+\eta)^{-1}\boldsymbol{\nabla}\cdot\left[\nu_{\rm br}(h+\eta)\boldsymbol{\nabla}\boldsymbol{u}\right].$$

The eddy viscosity $\nu_{\rm br}$ associated with the breaking waves is given by

$$\nu_{\rm br} = B\delta^2(h+\eta)\frac{\partial\eta}{\partial t}, \tag{3.4}$$

where δ is a constant and B is a function of $\partial\eta/\partial t$ and varies between 0 and 1. When $\partial\eta/\partial t$ is sufficiently large (i.e., the front face of a steep breaking wave) B becomes non-zero. The *Zelt* [1991] expression for B is used. A model parameter c_I controls the onset of breaking. When $\partial\eta/\partial t > c_I\sqrt{gh}$, B is non-zero.

The δ and c_I values used are similar to those used for modeling laboratory breaking waves [*Kennedy et al.*, 2000], field wave heights and alongshore currents [*Chen et al.*, 2003; *Lynett*, 2006], rip currents [*Johnson and Pattiaratchi*, 2006], and surfzone drifter dispersion [*Spydell and Feddersen*, 2009].

3.3.2 Model Domain, Discretization, Bathymetry, Sponge Layers, and Boundary Conditions

The model equations are 2nd-order spatially discretized on a C-grid [*Harlow and Welch*, 1965] and time-integrated with a third-order Adams-Bashforth [*Durran*, 1991] scheme. The model cross-shore domain L_x varies between 453 - 490 m, depending on the release day, including onshore and offshore sponge layers (e.g., Figure 3.2). The alongshore model domain is $L_y = 1500$ m, with periodic alongshore boundary conditions. The cross-shore grid spacing is either $\Delta x = 1$ m (R1, R2, R3, and R4) or $\Delta x = 0.75$ m (R6), and alongshore grid spacing is $\Delta y = 1.25$ m. The model time step Δt is set between $0.01 - 0.005$ s, depending upon release.

The model bathymetry is derived from survey bathymetry performed closest in time to the release day (e.g., Figure 3.1) by alongshore averaging the survey bathymetry over the alongshore region (200-600 m, depending upon release) where dye tracer was observed [*Clark et al.*, 2010]. The bathymetry was then adjusted by the mean tidal elevation of observed tracer release. For the onshore sponge layer, a flat region of $h = h_{\min}$ was added to the shoreward end of the bathymetry, where bathymetry $h < h_{\min}$ was set to $h = h_{\min}$. The onshore sponge layer depth $h_{\min}$ varied between 0.2 m and 0.35 m, depending upon release (Table 3.1). This bathymetry was then cross-shore smoothed with a 5-m smoothing width. At offshore locations where the depth $h > 7$ m, the model bathymetry is set to be flat with depth $h = 7$ m to prevent kh (where k is the wavenumber) from becoming too large for the Boussinesq dynamics.

A shoreline sponge layer dissipates any remnant sea-swell or any infragravity wave energy. The sponge layer is applied onshore of the shoreline ($x \geq 0$ m) (Figure 3.2) with a cross-shore width L_{sp} between 60–89 m on flat bathymetry with depth $h_{\min}$. At the offshore end of the model domain, a second 80-m wide sponge layer (Figure 3.2) absorbs outgoing sea-swell wave energy generated at the wavemaker. The flat-

Table 3.1: Model configuration for each HB06 dye release: release number, cross-shore domain width, and shoreline sponge layer width $L_{\rm sp}$ and depth $h_{\rm min}$.

Release	width (m)	$L_{\rm sp}$ (m)	$h_{\rm min}$ (m)
R1	490	89	0.20
R2	454	65	0.28
R3	454	63	0.30
R4	454	60	0.35
R6	453	81	0.20

depth region and sponge layer also prevent infragravity wave refraction. Outgoing infragravity wave energy generated within the model domain is dissipated in the sponge layer.

3.3.3 Generation of Waves

Random directionally-spread waves are generated at a wavemaker (WM), following *Wei et al.* [1999]. The WM oscillates the sea surface η on an offshore source strip located in $h = 7$ m depth (light shaded region in Figure 3.2), with the WM center located about 115 m from the offshore boundary with WM half-width of about 25 m. Thus, the WM region and offshore sponge layer do not overlap. Onshore of the WM, the bathymetry has a 20–27 m wide flat section prior to shoaling into shallower water (Figure 3.2).

At the instrumented frame, the full directional spectrum cannot be estimated, only directional properties (e.g., bulk direction and spread) as a function of frequency [e.g., *Kuik et al.*, 1988]. Therefore, the model wavemaker is initialized with directionally averaged bulk properties. The wavemaker spectra, wave-angle, and directional spread are derived by back-refracting the observed spectral quantities from the most offshore frame 7. The back-refraction assumes linear waves.

The observed spectral frequency resolution was relatively low, with $\Delta f = 1/600\ \mathrm{s}^{-1}$. Therefore, the back-refracted WM wave spectra quantities were back interpolated onto a finer frequency resolution grid with $(\Delta f) = 1/5600\ \mathrm{s}^{-1}$ which resulted in ≈ 750 distinct forcing frequencies (between 0.06–0.18 Hz) depending on the release. The WM recurrence period is 5600 s. The WM is forced following *Wei et al.* [1999]

with the directional distribution used by *Spydell and Feddersen* [2009]. The number of frequencies and directions were sufficient so that the source standing wave problem [*Johnson and Pattiaratchi*, 2006] did not occur.

3.3.4 Model Output

For each release, the model was run for 16,000 s. To facilitate model spinup, the model alongshore velocity $v(x)$ initial condition was set to an interpolation of the observed mean alongshore current $V(x)$. The model η, and u initial conditions were zero. The wavemaker begins generating waves at $t = 0$ s. After 2000 s (≈ 22 min), model variables η, ν_{br}, u, and v are output over the entire model domain every 2 s. Model vorticity $\zeta = \partial v/\partial x - \partial u/\partial y$ is estimated from the output velocity fields. At a single cross-shore transect, η, u, and v are output at 1 Hz to calculate wave spectra.

3.3.5 Model Example

Model sea-surface elevation η and vorticity ζ output for Release R3 are shown in Figure 3.3. Long-period swell approaches the beach with a positive angle of incidence (i.e., $+y$ direction, Figure 3.3a) whereas high frequency ($f \approx 0.16$ Hz) sea is incident from the opposite quadrant. Within the surfzone (dashed line in Figure 3.3a), these finite-crest-length waves break and dissipate generating vorticity with a range of length-scales (Figure 3.3b). Eddies are occasionally ejected seaward from the surfzone.

3.3.6 Model Spinup

To determine the model spin-up time (i.e., model statistics are quasi stationary) the cross-shore integrated (between the shoreline and x_{F7}) and alongshore domain integrated kinetic energy (KE), potential energy (PE), and mean square vorticity (enstrophy, Z) are examined. These quantities are defined as

$$\mathrm{KE} = \int_0^{L_y} \int_0^{x_{\mathrm{F7}}} \frac{1}{2} h(u^2 + v^2) dx dy, \tag{3.5a}$$

$$\mathrm{PE} = \int_0^{L_y} \int_0^{x_{\mathrm{F7}}} \frac{1}{2} g\eta^2 dx dy, \tag{3.5b}$$

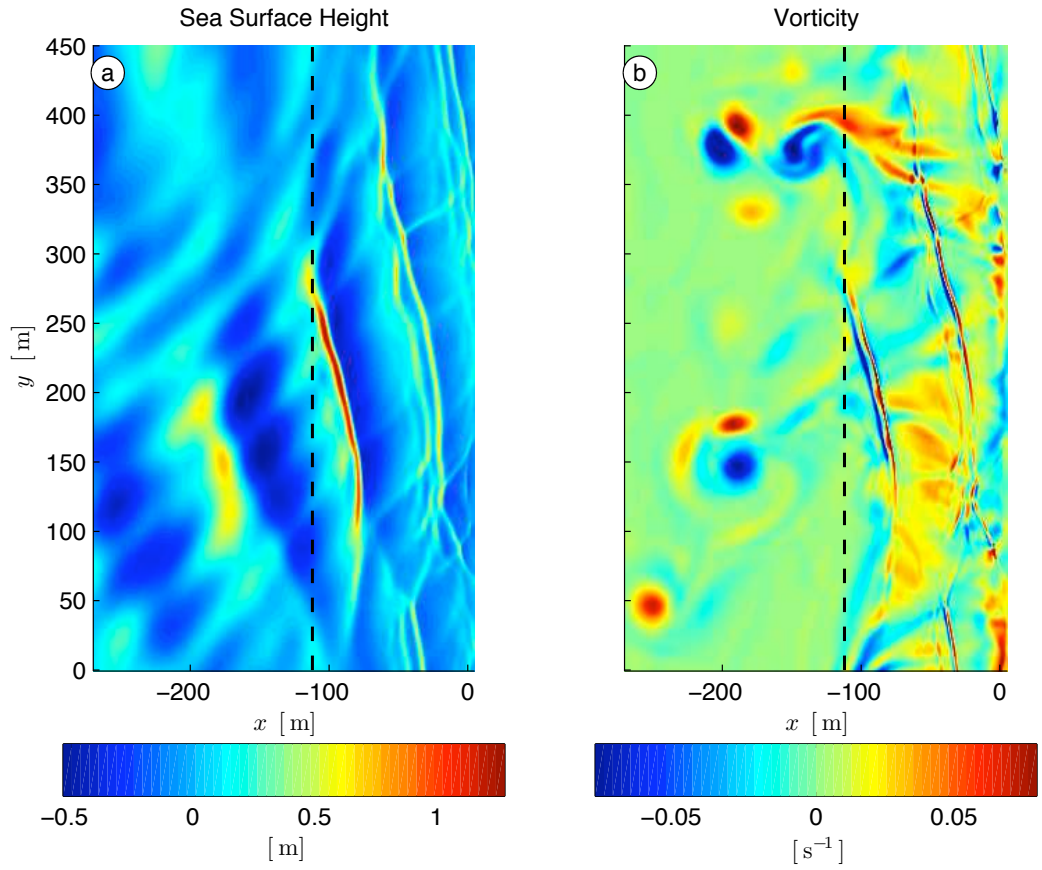

Figure 3.3: Snapshot in time of modeled (a) sea surface elevation η, and (b) vorticity ζ versus x and y for R3, 2700 s into the model run. The model "shoreline" is located at $x = 0$ m and the black dashed line is the approximate outer limit of the surfzone L_x. Only a subset of the model domain is shown. Note the broad range of vorticity length-scales within the surfzone.

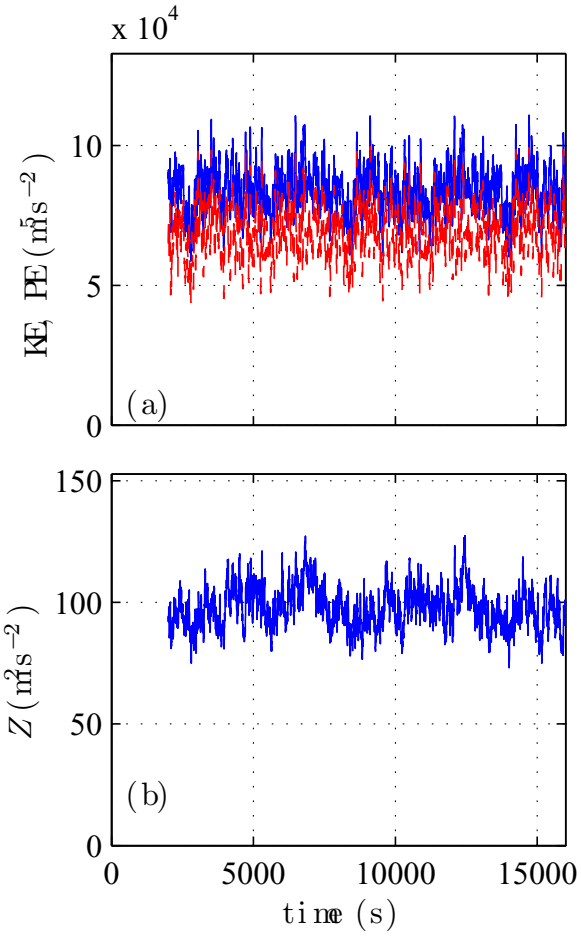

Figure 3.4: Release R2 (a) integrated kinetic KE (blue) and potential PE (red) energy and (b) integrated-square-vorticity Z (3.5c) versus time for R2.

$$Z = \int_0^{L_y} \int_0^{x_{\mathrm{F7}}} \zeta^2 dx dy, \tag{3.5c}$$

where g is gravity. The dominant contribution to PE is from surface gravity waves. KE has contributions from both surface gravity waves and the circulation (mean currents and eddies). The contributions to Z are largely from the mean current and eddy field.

After 2000 s of model spinup, the model KE and PE have equilibrated and fluctuate around a mean for all releases (R2 is shown in Figure 3.4a). For R2 (and also R1, R3, and R4), the PE is generally about 2/3 of the KE. Release R6 had the weakest currents and so $\mathrm{PE} \approx \mathrm{KE}$, as expected for an equipartion of wave energy. After 2000 s, the total enstrophy, Z, also has equilibrated for all releases (Figure 3.4b, other releases are similar), indicating that both the mean alongshore current and the eddy field have also come to largely steady state. The total Z varies typically about $\pm 5\%$ over the simulation with a range of time-scales, but is largely red. The 5600 s wavemaker recurrence is seen in each of the KE, PE, and Z.

3.4 Bulk Parameter: Model-Data Comparisons

Model-data comparison of "bulk" parameters include the sea-swell (0.05-0.25 Hz) frequency-integrated wave statistics such as significant wave height H_{s}, and the mean alongshore current V. Model wave quantities H_{s} are estimated on a single cross-shore transect with 1 Hz η model output using the same methods as used to calculate the field observed quantities. The model mean alongshore current V is estimated as a time-average (from 3000-16,000 s) and alongshore average (over all y) of the instantaneous alongshore velocity v. The alongshore standard deviation (std) of the time-averaged $V^{(\mathrm{m})}(x)$ is also computed, where the superscripts "(m)" and "(obs)" denote model and observed quantities, respectively. Note that model-data comparison of wave-spectra, direction, and spread in the sea-swell band is good at most instrument frame locations (not shown).

Table 3.2: For each release, root-mean-square (rms) error (ϵ) and skill between the model and observed wave height H_s (ϵ_{H_s}) and mean alongshore current V (ϵ_V) over all frames. Skill is defined as (for some quantity T) as skill $= 1 - \langle (T^{(\mathrm{obs})} - T^{(\mathrm{m})})^2 \rangle / \langle (T^{(\mathrm{obs})})^2 \rangle$ where superscript "(m)" and "(obs)" denote model and observed quantities, respectively, and $\langle\rangle$ denotes an average over all frames. This quantity gives the prediction skill over a zero prediction.

Release	ϵ_{H_s} (m)	H_s skill	ϵ_V ($\mathrm{m\,s^{-1}}$)	V skill
R1	0.087	0.98	0.03	0.98
R2	0.065	0.99	0.12	0.77
R3	0.071	0.99	0.05	0.95
R4	0.114	0.98	0.10	0.90
R6	0.044	0.99	0.02	0.95

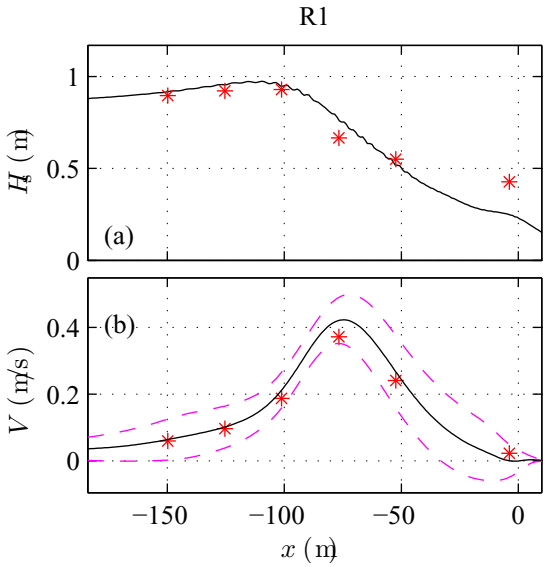

Figure 3.5: Modeled (solid) and observed (symbols) (a) H_s, (b) mean alongshore current V ($\pm$ the alongshore std dev of V, dashed-magenta curves) versus x for R1. The shoreline is located at $x = 0$ m.

3.4.1 Release R1

The R1 observed cross-shore H_s distribution is generally well reproduced by the Boussinesq model (Figure 3.5a). The ϵ_{H_s} are small and the prediction skill is high (Table 3.2). The incident F7 $H_s = 0.9$ m, and wave-breaking begins at F5. The H_s at F1 is underpredicted. At all frames both within and seaward of the surfzone, the observed V is well reproduced by the model (Figure 3.5b, rms error $\epsilon_V = 0.03\ \mathrm{m\,s^{-1}}$, and

high skill of 0.98, Table 3.2). Modeled and observed maximum $V \approx 0.4\ \mathrm{m\,s^{-1}}$occurs near F4. Near the shoreline at F1, both the observed and modeled V are near-zero. The time-averaged model alongshore current $V^{(\mathrm{m})}$ varies weakly in the alongshore by about $\pm 0.05\ \mathrm{m\,s^{-1}}$(magenta dashed-curves in Figure 3.5b) largely due to long-period (> 2000 s) red fluctuations in v. The $V^{(\mathrm{obs})}$ alongshore variability was not measured but is inferred to be small due to the closure of cross-shore integrated alongshore momentum balances during the experiment [*Feddersen*, 2010b].

3.4.2 Release R2

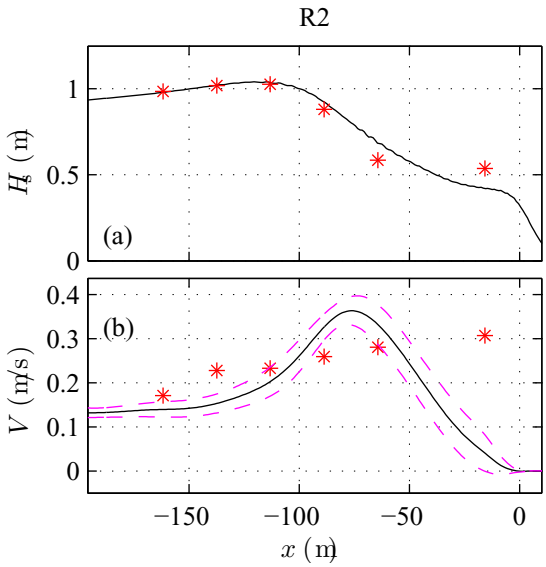

Figure 3.6: Modeled (solid) and observed (symbols) (a) H_s, (b) mean alongshore current V ($\pm$ the alongshore std dev of V, dashed-magenta curves) versus x for R2. The shoreline is located at $x = 0$ m.

Many of the general features of R1 apply to the other releases. Similar to R1, the observed H_s is well modeled (Figure 3.6a) with low rms-error ($\epsilon_{H_\mathrm{s}} = 0.065$ m) and high skill (Table 3.2). The H_s error is largest near the shoreline at F1. The $V^{(\mathrm{obs})}$ increased monotonically towards the shoreline with a maximum of $0.31\ \mathrm{m\,s^{-1}}$at the near-shoreline F1 (asterisks in Figure 3.6b). This strong near-shoreline $V^{(\mathrm{obs})}$ is not predicted (error $= 0.25\ \mathrm{m\,s^{-1}}$), perhaps due to alongshore wave or bathymetric variations not included

in the model. Offshore of the surfzone, a signficant alongshore (northward $+y$ direction) wind stress (included in the model) drives the relatively strong (and well modeled) $V = 0.17\ \mathrm{m\,s^{-1}}$at F7 and F6. Overall, the R2 V model-data agreement is the poorest, with the largest $\epsilon_V = 0.12\ \mathrm{m\,s^{-1}}$and lowest skill (Table 3.2).

3.4.3 Release R3

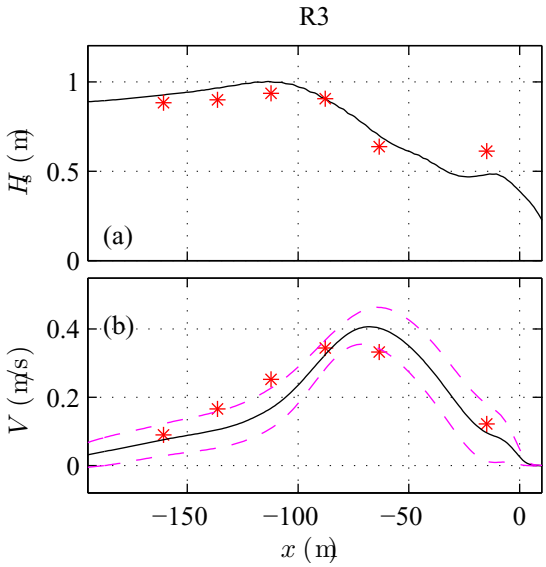

Figure 3.7: Modeled (solid) and observed (symbols) (a) H_s, (b) mean alongshore current V ($\pm$ the alongshore std dev of V, dashed-magenta curves) versus x for R3. The shoreline is located at $x = 0$ m.

Similar to R1 and R2, the R3 model $H_\mathrm{s}^{(\mathrm{m})}$ generally reproduces the observed $H_\mathrm{s}^{(\mathrm{obs})}$ (Figure 3.7a) with $\epsilon_{H_\mathrm{s}} = 0.07$ m and high skill (Table 3.2). Maximum $H_\mathrm{s} = 1$ m occurs near F5 with a sloping decrease down to F3. The resulting model alongshore current $V^{(\mathrm{m})}$ reproduces the observed $V^{(\mathrm{obs})}$ well (Figure 3.7b) with small error ($\epsilon_V = 0.05\ \mathrm{m\,s^{-1}}$) and high skill (Table 3.2). Both observed and model maximum $V \approx 0.37\ \mathrm{m\,s^{-1}}$occurs near F4, with weaker near-shoreline and offshore V. As with other releases, the mean alongshore current has some alongshore variability (magenta dashed curves in Figure 3.7b).

3.4.4 Release R4

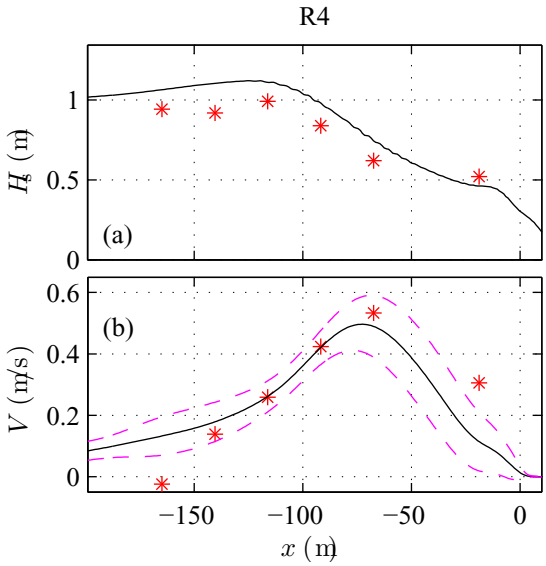

Figure 3.8: Modeled (solid) and observed (symbols) (a) $H_{\rm s}$, (b) mean alongshore current V ($\pm$ the alongshore std dev of V, dashed-magenta curves) versus x for R4. The shoreline is located at $x = 0$ m.

The R4 observed and modeled $H_{\rm s}$ are similar (Figure 3.8a), although the $H_{\rm s}^{(\rm m)}$ is biased high, leading to the largest $\epsilon_{H_{\rm s}} = 0.11$ m of all releases. The model alongshore current $V^{(\rm m)}$ reproduces the observed $V^{(\rm obs)}$ reasonably well (Figure 3.8b, $\epsilon_V = 0.10\ {\rm m\,s^{-1}}$, Table 3.2), Both model and observed maximum $V \approx 0.5\ {\rm m\,s^{-1}}$ are near F3, with weaker near-shoreline and offshore V, although the F1 and F7 V errors $\approx 0.15\ {\rm m\,s^{-1}}$.

3.4.5 Release R6

The R6 incident F7 $H_{\rm s} = 0.41$ m is about half that of the other releases, dominated by long-periods with little sea component. Similar to other releases, the model $H_{\rm s}^{(\rm m)}$ reproduces the observed $H_{\rm s}^{(\rm obs)}$ (Figure 3.9a) with small rms error $\epsilon_{H_{\rm s}} = 0.05$ m and high skill (Table 3.2). At all frames, the $V^{(\rm m)}$ reproduces well $V^{(\rm obs)}$ (Figure 3.9b) with very small errors ($\epsilon_V = 0.02\ {\rm m\,s^{-1}}$) and high skill (Table 3.2). At the observed locations seaward of the surfzone (F5–F7, $x < -110$ m), both model and observed V are

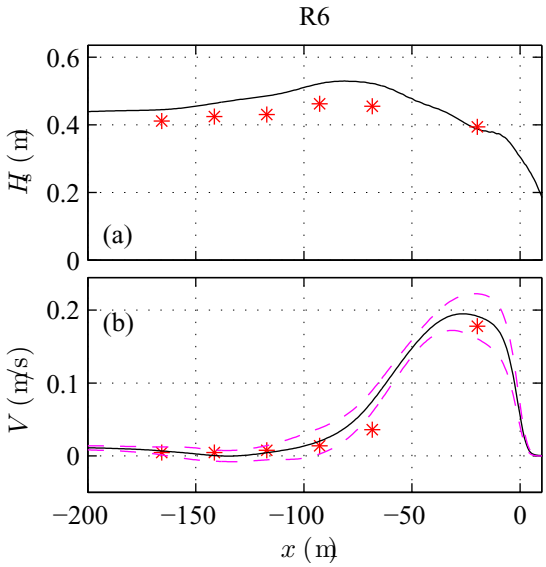

Figure 3.9: Modeled (solid) and observed (symbols) (a) $H_{\rm s}$, (b) mean alongshore current V ($\pm$ the alongshore std dev of V, dashed-magenta curves) versus x for R6. The shoreline is located at $x = 0$ m.

near-zero. Within the surfzone onshore of F3, model V rapidly increases to a maximum $V = 0.2\ {\rm m\,s^{-1}}$near F1. Except near F1, the alongshore variation in V is small.

3.5 Low-Frequency Rotational Velocity Model-Data Comparison

Low frequency ($f < 0.03$ Hz) surfzone eddies (rotational motions) were implicated in surfzone drifter dispersion [*Spydell and Feddersen*, 2009]. In addition the tracer dispersion derived cross-shore diffusivities were consistent with a mixing-length scaling that used a low-frequency rotational velocity for a velocity scale [*Clark et al.*, 2010]. Here, the ability of the `funwaveC` model to reproduce bulk low-frequency motions within the surfzone is examined.

Assuming negligible sea-surface elevation signal for surfzone rotational motions (eddies, rips, etc.), a bulk low frequency (over 0.004-0.03 Hz) rotational velocity $\mathcal{V}_{\rm rot}(x)$

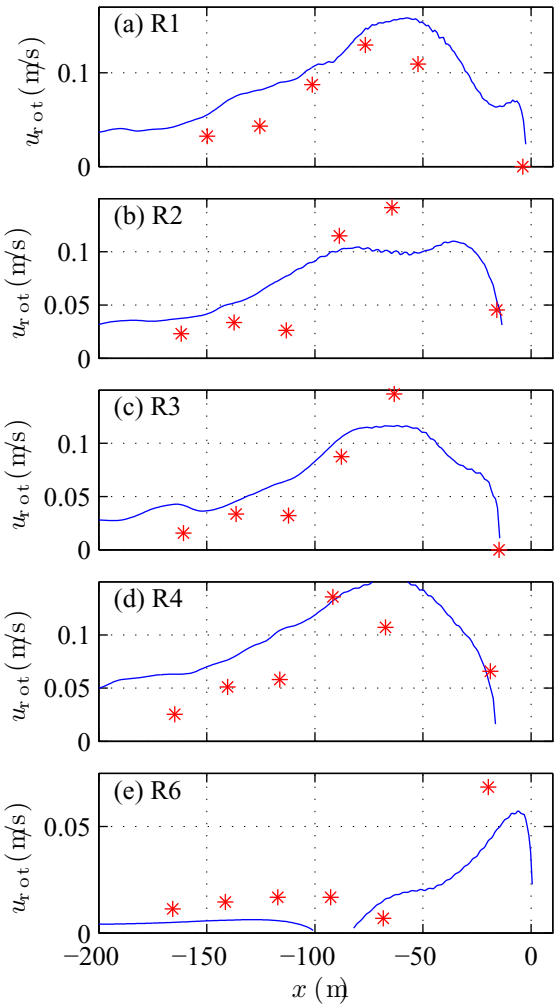

Figure 3.10: $\mathcal{V}_{\mathrm{rot}}(x)$ versus x for releases (a) R1, (b) R2, (c) R3, (d) R4, and (e) R6 for observed (asterisks) and model (solid curves). The *Lippmann et al.* [1999] method is used to derive $\mathcal{V}_{\mathrm{rot}}(x)$. The rms error $\epsilon_{\mathcal{V}_{\mathrm{rot}}(x)}$ varies between $\epsilon_{\mathcal{V}_{\mathrm{rot}}(x)} = 0.035\ \mathrm{m\,s^{-1}}$for R1 and $\epsilon_{\mathcal{V}_{\mathrm{rot}}(x)} = 0.015\ \mathrm{m\,s^{-1}}$for R6. The skill for all releases is > 0.8 and the over all releases the skill is 0.84.

[*Lippmann et al.*, 1999]

$$\mathcal{V}_{\rm rot}(x) = \left[\int_{0.004\ \rm Hz}^{0.03\ \rm Hz} (S_{uu}(f) + S_{vv}(f) - S_{\eta\eta}(f)\frac{g}{h})\mathrm{d}f\right]^{1/2} \tag{3.6}$$

removes IG wave-energy by subtracting the converted-to-velocity $S_{\eta\eta}$ spectrum from the summed cross- and alongshore velocity spectra (S_{uu} and S_{vv}, respectively). Observed and modeled $\mathcal{V}_{\rm rot}(x)$ are estimated with (3.6) integrated over the same frequency band used in *Clark et al.* [2010].

For all releases, the model reproduces the observed $\mathcal{V}_{\rm rot}(x)$ structure and magnitude (Figure 3.10). For larger wave heights releases (R1–R4, Figure 3.10a–d), the model and observed maximum $\mathcal{V}_{\rm rot}(x) \approx 0.15\ \mathrm{m\,s^{-1}}$occured around F3 and F4. Offshore of the surfzone at F7 model and observed $\mathcal{V}_{\rm rot}(x)$ are reduced, although the model overpredicts $\mathcal{V}_{\rm rot}(x)$. For releases R1–R4, the $\mathcal{V}_{\rm rot}(x)$ rms error varies between $\epsilon_{\mathcal{V}_{\rm rot}(x)} = 0.024\ \mathrm{m\,s^{-1}}$and $0.035\ \mathrm{m\,s^{-1}}$. For R6, with small waves and weak nearshoreline V, maximum $\mathcal{V}_{\rm rot}(x) \approx 0.05\ \mathrm{m\,s^{-1}}$occurs near F1, and $\mathcal{V}_{\rm rot}(x)$ decreases rapidly to very weak values at F4 and farther offshore (Figure 3.10e). For R6, the $\epsilon_{\mathcal{V}_{\rm rot}(x)} = 0.015\ \mathrm{m\,s^{-1}}$is reduced relative to the other releases. The skill for any release is > 0.8 and the mean over all releases is 0.84. The similarity between the observed and modeled $\mathcal{V}_{\rm rot}(x)$ indicates that the model reasonably reproduces the bulk low-frequency surfzone eddy field.

3.6 Summary

Accurately modeling the transport and dispersion of surfzone tracers requires a wave and circulation model that accurately represents surfzone motions from sea-swell time-scales to low-frequency and mean flows. Model-data comparisons with wave-resolving time-dependent Boussinesq models have been limited to only a few cases. The waves and current during five HB06 tracer releases are simulated with a time-dependent Boussinesq surfzone model (`funwaveC`). For each release, the observed bathymetry and incident wave conditions are used as model input. After 2000 s, the model current and eddy field has spun up within the surfzone.

The modeled and observed significant wave heights $H_{\rm s}(x)$ initially increase towards the shoreline due to shoaling, then decrease as breaking dissipates the wave en-

ergy. There is good $H_{\rm s}(x)$ agreement, with low mean (over all releases) rms errors (0.08 m) and high mean skill (as compared to a zero prediction) of 0.99. Modeled mean alongshore currents $V(x)$ are also similar to the observations with 0.05 $\mathrm{m\,s^{-1}}$ mean rms errors, and 0.95 mean skill. The $V(x)$ structure is well modeled for releases R1, R3, and R4 with mid-surfone $V(x)$ maxima close to 0.4 $\mathrm{m\,s^{-1}}$and small $V(x)$ near the shoreline, and for R6, with a maximum $V = 0.2$ $\mathrm{m\,s^{-1}}$near the shoreline. The R4 modeled and observed $V(x)$ are similar for $x < -50$ m, but the model under predicts the observed near-shoreline maxima ($V = 0.31$ $\mathrm{m\,s^{-1}}$) by 0.25 $\mathrm{m\,s^{-1}}$.

Modeled and observed low frequency (< 0.03 Hz) horizontal rotational velocities $\mathcal{V}_{\rm rot}(x)$, possibly important for cross-shore dispersion, have similar cross-shore structure. The $\mathcal{V}_{\rm rot}(x)$ mean skill is high (0.84), although $\mathcal{V}_{\rm rot}(x)$ magnitudes are slightly over predicted. The wave and current model-data agreement indicates that a further comparison of modeled tracer plumes (Chapter 4) is appropriate.

Chapter 3, in part is currently being prepared for submission for publication of the material. Clark, David B.; Feddersen, Falk; Guza, R.T. The dissertation author was the primary investigator and author of this material.

Chapter 4

Boussinesq Modeling of Surfzone Tracer Plumes: Part 2, Tracer Model-data Comparison

4.1 Introduction

The rates and mechanisms for surfzone tracer dispersal are poorly understood. Accurately predicting the transport and dispersal of tracers (e.g., pollution, nutrients, sediment, and larvae) requires a better knowledge of the processes that control dispersion rates. Surfzone numerical models can provide insight into surfzone tracer dispersion, however surfzone tracer model validation is scarce or non-existent.

Surfzone tracer dispersion has only been measured a few times [e.g., *Harris et al.*, 1963; *Inman et al.*, 1971; *Clarke et al.*, 2007; *Clark et al.*, 2010], thus few data sets are available for model validation. The scope of these experiments ranges from point concentration measurements at the shoreline [*Harris et al.*, 1963; *Clarke et al.*, 2007] or the visually estimated center of a dye patch [*Inman et al.*, 1971], to repeated cross-shore concentration transects at through a dye plume at multiple alongshore locations with a dye sampling jet ski [*Clark et al.*, 2010]. Only the most recent study [i.e., *Clark et al.*, 2010] has the detailed wave and current measurements necessary to validate numerical simulations of waves and currents, a necessary precursor to model-data comparisons of

tracer transport and dispersion.

Surfzone tracer dispersion has been modeled with analytic and numerical models of varying complexity. Simple Fickian analytic models have been used to estimate bulk diffusion coefficients from field data [*Harris et al.*, 1963; *Inman et al.*, 1971; *Clarke et al.*, 2007; *Clark et al.*, 2010]. Fickian models provide a framework for calculating diffusivities in the surfzone, and may provide good predictive capability if used with the appropriate diffusion coefficient. However, diffusion coefficients in the surfzone are poorly known.

An idealized study of breaking wave driven cross-shore tracer diffusion [*Feddersen*, 2007] used a moving region of diffusivity to simulate the turbulent mixing on the front face of a broken wave (bore), and found a non-dimensional cross-shore average diffusivity $\hat{\kappa} = \sqrt{\pi}/(\hat{c}\hat{T})$ [*Henderson*, 2007], where $\hat{c}$ and $\hat{T}$ are the non-dimensional cross-shore wave speed and wave period. The dimensionalized form of the average cross-shore diffusivity $\kappa_{xx} \sim H_{\rm s}^2 T_{\rm m}^{-1}$ [*Clark et al.*, 2010], where $H_{\rm s}$ and $T_{\rm m}$ are the incident significant wave height and mean period, respectively, is equivalent to breaking wave cross-shore diffusivity scalings suggested by past field studies [*Harris et al.*, 1963; *Inman et al.*, 1971]. However, this scaling did not find good agreement with recent observations [*Clark et al.*, 2010].

Wave average (WA) numerical models (averaged over a wave period), typically solving non-linear shallow water equations, have been used to examine tracer dispersion in the nearshore and surfzone [e.g., *Rodriguez et al.*, 1995; *Tao and JianHua*, 2006; *Issa et al.*, 2010]. WA models do not contain rich vorticity fields, or finite-crest-length wave breaking [*Peregrine*, 1998], indicated as a primary source of surfzone 2-D (vertical) vorticity [*Spydell and Feddersen*, 2009]. Thus, the model diffusivities are parameterized as functions of wave or current conditions, although none of these parameterizations have been validated in the surfzone. Comparison of WA tracer dispersion to observations is very limited [*Rodriguez et al.*, 1995].

Time-dependent wave-resolving surfzone models (most commonly Boussinesq models) contain waves and currents with periods from the sea-swell band (including individual breaking events) to the mean flow. Boussinesq surfzone models solve an extended version of the nonlinear shallow water equations with weak nonlinearity and dis-

persion [e.g., *Peregrine*, 1967; *Nwogu*, 1993; *Wei et al.*, 1995], and handle directionally-spread random wave fields (Chapter 3). They have been used to examine surfzone drifter dispersion [*Johnson and Pattiaratchi*, 2006; *Spydell and Feddersen*, 2009], but have not been used for surfzone tracer modeling. Depth averaged tracer concentration can be simulated with an advection diffusion equation coupled to a Boussnesq model. This type of model contains mixing by the horizontal eddy field (e.g., vertical vorticity) without the need for parameterization. Boussinesq models are quasi-depth averaged, and lack cross-shore dispersion by vertically sheared currents (i.e., undertow). However, this mechanism was not estimated to be significant in a natural surfzone with directionally spread waves [*Clark et al.*, 2010]. Furthermore, rapid vertical mixing within the surfzone [e.g., *Feddersen and Trowbridge*, 2005; *Feddersen*, 2010b] implies little vertical tracer structure, however this may not be the case seaward of the surfzone.

Here, surfzone tracer observations from the HB06 experiment in Huntington Beach, California [*Clark et al.*, 2010] are simulated with the Boussinesq surfzone model `funwaveC` . Tracer model-data comparison first requires a well modeled surfzone, where waves and currents are similar to the observations. The model setup, including model equations, model domain and boundary conditions are given in Chapter 3, and the modeled waves and currents have good qualitative agreement with observations. The HB06 tracer experiments and existing results are summarized in Section 4.2. The `funwaveC` tracer equations are given in Section 4.3, along with the tracer domain and boundary conditions.

The `funwaveC` model allows for a broad range of ways to examine surfzone tracer dispersion that are not presently available from field data. However, for the purpose of model-data comparison, the means, fluxes and moments presented here (Sections 4.4-4.5) are calculated using the same equations as the HB06 field data [*Clark et al.*, 2010]. The model-data agreement is discussed (Section 4.6.1), along with the relevance of modeled wave breaking eddy diffusivity (Section 4.6.3) and scalings for modeled cross-shore diffusivity κ_{xx} (Section 4.6.4). A summary is given in Section 4.7.

4.2 HB06 Observations

The surfzone component of the HB06 experiment was carried out at Huntington Beach, California, located in the center of the Southern California Bight. The southwest facing beach is sheltered by offshore islands that block normally incident swell. During HB06 (14 Sep – 17 Oct, 2006) the predominant south swell drove strong alongshore currents upcoast (towards the northwest). Waves and currents were measured on a cross-shore array of 7 bottom mounted tripods (denoted F1-F7 from closest to farthest from the shoreline) with acoustic Doppler velociometers and pressure sensors spanning 140 m in the cross-shore, from near the shoreline to roughly 4 m water depth. The instruments at F2 had frequent problems, and are left out of the subsequent analysis. Significant wave heights $H_{\rm s}$ ranged from 0.41–1.02 m during the tracer releases, with mean wave periods $T_{\rm m}$ from 9–9.9 s, and directional spreads σ_θ from 15–23 degrees. Mean (in time) alongshore currents $V(x)$ (where x is the cross-shore distance from the shoreline) were generally maximum near mid-surfzone, except for one release with maximum $V(x)$ near the shoreline (Chapter 3). Details of HB06 Eulerian wave and current observations are given in *Clark et al.* [2010] and Chapter 3.

4.2.1 Tracer Releases

Cross-shore dispersion analysis was studied using 5 continuous tracer releases (denoted R1, R2, R3, R4, and R6) performed on different days throughout the month-long HB06 experiment. Tracer was released 0.5 m above the bed in roughly 1 m water depth (4–54 m from the shoreline). Dye was pumped at rate between $1.3 - 7.1\ \mathrm{mL\,s^{-1}}$(263–1489 ppb $\mathrm{m^3\,s^{-1}}$), and advected downstream with the mean alongshore current forming a plume in the y (alongshore distance from the dye source) direction. Dye tracer was measured near the surface for 40–121 minutes with a jet ski mounted fluorometer system [*Clark et al.*, 2009, 2010]. Dye was sampled on repeated cross-shore transects at 3–9 downstream locations, between 16–565 m from the tracer source, with the mean degrees of freedom per transect ranging between 7–15 per release [*Clark et al.*, 2010].

4.2.2 Review of Observed HB06 Plume Properties

Rapid vertical tracer mixing was visually observed, with tracer reaching the surface within 1 m of the source. Surfzone tracer plumes were visually patchy and highly variable. The mean cross-shore tracer profiles $\overline{D}(x, y_j)$ had decreasing peak concentrations and increasing cross-shore widths with downstream distance y from the dye source. The cross-shore profiles were often shoreline attached, roughly resembling a half-Gaussian, with a maxima near the shoreline. The tracer cross-shore integrated surface-center of mass $\mu(y_j)$ (from mean $\overline{D}$ profiles) moved away from the shoreline with downstream distance from the source, and was consistent with a simple Fickian equation for tracer diffusion near a boundary. Bulk cross-shore surfzone diffusivities κ_{xx} were estimated from the downstream evolution of the plume squared cross-shore length scale, and varied between 0.5–2.5 $\mathrm{m^2\,s^{-1}}$. The κ_{xx} variation was examined with three scalings: bore diffusion, low frequency 2-D eddy mixing, and cross-shore shear (undertow) dispersion, where the low frequency eddy scaling agreed best with the data.

4.3 Tracer Modeling

The 5 tracer releases analyzed in *Clark et al.* [2010] are simulated with a time-dependent wave-resolving Boussinesq model (`funwaveC`). The model implements momentum equations following *Nwogu* [1993], a wave maker following *Wei et al.* [1999], and parameterized wave breaking following *Kennedy et al.* [2000]. The observed bathymetry is roughly alongshore uniform and the alongshore-averaged bathymetry, over the observed tracer release region, is used here (Figure 4.1b). Waves matching the observed incident angle, directional spread, and energy spectrum are generated by the model wavemaker, allowed to propagate freely towards the shoreline where they "break" and dissipate (by the breaking eddy viscosity ν_{br}), and drive alongshore currents and surfzone eddies. The Boussinesq model equations, general model setup, and the details of waves and currents generated by the model are given in Chapter 3.

Aside from the proscribed incident waves and bathymetry, the currents and circulation develop freely according to model dynamics. Model-data comparisons for HB06 Eulerian statistics during tracer releases is given in Chapter 3. In summary,

there is agreement between the observed and modeled significant wave height $H_{\rm s}(x)$, mean alongshore current $V(x)$, and bulk rotational velocities $\mathcal{V}_{\rm rot}(x)$ (a possible mixing mechanism) with cross-shore distance x from the $x = 0$ shoreline.

Coupled to the standard time-dependent Boussinesq model `funwaveC` is a depth-averaged tracer module. This module allows for three separate non-interacting model tracers. Each tracer is released at a specified point within the model domain over a specified time period. Each of the three model tracers evolve according to a tracer advection-diffusion equation,

$$\frac{\partial([h+\eta)D]}{\partial t} + \boldsymbol{\nabla}\cdot[(h+\eta)\boldsymbol{u}D] = \boldsymbol{\nabla}\cdot[(\kappa_{\rm br}+\kappa_0)(h+\eta)\boldsymbol{\nabla}D] \tag{4.1}$$

where D is the tracer concentration, h is the still water depth, η is the free surface elevation, $\kappa_{\rm br}$ is the breaking-wave eddy diffusivity, κ_0 is the background eddy diffusivity, $\boldsymbol{\nabla}$ is the 2D horizontal gradient operator, and $\boldsymbol{u}$ is the horizontal velocity vector, which for small kh is approximately the depth-averaged velocity. Model tracer is advected by both orbital wave velocities and mean/low-frequency currents.

In (4.1), $\kappa_{\rm br}$ is set equal to the the breaking-wave eddy viscosity $\nu_{\rm br}$ (e.g., momentum and tracer are assumed to mixed identically - the tracer Schmidt number is one), and the background diffusivity is set to $\kappa_0 = 0.01\ {\rm m^2\,s^{-1}}$ (two orders of magnitude smaller than the observed bulk κ_{xx}). The $\kappa_{\rm br}$ is applied only on the "breaking" front face of a wave, whereas the κ_0 is applied everywhere in the tracer domain. The inclusion of the breaking eddy viscosity allows the breaking-wave cross-shore tracer dispersion mechanism discussed in *Feddersen* [2007] to be examined relative to other tracer dispersion mechanisms (Section 4.6.3).

As discussed in Chapter 3, model sponge layers are located on the on- and offshore boundaries, and an offshore wavemaker generates waves (shaded regions in Figure 4.1a). The cross-shore extent of the tracer domain (dashed lines, Figure 4.1a) is a subset of the full domain. The offshore tracer boundary is located just onshore of the wavemaker region and ranges from $x = 232$ m to 260 m from the shoreline. The offshore tracer boundary condition is set to $D = 0$. The onshore tracer boundary is typically located ~ 5 m onshore of the start of the sponge layer (the of the flat region is $h_0 = 0.2 - 0.35$ m) where a no-flux boundary condition is applied. In contrast to the η and $\boldsymbol{u}$ periodic alongshore boundary conditions, the tracer alongshore boundary

conditions are open so tracer advects out of the domain.

To account for `funwaveC` model spinup, the continuous tracer source is turned on at $t = 2000$ s at alongshore locations $Y = 250$ m, $Y = 500$ m, and $Y = 750$ m from the upstream boundary (on $L_y = 1500$ m alongshore domain), for the 3 different tracers A, B, and C, respectively (Figure 4.1a). The model cross-shore release location x_0 varies from $x_0 = -10$ to -54 m (Table 4.1). The model tracer is injected at the same rate as the observed dye pump rate, and varies from 263–1489 ppb $\mathrm{m}^3\,\mathrm{s}^{-1}$(Table 4.1).

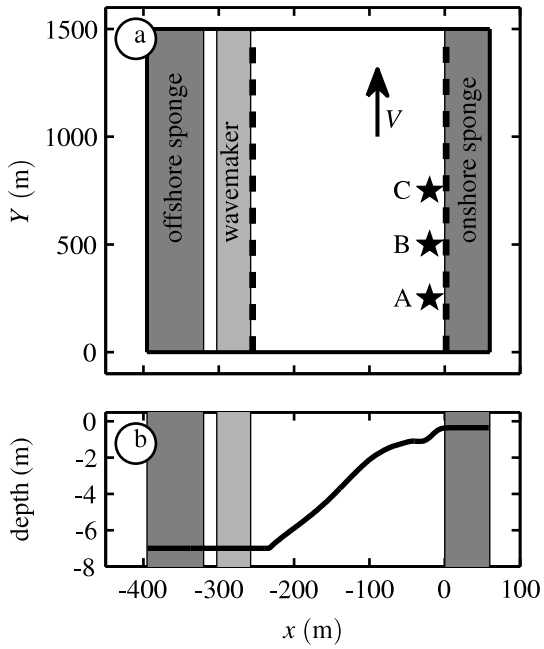

Figure 4.1: (a) Typical model domain (R4 example) as a function of x (cross-shore distance from the "shoreline") and Y (alongshore) with gray regions indicating sponge layers and the wavemaker. The cross-shore tracer domain (dashed lines) is bounded by the offshore wavemaker and the onshore sponge layer. Tracer boundary conditions are open at the alongshore edges, set to zero along the offshore edge, and a no-flux boundary condition at $x = 0$. Stars indicate tracer release locations for model tracer A ($Y = 250$ m), B (500 m), and C (750 m), and the arrow indicates the direction of the mean alongshore current V. (b) Typical cross-shore model bathymetry versus x (R4 example), with a flat region at 7 m depth for the offshore sponge layer and wavemaker and a 0.3 m depth flat region for the onshore sponge layer.

Table 4.1: Model tracer release parameters: input tracer flux M_0, cross-shore release location x_0.

Release	M_0 (ppb $\mathrm{m}^3\,\mathrm{s}^{-1}$)	x_0 (m)
R1	263	-54
R2	647	-13
R3	1256	-10
R4	1489	-22
R6	485	-12

4.3.1 Model Tracer Output

Model tracer concentrations $D^{(\mathrm{A,B,C})}$ are output every 2 seconds over the entire domain, along with sea surface elevation η, cross- and alongshore currents (u and v), and breaking wave eddy diffusivity κ_{br}. Instantaneous $D^{(\mathrm{A})}$ model tracer plumes (Figure 4.2a,c,e) are patchy with adjacent regions of high and low concentration and tendril-like structures. Vortex stuctures are apparent in the tracer field, especially in regions farther from the shoreline ($x < -100$ m). Mean tracer $\overline{D}^{(\mathrm{A})}$ plumes (averaged from 6000–14000 s after the tracer release started, Figure 4.2b,d,f) are much smoother, where averaging has removed fine structures. The mean plumes have shore-parallel axes, with peak concentrations decreasing and cross-shore widths increasing with downstream distance y from the tracer source. The absolute concentration (i.e., ppb) varies between model releases (relative shades of gray between panels in Figure 4.2), and correspond to different tracer injection rates (Table 4.1), the magnitude of V (stronger V decreases tracer concentrations for a given injection rate), and the intensity of the cross-shore mixing.

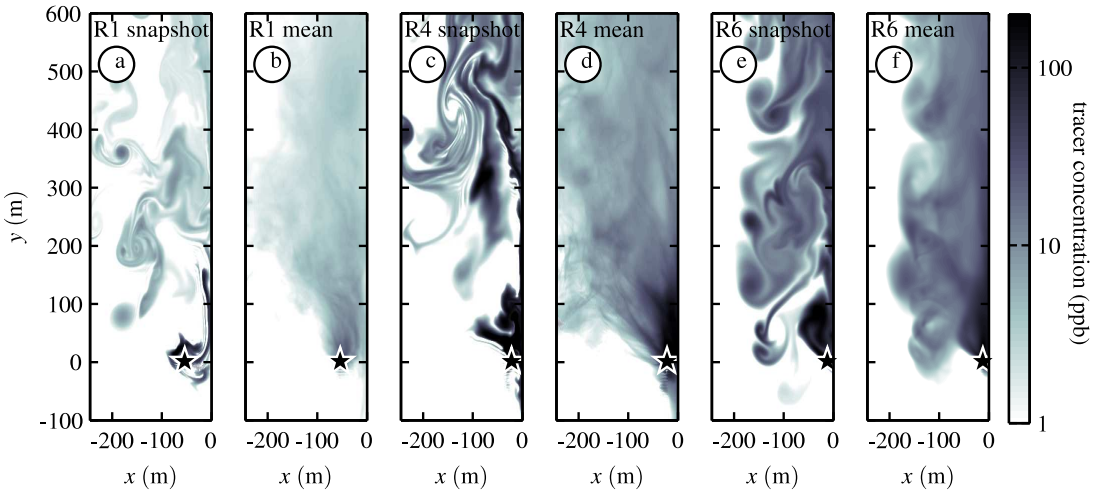

Figure 4.2: (a, c, e) Instantaneous $D^{(\mathrm{A})}$ and (b, d, f) mean $\overline{D}^{(\mathrm{A})}$ (time average over 6000–14000 s after each tracer release begins) modeled tracer concentration (tracer A) vs x, the cross-shore distance from the "shoreline", and y, the alongshore distance from the dye source, for (a, b) R1, (c, d) R4, and (e, f) R6. Tracer is released at the black star in each panel, and the cross-shore release locations x_0 are given in Table 4.1.

4.4 Tracer Means and Alongshore Flux: Model Data Comparison

4.4.1 Mean Cross-shore Profiles

Mean model tracer concentrations $\overline{D}^{(\mathrm{A})}(x,y)$, $\overline{D}^{(\mathrm{B})}(x,y)$, and $\overline{D}^{(\mathrm{C})}(x,y)$ are the time averages of tracers A, B, and C in a fixed reference frame. Averages over 6000-14000 s after tracer release begins avoid initial tracer plume transients (Figure 4.3) for $0 < y < 250$ (where surfzone diffusivities are estimated). The plume is absolute averaged (e.g., in fixed coordinates) and includes any plume meandering, in contrast with relative averaging (e.g., in center of mass coordinates, *Batchelor* [1952]; *Csanady* [1973]; *Fong and Stacey* [2003]), which attempts to separate large scale plume meandering from smaller scale mixing. Absolute averaging is used here because the interpretation of relative averages is unclear near the shoreline boundary [*Clark et al.*, 2010].

Three representative model $\overline{D}^{(\mathrm{A})}$ profiles at various downstream y are shown for each release (Figure 4.4). Model $\overline{D}^{(\mathrm{A})}$ profiles for R3, R4, and R6 are similar to

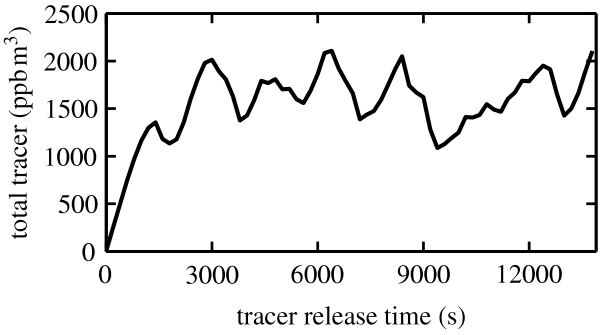

Figure 4.3: Total tracer integrated from the upstream model boundary to 250 m downstream of the tracer source versus time after the tracer release began, for R1 tracer A. Tracer means taken 6000 s after the tracer release begins, avoid initial plume transients (<3000 s). Other releases and tracers (A, B, C) are similar.

each other and to observed $\overline{D}^{(\mathrm{obs})}$ (Figure 4.4c,d,e). The $\overline{D}^{(\mathrm{A})}$ and $\overline{D}^{(\mathrm{obs})}$ both increase towards the shoreline, with decreasing peak concentrations and increased cross-shore width with downstream distance y from the source (Figure 4.4c,d,e). These $\overline{D}^{(\mathrm{A})}$ are usually shoreline attached, with maxima at or near the shoreline (Figure 4.4c,d,e), but occasionally have peaks shoreward of the observations with decreasing tracer concentrations near the shoreline (e.g., $y = 84$ m in Figure 4.4d). The tracer concentration skill for each transect is estimated by $1 - \langle(\overline{D}^{(\mathrm{obs})}(x,y) - \overline{D}^{(\mathrm{A,B,C})}(x,y))^2\rangle / \langle\overline{D}^{2\,(\mathrm{obs})}(x,y)\rangle$ for regions where $\overline{D}^{(\mathrm{obs})} > 5$ ppb. Mean R3, R4 and R6 skills, averaged over all the transects in each release and the three model tracers, are between 0.5 and 0.73 (Table 4.2), consistent with the qualitative agreement in Figure 4.4c,d,e.

For release R1 the cross-shore structure for $\overline{D}^{(\mathrm{A})}$ and $\overline{D}^{(\mathrm{obs})}$ have roughly similar shapes and magnitudes, and both model and observed spread in the cross-shore with downstream distance (Figure 4.4a). However, at $y = 56$ and 107 m the $\overline{D}^{(\mathrm{A})}$ plume is closer to the shoreline than $\overline{D}^{(\mathrm{obs})}$ (Figure 4.4a), consistent with seaward advection of the observed plume [*Clark et al.*, 2010]. The cross-shore displacement of $\overline{D}^{(\mathrm{A})}$ and $\overline{D}^{(\mathrm{obs})}$ plume locations produce negative skill for R1 (Table 4.2), despite similar cross-shore shapes and magnitudes.

Release R2 also has negative skill (Table 4.2). The R2 $\overline{D}^{(\mathrm{A})}$ does spread and decrease similar to $\overline{D}^{(\mathrm{obs})}$, however the $\overline{D}^{(\mathrm{A})}$ magnitudes are much larger than $\overline{D}^{(\mathrm{obs})}$ (Figure 4.4b). The differences in tracer magnitude are most pronounced near the shore-

line where $\overline{D}^{(\mathrm{A})}$ are often twice a large as $\overline{D}^{(\mathrm{obs})}$ (Figure 4.4b).

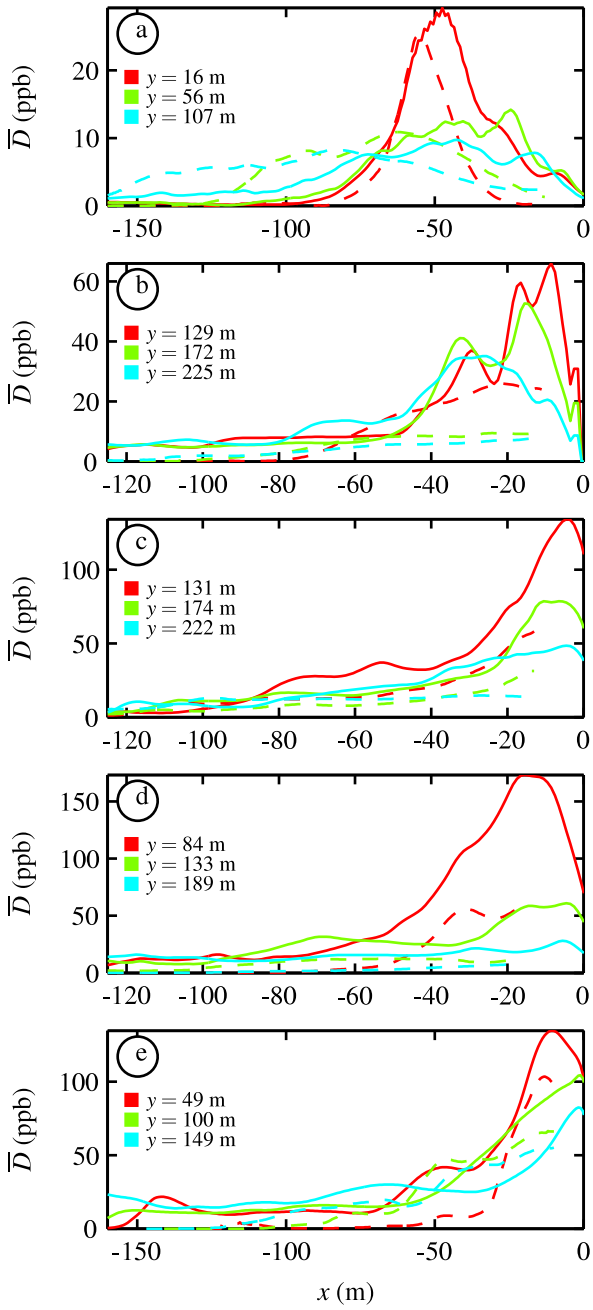

Figure 4.4: Modeled $\overline{D}^{(\mathrm{A})}$ (solid) and observed $\overline{D}^{(\mathrm{obs})}$ (dashed) mean cross-shore tracer profiles vs x for (a) R1, (b) R2, (c) R3, (d) R4, and (e) R6, with alongshore distance y from the source indicted by the legend in each panel. Observed transects extend from seaward of the tracer plume to the inner transect edge x_{in}.

Table 4.2: Mean $\overline{D}^{(\mathrm{A,B,C})}$ versus $\overline{D}^{(\mathrm{obs})}$ skill, averaged over all observed transects and model tracers $\overline{D}^{(\mathrm{A})}$, $\overline{D}^{(\mathrm{B})}$, and $\overline{D}^{(\mathrm{C})}$ for each release.

R1	R2	R3	R4	R6
-2.70	-8.89	0.70	0.50	0.73

4.4.2 Alongshore Tracer Flux

Model alongshore tracer fluxes $M^{(\mathrm{A,B,C})}(y)$ are estimated following the observed $M^{(\mathrm{obs})}(y)$ definition [*Clark et al.*, 2010]

$$M(y) = \int_{x_{\mathrm{F7}}}^{x_{\mathrm{in}}} h(x)V(x,y)\,\overline{D}(x,y)\,dx, \tag{4.2}$$

where the inner cross-shore integral limit is the observed inner transect edge x_{in} (i.e., where observations end near the shoreline, Figure 4.4) and the outer limit is the F7 location x_{F7} (the farthest seaward velocity observation), and $V(x,y)$ is the mean alongshore current averaged over the same times as $\overline{D}(x,y)$. The x_{in} range from -17 to -10 m, and x_{F7} range from -146 to -162 m from the shoreline. This $M(y)$ estimate excludes the region shoreward of x_{in} and seaward of x_{F7} where tracer concentrations may be significant (e.g., $\overline{D}^{(\mathrm{A})}$ with $x > -15$ m in Figure 4.4c). The model and observed $M(y)$ use time averages $V(x,y)$ and $\overline{D}(x,y)$, thus excluding alongshore eddy fluxes.

The $M^{(\mathrm{A,B,C})}$ are similar to $M^{(\mathrm{obs})}$ for releases R1, R2, and R4 (Figure 4.5a,b,d), and generally overestimated for R3 and R6 (Figure 4.5c,e). All $M^{(\mathrm{A,B,C})}$ have roughly similar structure to $M^{(\mathrm{obs})}$ with slightly decreasing $M^{(\mathrm{A,B,C})}$ at large y. There are large differences in flux estimates between individual $M^{(\mathrm{A})}$, $M^{(\mathrm{B})}$, and $M^{(\mathrm{C})}$, with the variation often close to 50% of $M^{(\mathrm{A,B,C})}$ magnitudes (Figure 4.5).

The model tracer input flux is equal to the observed dye pump flux $M^{(\mathrm{obs})}(y = 0)$, however the $M^{(\mathrm{A,B,C})}$ do not necessarily match at the source. In contrast, the cross-shore integrated mean time-dependent tracer fluxes (only available from the model, Section 4.6.2) $\overline{v(x,y,t)D(x,y,t)}$ do match the input flux at $y = 0$, with little variation between tracers (A, B, and C). Alongshore eddy fluxes may be significant, and may partially account for the difference between the observed pump flux ($y = 0$, black circles in Figure 4.5) and fluxes estimated from observations on downstream transects $M^{(\mathrm{obs})}(y > 0)$.

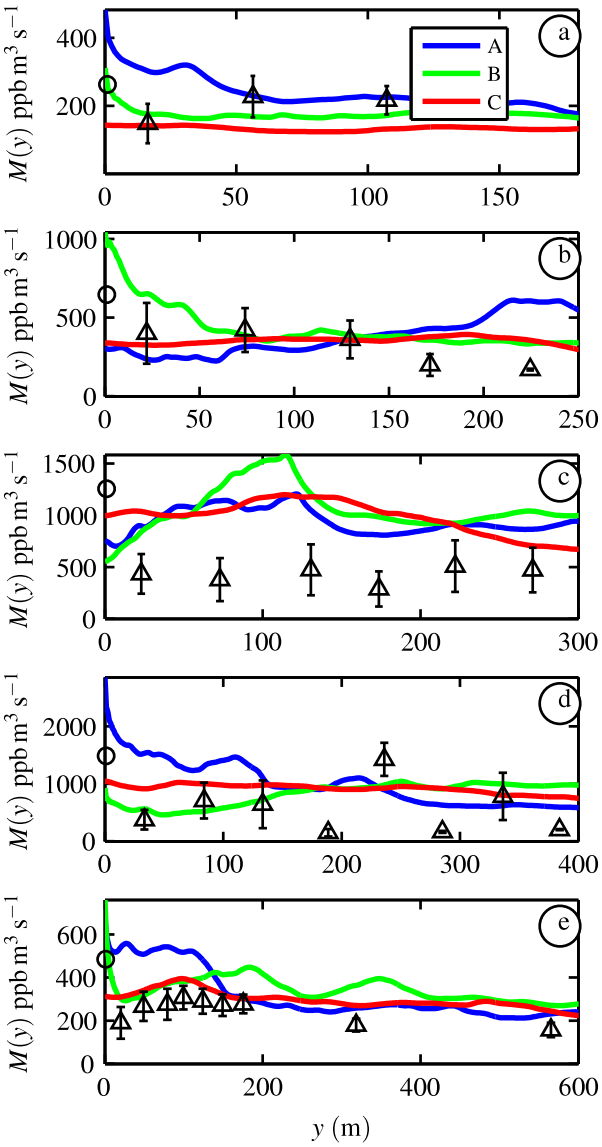

Figure 4.5: Modeled $M^{(\mathrm{A,B,C})}$ (colored curved) and observed $M^{(\mathrm{obs})}$ transect estimated (black triangles with error bars) alongshore tracer fluxes (4.2) vs y, for releases (a) R1, (b) R2, (c) R3, (d) R4, and (e)R6. The observed pumped dye release rate is estimated by the black circle at $y = 0$

4.5 Cross-shore Integrated Moments, and Surfzone κ_{xx}

4.5.1 Definitions

Cross-shore integrated tracer moments are used to compare generalized cross-shore plume structure. The moments are normalized by the cross-shore $\overline{D}$ integral, removing the dependence on model $\overline{D}^{(\mathrm{A,B,C})}$ absolute concentrations.

The surface-center of mass μ is the $\overline{D}$ first moment

$$\mu(y) = \frac{\int_{x_{\mathrm{out}}}^{x_{\mathrm{in}}} x\, \overline{D}(x,y)\, dx}{\int_{x_{\mathrm{out}}}^{x_{\mathrm{in}}} \overline{D}(x,y)\, dx}, \tag{4.3}$$

where x_{out} is the offshore extent of the observed transects (observed x_{out} varies from -105 to -298 m over all transects because the jet ski always drives seaward until dye concentrations are no longer detectable) or the offshore extent of the modeled tracer (constrained by the seaward boundary).

Surfzone κ_{xx} is estimated using the surfzone specific $\overline{D}$ squared cross-shore length scale σ^2_{surf}, a shoreline based second moment integrated over the surfzone [*Clark et al.*, 2010]

$$\sigma^2_{\mathrm{surf}}(y) = \frac{\int_{-L_x}^{x_{\mathrm{in}}} x^2\, \overline{D}(x,y)\, dx}{\int_{-L_x}^{x_{\mathrm{in}}} \overline{D}(x,y)\, dx}, \tag{4.4}$$

where the integral is taken over the observed limits from the seaward extent of the surfzone $x = -L_x$ (at the location of maximum H_{s}) to $x = x_{\mathrm{in}}$. Observed H_{s} are only estimated at discrete locations (instrumented frames are roughly 20 m apart), thus the resolution for determining L_x is corse. Model and observed L_x are similar (12 m rms difference), and for comparison, observed L_x are used to estimate model and observed σ^2_{surf} (4.4). The shoreline based (i.e., without subtracting μ) moment is appropriate for estimating κ_{xx} near a boundary, assuming the alongshore plume axis is parallel to the shoreline (i.e., no large scale cross-shore advection of the mean plume, *Clark et al.* [2010]).

A bulk surfzone cross-shore diffusivity κ_{xx} for each release is estimated from the σ^2_{surf} that are well contained in the surfzone, thus representing surfzone diffusion rather than diffusion seaward of the surfzone. Transects are well contained when $\mathcal{R} < 0.55$, where $\mathcal{R}$ is the ratio of plume $\sigma^2_{\mathrm{surf}}(t_{\mathrm{p}})$ to the theoretical value of σ^2_{surf} if tracer

concentrations were constant across the surfzone [*Clark et al.*, 2010]. For each release, the bulk κ_{xx} is estimated by a linear fit to $\sigma^2_{\rm surf}$ versus $t_{\rm p}$

$$\sigma^2_{\rm surf} = 2\kappa_{xx} t_{\rm p} + \beta, \tag{4.5}$$

where κ_{xx} and β are fit constants, and $t_{\rm p}$ is the plume alongshore advection time

$$t_{\rm p} = \overline{V}^{-1} y. \tag{4.6}$$

The $t_{\rm p}$ estimates the plume age at a downstream location y. The observed $t_{\rm p}$ use the surfzone averaged mean alongshore current $\overline{V}$ from the cross-shore array of current meters, and the model $t_{\rm p}$ use the surfzone (cross-shore) and alongshore-averaged mean current $\overline{V}$ from the region between the release location $y = 0$ and the farthest downstream location with $\Re < 0.55$ (i.e., the region where κ_{xx} is estimated).

4.5.2 Surface Center of Mass μ: Model Data Comparison

The observed $\mu^{(\rm obs)}$ and modeled $\mu^{(\rm A,B,C)}$ generally decrease (move seaward) with downstream distance y (Figure 4.6). The rate that μ moves away from the shoreline is roughly constant for all $\mu^{(\rm obs)}$ except R6, which has decreased seaward $\mu^{(\rm obs)}$ movement for $y > 200$ m. The observed R6 was sampled farther downstream than the other releases making observations of tracer interacting with weaker diffusivities seaward of the surfzone more likely, and consistent with the nearly constant $\mu^{(\rm obs)}$ for $y > 200$ m. The decreased seaward $\mu^{(\rm A,B,C)}$ movement, apparent for most model releases at $y > 200$ m, may be caused by weaker mixing seaward of the surfzone or by interaction with the offshore boundary.

The downstream evolution of $\mu^{(\rm obs)}$ and $\mu^{(\rm A,B,C)}$ are very similar for R2, R3, and R4 (Figure 4.6b,c,d). The R1 $\mu^{(\rm obs)}$ and $\mu^{(\rm A,B,C)}$ are similar at the closest transect to the source (Figure 4.6a), but $\mu^{(\rm obs)}$ magnitudes are larger than $\mu^{(\rm A,B,C)}$ for the two farthest downstream transects, consistent with seaward advection of the observed R1 plume, possibly by local bathymetric variation [*Clark et al.*, 2010]. The R6 modeled $\mu^{(\rm C)}$ closely match the $\mu^{(\rm obs)}$, but $\mu^{(\rm A)}$ and $\mu^{(\rm B)}$ magnitudes are generally larger than the $\mu^{(\rm obs)}$, with more variation along individual $\mu^{(\rm A)}$ and $\mu^{(\rm B)}$ than the $\mu^{(\rm obs)}$. The larger magnitude and variation correspond with small patches of low $\overline{D}^{(\rm A)}$ and $\overline{D}^{(\rm B)}$ lingering seaward of the surfzone.

Model-data agreement is summarized by the μ model skill, estimated by $1 - \langle(\mu^{(\mathrm{obs})}(y) - \mu^{(\mathrm{A,B,C})}(y))^2\rangle / \langle\mu^{2\,(\mathrm{obs})}(y)\rangle$, for each tracer and release. The mean $\mu^{(\mathrm{A,B,C})}$ skill over all releases and tracers is 0.88 indicating good model-data agreement.

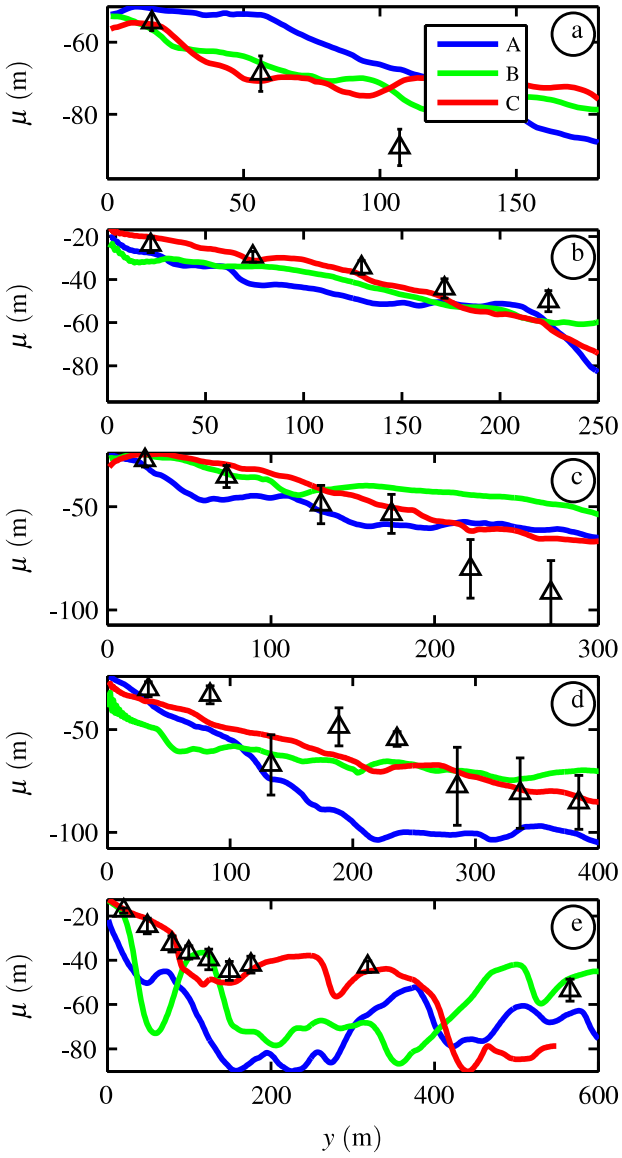

Figure 4.6: Modeled (colored) and observed (black triangles with error bars) surface center of mass μ vs y for releases (a) R1, (b) R2, (c) R3, (d) R4, and (e)R6. The mean skill over all releases is 0.88.

4.5.3 Cross-shore Length Scale, and κ_{xx}

Consistent with the observed cross-shore spreading with downstream distance (Figure 4.4), the plume squared cross-shore length scale $\sigma^2_{\rm surf}$ (4.4) increases with the plume alongshore advection time $t_{\rm p}$ (4.6) (Figure 4.7). The model $\sigma^{2\,({\rm A,B,C})}_{\rm surf}$ and observed $\sigma^{2\,({\rm obs})}_{\rm surf}$ magnitudes are similar, and the overall shape of $\sigma^2_{\rm surf}$ versus $t_{\rm p}$ are well modeled for R2, R3, R4, and R6 (Figure 4.7b,c,d,e). The $\sigma^{2\,({\rm A,B,C})}_{\rm surf}$ skill at observed transect locations (square symbols, Figure 4.7) is $1 - \langle(\sigma^{2\,({\rm obs})}_{\rm surf}(t_{\rm p}) - \sigma^{2\,({\rm A,B,C})}_{\rm surf}(t_{\rm p}))^2\rangle / \langle(\sigma^{2\,({\rm obs})}_{\rm surf}(t_{\rm p}))^2\rangle$. The mean $\sigma^{2\,({\rm A,B,C})}_{\rm surf}$ skill for releases R2, R3, R4, and R6 is 0.92.

The R1 $\overline{D}^{({\rm obs})}$ are different from the other releases because the plume does not interact strongly with the shoreline, but the the mean plume moves seaward (Figure 4.4a), as discussed in *Clark et al.* [2010]. Thus, the R1 observations are treated as a special case, with κ_{xx} estimated from the squared cross-shore length scale σ^2

$$\sigma^2(y) = \frac{\int_{x_{\rm out}}^{x_{\rm in}} [x - \mu^{({\rm obs})}(y)]^2 \overline{D}^{({\rm obs})}(x,y) dx}{\int_{x_{\rm out}}^{x_{\rm in}} \overline{D}^{({\rm obs})}(x,y) dx}, \tag{4.7}$$

where the seaward advection of the mean plume is removed. The R1 $\overline{D}^{({\rm A,B,C})}$ interact with the shoreline and do not exhibit the same non-dispersive cross-shore advection (Figure 4.4a), thus $\sigma^{2\,({\rm A,B,C})}_{\rm surf}$ (4.4) are used for estimating model $\kappa^{({\rm A,B,C})}_{xx}$. For the purpose of comparison (Figure 4.7a), the R1 $\sigma^{2\,({\rm obs})}(t_{\rm p})$ is compared with the modeled $\sigma^{2\,({\rm A,B,C})}_{\rm surf}(t_{\rm p}) - \overline{\sigma^{2\,({\rm A,B,C})}_{\rm surf}}(t_{\rm p} = 0)$. The R1 modeled and observed squared cross-shore length scales evolve similarly (Figure 4.7a). This R1 model-data comparison is qualitative and skill is not estimated.

Modeled cross-shore surfzone diffusivities $\kappa^{({\rm A,B,C})}_{xx}$ are estimated by least squares fits (4.5) using the region where the tracer plume is well contained within the surfzone ($\mathcal{R} < 0.55$, regions below the dashed gray lines in Figure 4.7). The modeled $\kappa^{({\rm A,B,C})}_{xx}$ and observed $\kappa^{({\rm obs})}_{\rm xx}$ (except for R1) are calculated between $t_{\rm p} = 0$ and the largest $t_{\rm p}$ where $\mathcal{R} < 0.55$. The R1 $\kappa^{({\rm obs})}_{\rm xx}$ is estimated from the first downstream transect (surfzone contained by inspection) and the assumed initial condition $\sigma^2(t_{\rm p} = 0) = 0$. Linear fits to $\sigma^{2\,({\rm A,B,C})}_{\rm surf}$ versus $t_{\rm p}$ have high r^2 values, with a mean $r^2 = 0.87$. Individual modeled $\kappa^{({\rm A,B,C})}_{xx}$ have relatively small errors (from the fit slope error), but

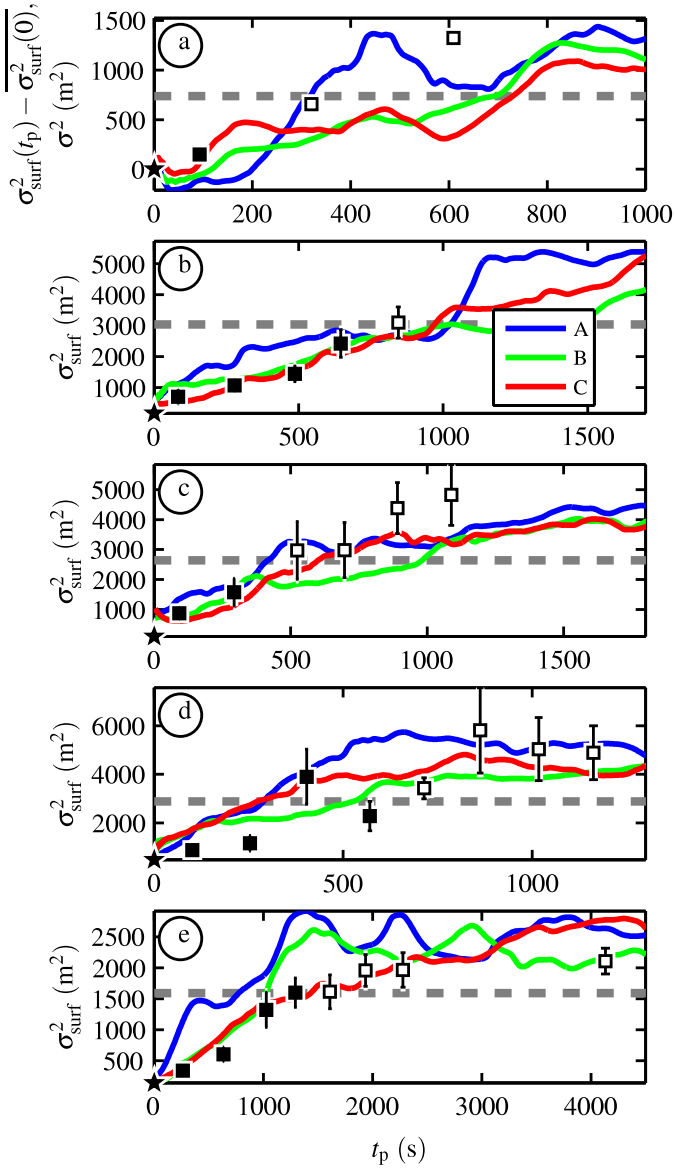

Figure 4.7: Modeled (color curves) and observed (black or white squares with error bars) squared cross-shore length scale $\sigma^2_{\rm surf}$ vs $t_{\rm p}$ for releases (b) R2, (c) R3, (d) R4, and (e)R6, and (a) $\sigma^{2\,({\rm A,B,C})}_{\rm surf}(t_{\rm p}) - \overline{\sigma^{2\,({\rm A,B,C})}_{\rm surf}}(t_{\rm p}=0)$ (modeled) and σ^2 (observed) for release R1. The $\overline{D}$ profiles that are well contained in the surfzone are used for κ_{xx} fits, and indicated by black squares (observed) or the region below the dashed gray line with $\mathcal{R} < 0.55$. The $\sigma^{2\,({\rm obs})}_{\rm surf}$ initial conditions (assuming a δ-function at $t_{\rm p}=0$) are indicated by the black stars. The mean $\sigma^2_{\rm surf}(t_{\rm p})$ skill over releases R2, R3, R4 and R6 is 0.92.

Table 4.3: Model $\kappa_{xx}^{(\mathrm{A,B,C})}$ derived from σ^2_{surf} versus t_{p} (Figure 4.8) fits and the mean $\langle\kappa_{xx}\rangle_{\mathrm{A,B,C}}$ over tracers A, B, and C.

	$\kappa_{xx}^{(\mathrm{A})}$	$\kappa_{xx}^{(\mathrm{B})}$	$\kappa_{xx}^{(\mathrm{C})}$	$\langle\kappa_{xx}\rangle_{\mathrm{A,B,C}}$
R1	1.28 ± 0.15	0.61 ± 0.07	0.30 ± 0.04	0.73 ± 0.29
R2	0.89 ± 0.04	0.81 ± 0.02	1.38 ± 0.04	1.02 ± 0.17
R3	1.71 ± 0.10	0.89 ± 0.05	1.86 ± 0.70	1.49 ± 0.30
R4	3.83 ± 0.18	1.34 ± 0.11	3.33 ± 0.24	2.83 ± 0.76
R6	0.81 ± 0.02	0.64 ± 0.01	0.56 ± 0.01	0.67 ± 0.07

relatively large variation between $\kappa_{xx}^{(\mathrm{A,B,C})}$ values for each tracer in a given release (Table 4.3). The mean model $\langle\kappa_{xx}\rangle_{\mathrm{A,B,C}}$ (averaged over tracers A, B, and C) range from 0.67–2.83 $\mathrm{m^2\,s^{-1}}$(Table 4.3) where errors include both the fit slope error and the variation between individual tracer $\kappa_{xx}^{(\mathrm{A,B,C})}$.

Mean model $\langle\kappa_{xx}\rangle_{\mathrm{A,B,C}}$ are similar to observed $\kappa_{\mathrm{xx}}^{(\mathrm{obs})}$ (Figure 4.8), with correlation $r^2 = 0.72$. The skill, $1 - \langle(\kappa_{\mathrm{xx}}^{(\mathrm{obs})} - \langle\kappa_{xx}\rangle_{\mathrm{A,B,C}})^2\rangle / \langle(\kappa_{\mathrm{xx}}^{(\mathrm{obs})})^2\rangle$, is 0.40. Model and observed cross-shore dispersion κ_{xx} are qualitatively similar for a given bathymetry and incident wave field, but the uncertainty in both are high (error bars Figure 4.8).

4.6 Discussion

4.6.1 Model-data Comparison

Tracer concentration $\overline{D}^{(\mathrm{A,B,C})}$ model data agreement is the most difficult to achieve (compared to cross-shore integrated moments), because $\overline{D}^{(\mathrm{A,B,C})}$ structure and magnitude depend on the cross-shore structure of $\overline{V}(x)$, eddy mixing intensity and structure, and the input tracer flux. Model and observed $\overline{D}^{(\mathrm{A})}$ and $\overline{D}^{(\mathrm{obs})}$ are similar with reasonable skill for releases R3, R4, R6 (Figure 4.4c,d,e), but other releases have significant deviations in plume location (R1, Figure 4.4a) or $\overline{D}^{(\mathrm{A})}$ magnitude (R2, Figure 4.4b) leading to low (negative) skill. The difference in R1 cross-shore plume location is likely by cross-shore advection of the mean $\overline{D}^{(\mathrm{obs})}$ plume (along-plume axis is not parallel to shore) by local bathymetric variation, however poor model dynamics cannot be ruled

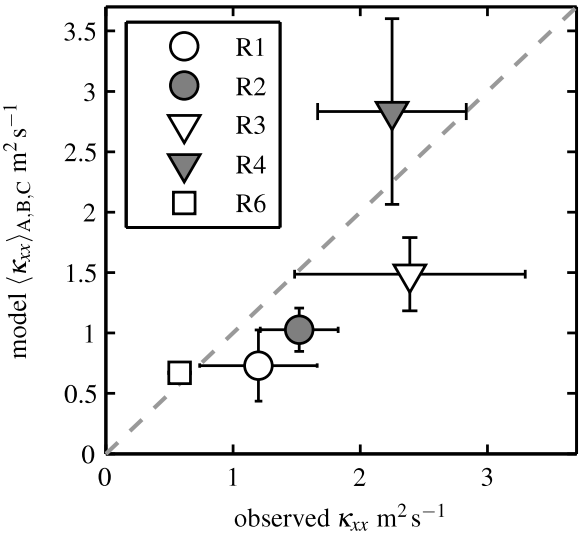

Figure 4.8: Mean modeled $\langle \kappa_{xx} \rangle_{\mathrm{A,B,C}}$ vs observed $\kappa_{\mathrm{xx}}^{(\mathrm{obs})}$, with a dashed line indicating perfect agreement. The $\kappa_{\mathrm{xx}}^{(\mathrm{obs})}$ error bars are estimated from the $\sigma_{\mathrm{surf}}^{2\,(\mathrm{obs})}$ versus t_{p} fit slope error [*Clark et al.*, 2010], and model $\langle \kappa_{xx} \rangle_{\mathrm{A,B,C}}$ error bars are the combination of fit slope errors and the variation in $\kappa_{xx}^{(\mathrm{A,B,C})}$ magnitudes. The skill (relative to perfect agreement) is 0.40.

out in causing the negative R1 $\overline{D}^{(\mathrm{A,B,C})}$ skill (Table 4.2). The R2 $\overline{D}^{(\mathrm{A})}$ are reasonably matched in the outer surfzone ($x < -60$, Figure 4.4b), but $\overline{D}^{(\mathrm{A})}$ magnitudes are often 2-5 times greater than $\overline{D}^{(\mathrm{obs})}$ near the shoreline, resulting in negative skill. This contrasts with the good agreement between R2 $M^{(\mathrm{A,B,C})}$ and $M^{(\mathrm{obs})}$ fluxes (Figure 4.5b). R2 model and observed $V(x)$ are well matched for $x < -50$ m, but model $V(x)$ is 0.25 $\mathrm{m\,s^{-1}}$less than observed near the shoreline ($x = -18$ m, Chapter 3, Figure 3.6). The under-predicted near-shoreline velocity coincides with over-predicted $\overline{D}^{(\mathrm{A})}$ (Figure 4.4b) resulting in matched $M^{(\mathrm{A,B,C})}$ (Figure 4.5b), but producing low model data agreement for $\overline{D}^{(\mathrm{A,B,C})}$ (Table 4.2). Despite low $\overline{D}^{(\mathrm{A,B,C})}$ skill, the R2 cross-shore dispersion (Figure 4.7b) has the best agreement (highest $\sigma^{2\,(\mathrm{A,B,C})}_{\mathrm{surf}}$ skill) of all the releases. Model $\overline{D}^{(\mathrm{A,B,C})}$ skill requires well matched Eulerian wave and current agreement, and absolute concentrations may be difficult to model even if the cross-shore mixing is well represented.

While $\overline{D}^{(\mathrm{A,B,C})}$ skill is variable and sometime negative, the cross-shore integrated moments $\mu^{(\mathrm{A,B,C})}$ (4.3) and $\sigma^{2\,(\mathrm{A,B,C})}_{\mathrm{surf}}$ (4.4) have high mean skill (0.88 and 0.92, repectively). The moments represent cross-shore plume structure by removing the dependence on absolute concentration. For example, $\mu^{(\mathrm{A,B,C})}$ are well matched, with high skill, for releases R1 and R2 (despite negative $\overline{D}^{(\mathrm{A,B,C})}$ skill), as well as R3 and R4 (Figure 4.6a,b,c,d).

The R6 $\mu^{(\mathrm{C})}$ closely matches $\mu^{(\mathrm{obs})}$, but $\mu^{(\mathrm{A})}$ and $\mu^{(\mathrm{B})}$ are much farther seaward resulting in a $\mu^{(\mathrm{A,B,C})}$ mean skill of 0.68, the lowest of all releases. Despite the highest $\overline{D}^{(\mathrm{A,B,C})}$ skill (Table 4.2), low $\overline{D}^{(\mathrm{A})}$ and $\overline{D}^{(\mathrm{B})}$ concentrations extend much farther seaward than the $\overline{D}^{(\mathrm{obs})}$ (see Figure 4.4e for $\overline{D}^{(\mathrm{A})}$), thus increasing $\mu^{(\mathrm{A})}$ and $\mu^{(\mathrm{B})}$ magnitudes. This may indicate mixing rates seaward of the surfzone are larger, or have different structure, than the R6 observations, transporting low $\overline{D}^{(\mathrm{A})}$ and $\overline{D}^{(\mathrm{B})}$ concentrations farther seaward. The model generally has greater low frequency ($f < 0.03$) rotational velocities seaward of the surfzone (Chapter 3), and increased seaward tracer dispersion could result from overly energetic model eddies not present in the observations.

The model $\sigma^{2\,(\mathrm{A,B,C})}_{\mathrm{surf}}$ skills are also high (0.92 over R2, R3, R4, and R6), and indicate the plume squared cross-shore length scales are generally well modeled. The variation between $\sigma^{2\,(\mathrm{A})}_{\mathrm{surf}}$, $\sigma^{2\,(\mathrm{B})}_{\mathrm{surf}}$, and $\sigma^{2\,(\mathrm{C})}_{\mathrm{surf}}$ (Figure 4.7) indicates there may be long timescale

variations (Chapter 3) in currents and eddies that have not been removed, even with 8000 s of averaging. In addition, there is alongshore variation in time-averaged $V(x,y)$ (see figures in Chapter 3) that effect $t_{\rm p}$ and resulting $\kappa_{xx}^{\rm (A,B,C)}$ estimates at different alongshore release locations. Such variation may occur naturally or be an artifact of the model wavemaker [*Johnson and Pattiaratchi*, 2006].

The observed $\kappa_{\rm xx}^{\rm (obs)}$ are estimates assuming the $\sigma_{\rm surf}^{2\,\rm (obs)}(t_{\rm p}=0)=x_0^2$ (tracer δ-function at the release location). For R6 the $\sigma_{\rm surf}^{2\,\rm (A,B,C)}(t_{\rm p}=0)$ are close to the assumed $\sigma_{\rm surf}^{2\,\rm (obs)}(t_{\rm p}=0)$, but the R2, R3, and R4 $\sigma_{\rm surf}^{2\,\rm (A,B,C)}(t_{\rm p}=0)$ are larger (by 153–724 $\rm m^2$) than the assumed value. There are no tracer measurements at the observed source, but tracer is sometimes visually observed to recirculate and spread around the source, and the model suggests the assumed $\sigma_{\rm surf}^{2\,\rm (obs)}(t_{\rm p}=0)=x_0^2$ underestimates the actual value. For example, the possible underestimation of R3 $\sigma_{\rm surf}^{2\,\rm (obs)}(t_{\rm p}=0)$ (Figure 4.7c) may have lead to increased R3 $\kappa_{\rm xx}^{\rm (obs)}$.

The $\kappa_{xx}^{\rm (A,B,C)}$ estimates have moderate skill (0.40) and higher correlation ($r^2=0.72$) indicating the surfzone cross-shore mixing in the model is similar to the observations. The initial increase in both model and observed $\sigma_{\rm surf}^2$ is roughly linear with $t_{\rm p}$ (Figure 4.7) indicating Brownian diffusion regimes. Individual $\kappa_{xx}^{\rm (A,B,C)}$ errors are small, roughly 5% of $\kappa_{xx}^{\rm (A,B,C)}$ magnitudes, but there are significant variations in $\kappa_{xx}^{\rm (A,B,C)}$ estimates for a given release. These differences may result from artifacts of the κ_{xx} estimation method, or long timescale variations. The range of $\sigma_{\rm surf}^{2\,\rm (A,B,C)}$ used for estimating κ_{xx} are cutoff at the $\mathcal{R}<0.55$ threshold (dashed gray lines in Figure 4.7) so that $\sigma_{\rm surf}^{2\,\rm (A,B,C)}$ variability (i.e., wiggles in the $\sigma_{\rm surf}^{2\,\rm (A,B,C)}$ lines in Figure 4.7) effects the range of $t_{\rm p}$ used. Thus, variation in $\sigma_{\rm surf}^{2\,\rm (A,B,C)}$ is passed through to the $\kappa_{xx}^{\rm (A,B,C)}$ estimate.

4.6.2 Time dependent alongshore fluxes and the cross-shore flux integral

The model tracer input flux is equal to the observed pump estimated input flux, however modeled alongshore tracer fluxes $M^{\rm (A,B,C)}(y)$ do not necessarily match the pump observations $M^{\rm (obs)}(y=0)$ (Figure 4.5). The $M^{\rm (obs)}$ are calculated from the mean $\overline{D}^{\rm (obs)}(x,y)$ and $\overline{V}(x)$ and do not include alongshore eddy fluxes. While time dependent alongshore fluxes are not available from the field data, they are calculated

from model output with the form

$$\mathcal{M}(y) = \int_{x_{\mathrm{F7}}}^{x_{\mathrm{in}}} h(x)\,\langle V(x,y,t)\,\overline{D}(x,y,t)\rangle\,dx, \tag{4.8}$$

where $\langle\rangle$ indicates a time average. The R4 model time dependent $\mathcal{M}^{(\mathrm{A})}$, roughly representative of $\mathcal{M}$ for all model releases and tracers, matches the observed pump flux at $y = 0$ and has less alongshore variation than $M^{(\mathrm{A})}$ (Figure 4.9). The comparison of $M^{(\mathrm{A})}$ and $\mathcal{M}^{(\mathrm{A})}$ indicates that alongshore eddy fluxes are non-zero, and likely present in the observations as well. The simple Fickian solution used to derive (4.5) assumes small $\mathcal{M}$, in agreement with the small 10% mean percent difference between R4 modeled $\mathcal{M}^{(\mathrm{A})}$ and $M^{(\mathrm{A})}$ for $0 < y < 500$ m (Figure 4.9). The M are generally smaller than $\mathcal{M}$ for $y < 200$ m indicating eddies are moving tracer downstream. Thus the age of the plume, t_{p}, may be overestimated by using $\overline{V}$, and κ_{xx} estimates may be biased slightly low.

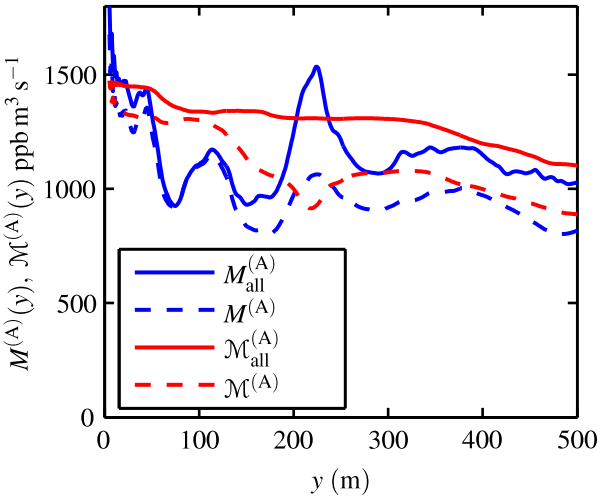

Figure 4.9: Mean (dashed blue curve) $M^{(\mathrm{A})}$ and mean time dependent (dashed red curve) $\mathcal{M}^{(\mathrm{A})}$ versus y for R4. The (solid blue curve) $M^{(\mathrm{A})}_{\mathrm{all}}$ and (solid red curve) $\mathcal{M}^{(\mathrm{A})}_{\mathrm{all}}$ are similar to $M^{(\mathrm{A})}$ (4.2) and $\mathcal{M}^{(\mathrm{A})}$ (4.8), but integrated over the entire cross-shore tracer domain.

The field observed $M^{(\mathrm{obs})}$ are integrated over the region where $\overline{V}$ and $\overline{D}^{(\mathrm{obs})}$ are known (i.e., x_{F7} to x_{in}), and excludes tracer outside this region. The model $M^{(\mathrm{A})}_{\mathrm{all}}$ and $\mathcal{M}^{(\mathrm{A})}_{\mathrm{all}}$ (Figure 4.9) are equivalent to (4.2) and (4.8), respectively, but they are integrated

over the entire cross-shore tracer domain. The $\mathcal{M}^{(\mathrm{A})}$ are smaller than the $\mathcal{M}^{(\mathrm{A})}_{\mathrm{all}}$ (and similarly for $M^{(\mathrm{A})}_{\mathrm{all}}$ and $M^{(\mathrm{A})}$), and the difference is primarily from tracer shoreward of x_{in}. The exclusion of tracer shoreward of x_{in} and alongshore eddy fluxes near the source account for the majority of the difference between observed dye pump and transect based $M^{(\mathrm{obs})}$ estimates.

4.6.3 Breaking κ_{br}

The model tracer diffusivity is a combination of a background diffusivity κ_0 (0.01 $\mathrm{m^2\,s^{-1}}$everywhere in the tracer domain) plus a breaking wave diffusivity κ_{br} set equal to the local breaking eddy viscosity ν_{br}. The application of κ_{br} simulates the spreading of tracer by breaking waves [*Feddersen*, 2007]. Although the κ_{br} does not include bore entrainment, significant cross-shore dispersion by bore entrainment is not visually observed [*Clark et al.*, 2010]. The application of ν_{br} to κ_{br} also assumes that mixing is the same for momentum and tracers. Previous work by *Henderson* [2007] suggests that the mean (time-averaged) breaking diffusivity $\overline{\kappa_{\mathrm{br}}}$ at a given location in the surfzone is the appropriate quantity when applied to bulk (or mean) cross-shore diffusion (Figure 4.10).

The $\overline{\kappa_{\mathrm{br}}}$ vary between releases, and are largest for R4. The R4 $\overline{\kappa_{\mathrm{br}}}(x)$ (Figure 4.10) increases from zero far seaward of the surfzone, to a maxima near the outer-surfzone (~ -100 m), and finally decrease towards the shoreline. Although R4 has the largest breaking diffusivities out of all the releases, the maximum $\overline{\kappa_{\mathrm{br}}} = 0.06\ \mathrm{m^2\,s^{-1}}$ is much smaller than the $O(1)$ estimates for $\langle \kappa_{xx} \rangle_{\mathrm{A,B,C}}$ (Table 4.3). The weak effect of breaking wave induced κ_{br} on cross-shore absolute dispersion is demonstrated by an R4 simulation with two tracers released at the same location, one with breaking and background diffusivities $\kappa_{\mathrm{br}} + \kappa_0$ applied to the tracer field and the other with background κ_0 only (Figure 4.11). The model σ^2_{surf} with and without κ_{br} are almost indentical (Figure 4.11).

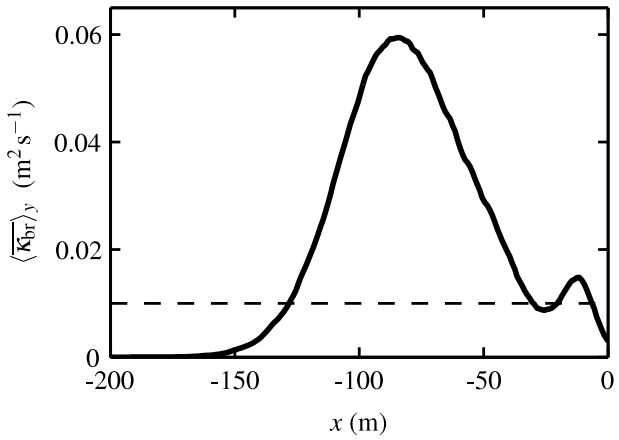

Figure 4.10: (solid curve) $\overline{\kappa_{\rm br}}$ and (dashed line) κ_0 vs x for R4, which has the largest $\overline{\kappa_{\rm br}}$ values of all the releases.

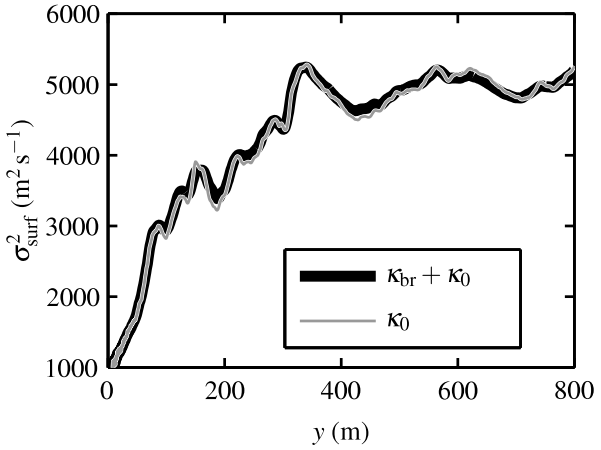

Figure 4.11: Model $\sigma^2_{\rm surf}$ vs y for R4 tracer with (black curve) full breaking-induced diffusivity $\kappa_{\rm br}+\kappa_0$ and (gray curve) background diffusivity κ_0 only. Both tracers are released at the same location in the model.

4.6.4 Model κ_{xx} Scalings

Scalings for κ_{xx} parameterize cross-shore mixing in terms of simple wave and current quantities. It is unlikely that any one mechanism is solely responsible for cross-shore mixing. A scaling that is highly correlated with κ_{xx} suggests it is a dominant dispersion mechanism.

The observed $\kappa_{\mathrm{xx}}^{(\mathrm{obs})}$ had the best agreement with a mixing-length scaling, i.e.,$\kappa_{xx} \sim \overline{\mathcal{V}}_{\mathrm{rot}} L_x$ that is the product of the surfzone width L_x and a surfzone-averaged low-frequency horizontal rotational velocity scale $\overline{\mathcal{V}}_{\mathrm{rot}}$. At a particular cross-shore location $\mathcal{V}_{\mathrm{rot}}(x)$ is defined (following *Lippmann et al.* [1999])

$$\mathcal{V}_{\mathrm{rot}}(x) = \sqrt{\int_{\mathrm{IG}} (S_{uu} + S_{vv} - \frac{g}{h} S_{\eta\eta}) df}, \tag{4.9}$$

where the S_{uu} (cross-shore velocity), S_{vv} (alongshore velocity), and $S_{\eta\eta}$ (pressure) spectra are integrated over infragravity frequencies ($0.004 < f < 0.03$ Hz). The model generally reproduces the magnitude and cross-shore structure of the observed $\mathcal{V}_{\mathrm{rot}}(x)$ over all releases (see Figure 3.10 in Chapter 3). The same $\overline{\mathcal{V}}_{\mathrm{rot}} L_x$ scaling is applied to model diffusivities (Figure 4.12a), where L_x is taken from the cross-shore maxima in model H_{s}, and $\overline{\mathcal{V}}_{\mathrm{rot}}$ is the surfzone averaged ($-L_x < x < 0$) $\mathcal{V}_{\mathrm{rot}}(x)$. The correlation ($r^2 = 0.59$) of the observed mixing-length scaling $\kappa_{xx} \sim \overline{\mathcal{V}}_{\mathrm{rot}} L_x$ suggested that that low-frequency eddies (vortical motions) were a dominant mechanism of cross-shore tracer dispersion. Here the same mixing-length scaling is applied to the model. In contrast, the model $\overline{\mathcal{V}}_{\mathrm{rot}} L_x$ scaling has a lower $r^2 = 0.29$ correlation.

The *Lippmann et al.* [1999] method for estimating rotational velocities is indirect and subject to assumptions about the infragravity wave field. The instantaneous model velocity field can also be decomposed into irrotational $\boldsymbol{u}_\phi$ and rotational $\boldsymbol{u}_\psi$ velocity components. Following *Spydell and Feddersen* [2009], the 2-D model velocity field $\boldsymbol{u}$ is decomposed into $\boldsymbol{u}_\phi = \boldsymbol{\nabla}\phi$ and $\boldsymbol{u}_\psi = \boldsymbol{\nabla} \times \psi$, where ϕ is the velocity potential, and ψ is the streamfunction. By definition, $\boldsymbol{\nabla} \times \boldsymbol{u}_\phi = 0$ and thus vorticity comes entirely from $\boldsymbol{u}_\psi$. Over the surfzone region, the rms (time- and spatial averaged) error of the velocity decomposition is small (i.e., rms $\boldsymbol{u} - (\boldsymbol{u}_\phi + \boldsymbol{u}_\psi)$ is $< 0.01\ \mathrm{m\,s^{-1}}$and maximum fractional error is $< 1\%$).

From the model rotational velocities, a cross-shore rotational velocity $U_\psi^{(\mathrm{rms})}$ is

estimated from the surfzone averaged rms cross-shore component of $\boldsymbol{u}_\psi$. The rotational velocity mixing-length scaling $\kappa_{xx} \sim U_\psi^{(\mathrm{rms})} L_x$ has a higher $r^2 = 0.63$ with κ_{xx} (Fig. 4.12b). The velocity spectrum is red and $U_\psi^{(\mathrm{rms})}$ has contributions from frequencies below $f = 0.004$ Hz (the limit of $\overline{\mathcal{V}}_{\mathrm{rot}}$ contributions), this indicating that model eddy energy with frequencies $f < 0.004$ Hz may be important to the model cross-shore dispersion.

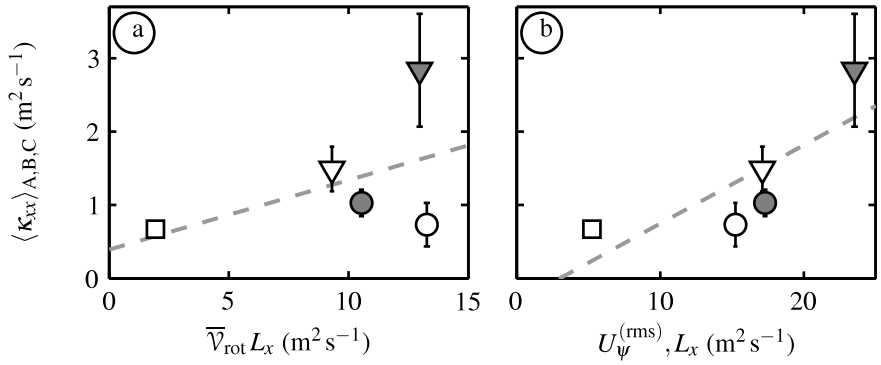

Figure 4.12: Model $\langle \kappa_{xx} \rangle_{\mathrm{A,B,C}}$ vs (a) $\overline{\mathcal{V}}_{\mathrm{rot}} L_x$, and (b) $U_\psi^{(\mathrm{rms})} L_x$ scalings. The dashed gray line indicates linear fits to each scaling, and r^2 correlations are (a) 0.29, (b) 0.63.

4.7 Summary

Time-dependent wave-resolving Boussineq surfzone models could provide insight into surfzone tracer dispersion, but no previous model validation for surfzone tracers has been conducted. Here, 5 observed tracer releases from the HB06 experiment are simulated with an advection diffusion model coupled to the Boussinesq surfzone model `funwaveC` , initialized with observed bathymetry and incident wave spectra. Model tracer is spread by currents, eddies, a breaking wave eddy diffusivity κ_{br} set equal to the breaking wave eddy viscosity, and a small (0.01 $\mathrm{m}^2\,\mathrm{s}^{-1}$) background diffusivity. Three non-interacting model tracers were released 250 m apart in the alongshore, using the observed cross-shore release locations and pumped dye release rates.

The continuously released model tracers form alongshore parallel plumes in the wave driven alongshore current, qualitatively similar to the observations, with decreas-

ing peak concentrations and increasing cross-shore widths with downstream distance from the source. Modeled $\overline{D}^{(\mathrm{A,B,C})}$ and observed $\overline{D}^{(\mathrm{obs})}$ often have shoreline attached profiles (near-shoreline maxima) roughly resembling a half-Gaussian. The $\overline{D}$ model-data agreement depends on plume shape, cross-shore location, and absolute concentration, and yields highly variable skill (from negative to 0.73).

Cross-shore integrated moments remove the dependence on absolute concentration, and compare generalized cross-shore plume structure. The model $\overline{D}^{(\mathrm{A,B,C})}$ cross-shore surface-centers of mass $\mu^{(\mathrm{A,B,C})}$ move away from the shoreline with downstream distance, and agree well with observations (0.88 skill over all releases). The release R6 is an exception, where patches of low $\overline{D}^{(\mathrm{A})}$ and $\overline{D}^{(\mathrm{B})}$ seaward of the surfzone over predict $\mu^{(\mathrm{A})}$ and $\mu^{(\mathrm{B})}$ magnitudes. The plume squared cross-shore length scale σ^2_{surf} (second moment) is used to estimate bulk cross-shore diffusivity κ_{xx}. The downstream evolution of model and observed σ^2_{surf} is similar, with high skill (0.92).

Model $\kappa_{xx}^{(\mathrm{A,B,C})}$ are variable between model tracers (A,B,C), where variation may be caused by long timescale variation or artifacts of the κ_{xx} estimation method. Mean model $\langle\kappa_{xx}\rangle_{\mathrm{A,B,C}}$ are similar to observed $\kappa_{\mathrm{xx}}^{(\mathrm{obs})}$, with good correlation ($r^2 = 0.72$) but only moderate skill (0.40). Observed $\kappa_{\mathrm{xx}}^{(\mathrm{obs})}$ were correlated with a mixing length scaling based on bulk infragravity cross-shore rotational velocities $\mathcal{V}_{\mathrm{rot}}(x)$, however modeled $\langle\kappa_{xx}\rangle_{\mathrm{A,B,C}}$ have a much lower $r^2 = 0.29$ correlation with this scaling. An alternative mixing length scaling using the model rms cross-shore component of a rotational velocity decomposition has a higher $r^2 = 0.63$ correlation with $\langle\kappa_{xx}\rangle_{\mathrm{A,B,C}}$.

Mean breaking eddy diffusivities are small, $\kappa_{\mathrm{br}} < 0.06\ \mathrm{m^2\,s^{-1}}$. Model σ^2_{surf} are examined with and without κ_{br} for two non-interacting tracers released at the same location. The downstream evolutions of the two tracers are nearly identical, indicating the breaking eddy diffusivity does not effect dispersion significantly.

Chapter 4, in part is currently being prepared for submission for publication of the material. Clark, David B.; Feddersen, Falk; Guza, R.T. The dissertation author was the primary investigator and author of this material.

Bibliography

Batchelor, G. K., Diffusion in a field of homogeneous turbulence. I. Eulerian analysis, *Austral. J. Sci. Res.*, *2*, 437–450, 1949.

Batchelor, G. K., Diffusion in a field of homogeneous turbulence. II. The relative motion of particles, *Proc. Cam. Phil. Soc.*, *48*, 345–363, 1952.

Beach, R. A., and R. W. Sternberg, Suspended sediment transport in the surf zone: Response to incident wave and longshore current interaction, *Marine Geology*, *108*, 275–294, 1992.

Beach, R. A., and R. W. Sternberg, Suspended-sediment transport in the surf zone: Response to breaking waves, *Cont. Shelf Res.*, *16*(15), 1989–2003, 1996.

Boehm, A. B., Model of microbial transport and inactivation in the surf zone and application to field measurements of total coliform in Northern Orange County, California, *Environ. Sci. Technol.*, *37*(24), 5511–5517, 2003.

Boehm, A. B., S. B. Grant, J. H. Kim, C. D. McGee, S. Mowbray, C. Clark, D. Foley, and D. Wellmann, Decadal and shorter period variability of surfzone water quality at Huntington Beach, California, *Environ. Sci. Technol.*, *36*, 3885–3892, 2002.

Bowen, A. J., and D. L. Inman, Nearshore mixing due to waves and wave-induced currents, *Rapp. P.-v Reun. Cons. Int. Explor. Mer*, *167*, 6–12, 1974.

Brenninkmeyer, S. J. B., In situ measurements of rapidly fluctuating, high sediment concentrations, *Mar. Geol.*, *20*(2), 117–128, 1976.

Brown, J., J. MacMahan, A. Reneirs, and E. B. Thornton, Surfzone diffusivity on a rip channeled beach, *J. Geophys. Res.*, *114*(C11015), doi:10.1029/2008JC005158, 2009.

Campbell, E. E., and G. C. Bate, The influence of current direction on longshore distribution of surf phytoplankton, *Botanica Marina*, *31*, 257–262, 1988.

Chen, Q., J. T. Kirby, R. A. Dalrymple, S. Fengyan, and E. B. Thornton, Boussinesq modeling of longshore currents, *J. Geophys. Res., Oceans*, *108*, doi: 10.1029/2002JC001,308, 2003.

Clark, D. B., F. Feddersen, M. M. Omand, and R. T. Guza, Measuring fluorescent dye in the bubbly and sediment laden surfzone, *Water Air Soil Poll.*, *204*(1-4), 103–115, doi:10.1007/s11270-009-0030-z, 2009.

Clark, D. B., F. Feddersen, and R. T. Guza, Cross-shore surfzone tracer dispersion in an alongshore current, *J. Geophys. Res., Oceans*, *115*(C10035), doi: 10.1029/2009JC005683, 2010.

Clarke, L. B., D. Ackerman, and J. Largier, Dye dispersion in the surfzone: Measurements and simple models, *Cont. Shelf Res.*, *27*, 650–669, 2007.

Csanady, G. T., Turbulent diffusion in Lake Huron, *J. Fluid Mech.*, *17*(3), 360–384, 1963.

Csanady, G. T., *Turbulent Diffusion in the Environment*, D. Reidel, New York, 1973.

Deane, G. B., Sound generation and air entrainment by breaking waves in the surf zone, *J. Acoust. Soc. Amer.*, *102*(5), 2671–2689, 1997.

Deane, G. B., and M. D. Stokes, Air entrainment processes and bubble size distributions in the surf zone, *J. Phys. Ocean.*, *29*, 1393–1403, 1999.

Denny, M. W., and M. F. Shibata, Consequences of surf-zone turbulence for settlement and external fertilization, *Am. Nat.*, *134*, 859–889, 1989.

Durran, D. R., The 3rd-order adams-bashforth method - an attractive alternative to leapfrog time differencing, *Mon. Wea. Rev.*, *119*, 702–720, 1991.

Emery, W. J., and R. E. Thomson, *Data analysis methods in physical oceanography*, Elsevier, New York, 2001.

Feddersen, F., Breaking wave induced cross-shore tracer dispersion in the surfzone: Model results and scalings, *J. Geophys. Res.*, *112*(C09012), doi: 10.1029/2006JC004006, 2007.

Feddersen, F., Quality controlling surfzone acoustic doppler velocimeter observations to estimate the turbulent dissipation rate, *J. Atmos. and Ocean. Tech.*, submitted, 2010a.

Feddersen, F., Observations of the surfzone dissipation rate, *J. Phys. Ocean.*, in preparation for, 2010b.

Feddersen, F., and J. H. Trowbridge, The effect of wave breaking on surf-zone turbulence and alongshore currents: a modelling study, *J. Phys. Ocean.*, *35*, 2187–2204, 2005.

Feuerstein, D. W., and R. Selleck, Fluorescent tracers for dispersion measurements, *J. Sanit. Eng. Div., Am. Soc., Civ. Eng.*, *89(SA4)*, 1–21, 1963.

Fischer, H. B., Tensor form of bulk dispersion coefficient in a bounded skewed shear-flow, *J. Geophys. Res.*, *83*(NC5), 2373–2375, 1978.

Fong, D. A., and M. T. Stacey, Horizontal dispersion of a near-bed coastal plume, *J. Fluid Mech.*, *489*, 239–267, 2003.

Grant, S. B., J. H. Kim, B. H. Jones, S. A. Jenkins, J. Wasyl, and C. Cudaback, Surf zone entrainment, along-shore transport, and human health implications of pollution from tidal outlets, *J. Geophys. Res.*, *110*(C10025), doi:10.1029/2004JC002,401, 2005.

Guibault, G. (Ed.), *Practical Fluorescence*, 2nd ed., Marcel Dekker, New York, 1990.

Haile, R. W., et al., The health effects of swimming in ocean water contaminated by storm drain runoff, *Epidemiology*, *10*, 355–363, 1999.

Hallermeier, R. J., Terminal settling velocity of commonly occurring sand grains, *Sedimentology*, *28*, 859–865, doi:10.1111/j.1365-3091.1981.tb01948.x, 1981.

Hanemann, M., L. Pendleton, and D. Layton, Southern California beach valuation project: Summary report on the expenditure module, *Tech. Rep. http://marineeconomics.noaa.gov/SCBeach/laobeach1.html*, National Oceanic and Atmospheric Administration, Silver Spring, MD, 2001.

Harlow, F., and J. Welch, Numerical calculation of time-dependent viscous incompressible flow of fluid with free surfaces, *Phys. Fluids*, *8*, 2181–2189, 1965.

Harris, T. F. W., J. M. Jordaan, W. R. McMurray, C. J. Verwey, and F. P. Anderson, Mixing in the surf zone, *Int. J. Air Wat. Polut.*, *7*, 649–667, 1963.

Henderson, S. M., Comment on 'Breaking wave induced cross-shore tracer dispersion in the surfzone: Model results and scalings', *J. Geophys. Res.*, *111*(C12007), doi: 10.1029/2006JC003539, 2007.

Houghton, R. W., Lagrangian flow at the foot of a shelfbreak front using a dye tracer injected into the bottom boundary layer, *Geophys. Res. Let.*, *24*(16), 2035–2038, 1997.

Inman, D. L., R. J. Tait, and C. E. Nordstrom, Mixing in the surfzone, *J. Geophys. Res.*, *26*, 3493–3514, 1971.

Issa, R., D. Rouge, M. Benoit, D. Violeau, and A. Joly, Modelling algae transport in coastal areas with a shallow water equation model including wave effects, *J. Hydroenviron. Res.*, *3*(4), 1570–6443, doi:10.1016/j.jher.2009.10.004, 2010.

Johnson, D., and C. Pattiaratchi, Transient rip currents and nearshore circulation on a swell-dominated beach, *J. Geophys. Res.*, *109*, doi:10.1029/2003JC001798, 2004.

Johnson, D., and C. Pattiaratchi, Boussinesq modelling of transient rip currents, *Coastal Eng.*, *53*(5), 419–439, 2006.

Jones, N. L., R. J. Lowe, G. Pawlak, D. A. Fong, and S. G. Monismith, Plume dispersion on a fringing coral reef system, *Limnol. Oceanogr.*, *53*(20), 2273–2286, 2008.

Kennedy, A. B., Q. H. Chen, J. T. Kirby, and R. A. Dalrymple, Boussinesq modeling of wave transformation, breaking and runup I: One dimension, *J. Waterway, Port, Coastal, and Ocean Eng.*, *126*, 39–47, 2000.

Kuik, A. J., G. P. V. Vledder, and L. H. Holthuijsen, A method for the routine analysis of pitch-and-roll buoy wave data, *J. Phys. Ocean.*, *18*, 1020–1034, 1988.

Ledwell, J. R., T. F. Duda, M. A. Sundermeyer, and H. E. Seim, Mixing in a coastal environment: 1. A view from dye dispersion, *J. Geophys. Res.*, *109*(C10013), doi:10.1029/2003JC002,194, 2004.

Lippmann, T. C., T. H. C. Herbers, and E. B. Thornton, Gravity and shear wave contributions to nearshore infragravity motions, *J. Phys. Ocean.*, *29*(2), 231–239, 1999.

Lynett, P., Nearshore modeling using high-order boussinesq equations, *J. Waterway, Port, Coastal, and Ocean Engineering*, *132*, 348–357, 2006.

Murthy, C. R., Horizontal diffusion charateristics in Lake Ontario, *J. Phys. Ocean.*, *6*, 76–84, 1976.

Noble, R. T., J. H. Dorsey, M. Leecaster, V. Orozco-Borbón, D. Reid, K. Schiff, and S. B. Weisberg, A regional survey of the microbiological water quality along the shoreline of the Southern California Bight, *Environ. Monit. Assess.*, *64*(1), 435–447, 2000.

Noyes, T., R. Guza, S. Elgar, and T. Herbers, Comparison of methods for estimating nearshore shear wave variance, *J. Atmos. and Ocean. Tech.*, *19*(1), 136–143, 2002.

Noyes, T., R. Guza, S. Elgar, and T. Herbers, Field observations of shear waves in the surf zone, *J. Geophys. Res.*, *109*(C1), doi:10.1029/2002JC001761, 2004.

Nwogu, O., Alternative form of boussinesq equations for nearshore wave propagation, *J. Wtrwy., Port, Coast., and Oc. Engrg.*, *119*, 618–638, 1993.

Ogston, A. S., and R. W. Sternberg, Effect of wave breaking on sediment eddy diffusivity, suspended-sediment and longshore sediment flux profiles in the surf zone, *Cont. Shelf Res.*, *22*, 633–655, 2002.

Okubo, A., Oceanic diffusion diagrams, *Deep-Sea Res.*, *18*, 789–802, 1971.

Oltman-Shay, J., P. A. Howd, and W. A. Birkemeier, Shear instabilities of the mean longshore current 2. Field observations, *J. Geophys. Res.*, *94*, 18,031–18,042, 1989.

Omand, M. M., F. Feddersen, D. B. Clark, P. J. S. Franks, J. J. Leichter, and R. T. Guza, The influence of bubbles and sand on chlorophyll fluorescence measurements in the surfzone, *Limnol. Oceanogr. Methods*, *7*, 354–362, 2009.

Pearson, J. M., I. Guymer, J. R. West, and L. E. Coates, Solute mixing in the surf zone, *J. Waterwy., Port, Coast., and Oc. Eng.*, *135*(4), 127–134, 2009.

Peregrine, D. H., Long waves on a beach, *J. Fluid Mech.*, *27*(04), 815–827, doi: 10.1017/S0022112067002605, 1967.

Peregrine, D. H., Surf zone currents, *Theor. Comput. Fluid Dyn.*, *10*, 295–309, 1998.

Pritchard, D. W., Background problems in fluorometric dye measurement in natural water, *Oceans*, *11*, 572–582, 1979.

Pritchard, D. W., and J. H. Carpenter, Measurements of turbulent diffusion in estuarine and inshore waters, *Bull. Int. Ass. Sci. Hydrol.*, *20*, 37–50, 1960.

Reniers, A., J. Roelvink, and E. Thornton, Morphodynamic modeling of an embayed beach under wave group forcing, *J. Geophys. Res.*, *109*(C1), doi: 10.1029/2002JC001586, 2004.

Rodi, W., Examples of calculation methods for flow and mixing in stratified fluids, *J. Geophys. Res.*, *92*(C5), 5305–5328, 1987.

Rodriguez, A., A. Sánchez-Arcilla, J. Redondo, E. Bahia, and J. Sierra, Pollutant dispersion in the nearshore region: modelling and measurements, *Wat. Sci. and Tech.*, *32*(9-10), 169–178, doi:doi:10.1016/0273-1223(96)00088-1, 1995.

Seymour, R., R. Guza, W. O'Reilly, and S. Elgar, Rapid erosion of a small Southern California beach fill, *Coastal Eng.*, *52*(2), 151–158, 2005.

Smart, P. L., and I. M. S. Laidlaw, An evaluation of some fluorescent dyes for water tracing, *Wat. Resour. Res.*, *13*(1), 15–33, 1977.

Spydell, M. S., and F. Feddersen, Lagrangian drifter dispersion in the surf zone: Directionally spread, normally incident waves, *J. Phys. Ocean.*, *39*, 809–830, 2009.

Spydell, M. S., F. Feddersen, R. T. Guza, and W. E. Schmidt, Observing surf-zone dispersion with drifters, *J. Phys. Ocean.*, *37*(12), 2007.

Spydell, M. S., F. Feddersen, and R. T. Guza, Observations of drifter dispersion in the surfzone: The effect of sheared alongshore currents, *J. Geophys. Res.*, *114*(C07028, doi:10.1029/2009JC005328), 2009.

Stanbro, W. D., and D. A. Pyrch, Stability of Rhodamine WT in saline waters, *Wat. Resour. Res.*, *15*(6), 1631–1632, 1979.

Suijlen, J. M., and J. J. Buyse, Potentials of photolytic Rhodamine WT as a large-scale water tracer assessed in a long-term experiment in the Loosdrecht Lakes, *Limnol. Oceanogr.*, *36*(6), 1411–1423, 1994.

Talbot, J. W., and M. J. Boon, The adsorption of rhodamine on to suspended sediments, *ICES J. Mar. Sci.*, *32*(2), 128–132, 1975.

Tao, S., and T. JianHua, Numerical simulation of pollutant transport acted by wave for a shallow water sea bay, *Int. J. Numer. Meth. Fluids*, *51*, 469–487, doi: 10.1002/fld.1116, 2006.

Taylor, G., The dispersion of matter in turbulent flow through a pipe, *Proc. Roy. Soc. Lond. A*, *223*(1155), 446–468, 1954.

Taylor, G. I., Diffusion by continuous movements, *Proc. London Math. Soc.*, *20*, 196–212, 1921.

Tennekes, H., and J. L. Lumley, *A First Course in Turbulence*, MIT Press, 1972.

Tilburg, C. E., R. W. Houghton, and R. W. Garvine, Mixing of a dye tracer in the Delaware plume: Comparison of observations and simulations, *J. Geophys. Res.*, *112*(C12004), doi:10.1029/2006JC003,928, 2007.

Wei, G., J. T. Kirby, S. T. Grilli, and R. Subramanya, A fully nonlinear Boussinesq model for surface waves. I. Highly nonlinear, unsteady waves., *J. Fluid Mech.*, *294*, 71–92, 1995.

Wei, G., J. T. Kirby, and A. Sinha, Generation of waves in Boussinesq models using a source function method, *Coastal Eng.*, *36*, 271–299, 1999.

Wunsch, C., *The Ocean Circulation Inverse Problem*, Cambridge University Press, 1996.

Yu, Y., R. W. Sternberg, and R. A. Beach, Kinematics of breaking waves and associated suspended sediment in the nearshore zone, *Cont. Shelf Res.*, *13*(11), 1219–1242, 1993.

Zege, E. P., I. L. Katsev, A. S. Prikhach, G. Gilbert, and N. Witherspoon, Simple model of the optical characteristics of bubbles and sediments in seawater of the surf zone, *Appl. Opt.*, *45*(25), 6577–6585, 2006.

Zelt, J. A., The run-up of nonbreaking and breaking solitary waves, *Coastal Eng.*, *15*, 205–246, 1991.